24/12/1989

DFUPG 25/89

*Revised in* 2/5/1990

# THE LARGE LIMITED STREAMER TUBES SYSTEM OF THE SLD EXPERIMENT*

Behcet Alpat

Dipartimento di Fisica and Sezione INFN di Perugia

06100 Perugia, ITALY

24 December 1989

* Doctoral Thesis

**Abstract**

The studies of the operating characteristics of the limited streamer tube system for a large hadron calorimeter and muon identifier built for the *SLD* detector at Stanford Linear Accelerator Center, are presented. A description is given of the *SLD* detector with emphasis on its physics goals. After an overview on the properties of gas detectors, the construction techniques and operational performance of the limited streamer tubes and chambers of the warm iron calorimeter are discussed in detail. The methods and results on reliability and longevity tests of limited streamer tubes are summarized together with the performance of a warm iron calorimeter prototype in a test beam.

## Table of Contents

# Chapter 1. Introduction

The limited streamer tubes (LSTs) are gaseous detectors widely used in high energy physics, both accelerator and underground experiments. The main reasons for the choice of these devices are their high efficiency, operating stability, large pulses allowing relatively simple readout electronics, possibility to use the external cathodes for multi dimensional readout, and low cost. About 80,000 of these detectors were used to construct large hadron calorimetry and tracking system of the Stanford Large Detector (*SLD*).

This wide utilization motivated a large R&D effort in many groups. In this thesis we present a summary of these works, in particular, referring to studies performed in *SLD* framework.

## 1.1 Outline of Thesis

The physics motivations and the main components of the *SLD* experiment are described in Chapter 2. The Stanford Linear Collider (*SLC*) machine and the *SLD* data acquisition system are also presented.

Chapter 3 discusses general properties of gas detectors including their various operational modes. The structure of the LSTs used in the *SLD* Warm Iron Calorimeter (WIC) chambers and some important parameters affecting their operational performances are also described.

In Chapter 4 the construction details of the WIC LSTs and chambers are given.

Chapter 5 considers the details of the limited streamer mechanism and of the operating characteristics of the LSTs. The characteristics of the digital and analog readout systems of the *SLD* WIC chambers are also discussed.

In Chapter 6 the long term test procedures performed with the WIC LSTs and their statistical results are summarized. The cosmic rays test of the WIC chambers are also discussed together with the performance and results of a WIC prototype in a test beam.

Appendix A discusses the studies performed with non–flammable $Ar+C_4H_{10}+CO_2$ based ternary mixtures as an alternative to the flammable "standard mixture".

Appendix B gives the results obtained from the studies performed with the non–flammable, $CF_4$ based fast gas mixtures.

Finally, Appendix C briefly describes the database system used for *SLD* WIC.

# Chapter 2. The *SLD* Experiment

## 2.1 Introduction

In this Chapter we will discuss first the physics topics which will be studied in the *SLD* experiment. We will then briefly present the main components of this experiment including the *SLD* data acquisition system.

## 2.2 Physics Motivation for the *SLD* at the *SLC*

The *SLD* experiment is being constructed at Stanford Linear Accelerator Center (SLAC) as second generation experiment for the *SLC* $Z^0$ factory which will extensively make use of the polarized electron beams. The *SLD* is designed to study the physics of $e^+e^-$ collisions at 100 GeV center–of–mass in a complementary way together with the LEP experiments at CERN.

The study of $e^+e^-$ collisions at 100 GeV center–of–mass with polarized beams will give the possibility to precisely test the Standard Model (SM) of the electroweak (EW) interactions and it will open up new horizons in the search of new and exotic physics. In the following, we list the main physics topics of *SLD* program at the *SLC* and the corresponding experimental requirements.

### *2.2.1 Precision Test of the SM, EW interactions and QCD*

The standard model of EW interactions is based on the gauge group SU(2) $\times$ U(1). As a result of this, the electromagnetic and weak interactions are unified in a gauge theory with three intermediate vector bosons, ($W^{\pm}$, $Z^0$), and the photon as gauge particles. The spontaneous breakdown of local gauge symmetry[1] (Higgs mechanism) allow for the generation of vector bosons and fermions masses. The masses of these gauge particles are given by the following expressions

$$M_w = \frac{1}{2} g\nu, \qquad M_Z = \frac{1}{2}\nu\sqrt{g^2 + {g'}^2} \tag{2.1}$$

$$M_\gamma = 0, \qquad M_{fermion} = \frac{h\nu}{\sqrt{2}} \tag{2.2}$$

where $g$ and $g'$ are the two gauge coupling constants and $\nu$ is the vacuum expectation value of the Higgs bosons.

The standard model is very sensitive to these parameters ($g$, $g'$ and $\nu$) and since they are not directly observable, it is convenient to replace them by parameters that are more closely related to experiments, namely $\alpha$, $G_F$, $M_Z$.

$\alpha = e^2/4\pi$ is given by the electron charge from Thomson scattering, the Fermi constant $G_F$ from the muon lifetime $\tau_\mu$, and both are known to extremely high precision, while mass of $Z^0$, $M_Z$, has been measured to 4 significant digits at the LEP/*SLC*. From above expressions Sirlin has introduced the following definition[2,3]

$$sin^2\Theta_w = 1 - \frac{{M_w}^2}{{M_Z}^2} \tag{2.3}$$

rewritten as

$$sin^2\Theta_w = \frac{\pi\alpha(m_e)}{\sqrt{2}G_F(m_\mu)} \cdot \frac{1}{m_w^2} \cdot \frac{1}{1-\Delta r}, (\Delta r = e, G_\mu, M_Z, m_t, m_H ...) \tag{2.4}$$

where $\Theta_w$ is the weak mixing or Weinberg angle and $\Delta r$ is the correction term which its exact value depends on the Higgs and top quark masses.

### *2.2.1.1 Measurement of the Mass and Width of the $Z^0$ Boson*

Since the precise measurements of $M_Z$ and $sin^2\Theta_W$ are very important high–precision test of the SM–EW theory, one important goal of *SLD* is to perform these measurements precisely, in particular, the mass and the width of the $Z^0$ resonance. A good way to measure $M_Z$ and $\Gamma_Z$ is, for instance, to look for the process $e^+e^- \rightarrow \mu^+\mu^-$ by scanning along the resonance. Aim[4] of *SLD* is an accuracy on $M_Z$ of about 30 MeV which would reduce the errors on $sin^2\Theta_w$ to

$\leq 0.0004$. The precision is affected by systematics due to the uncertainty on the knowledge of the machine energy and luminosity and on the detector acceptance (angular resolution, positioning accuracy etc.). Recent studies[5] have also shown that in *SLD* it will be possible a measurement of $\Gamma_Z$ by using large angle $e^+e^-$ events without making use of the luminosity measurements, reaching a precision of 2% of statistical error which is consistent with the typical systematic limit of the luminosity measurement techniques.

In *SLD* the mass and the width of $Z^0$ will be measured using almost all final states decaying into charged fermion pairs. The coupling ($C$) of any fermion state to the $Z^0$ can be written[6], in terms of the 3rd component of its weak isospin ($I_3$), its charge ($Q$), and $sin^2\Theta_w$;

$$C = \frac{-ie}{sin\Theta_w cos\Theta_w}[(I_{3l} - Qsin^2\Theta_w)\frac{(1-\gamma_5)}{2} + (I_{3r} - Qsin^2\Theta_w)\frac{(1-\gamma_5)}{2}] \tag{2.5}$$

where the first term in the brackets relates to the left–handed coupling, and the second to the right–handed coupling. Since $I_{3r}$ is zero for fermions, right–handed massless neutrinos should not be observed. It is convenient to define an axial vector ($a$) term which does not depend on $sin^2\Theta_w$ and couples via $\gamma_5$, and a vector ($v$) coupling which is sensitive to $sin^2\Theta_w$:

$$a = 2I_3 \tag{2.6}$$

$$v = 2(I_3 - 2Qsin^2\Theta_w) \tag{2.7}$$

so that the total width of the $Z^0$ can then be written,

$$\Gamma_{total} = \sum_i \beta_i N_i^c \frac{G_F M_Z^3}{24\pi\sqrt{2}}(v_i^2 + a_i^2)C_i^f \tag{2.8}$$

where the sum is over all pointlike fermions. The kinematic factor

$$\beta_i = \sqrt{\frac{1 - 4m_i^2}{s}}, \tag{2.9}$$

is close to one for all known fermions, $N_i^c$ is the number of colors being three for quarks and one for leptons. The final state correction ($C_f$) depends on the phase space enlargement due to final–state radiation[7],

$$C_f = \left(1 + \frac{3\alpha_{QED}}{4\pi}q^2 + O(\alpha_{QED}^2)\right)(1 + \frac{N_\nu - 1}{2})$$
$$\left(\frac{\alpha_s}{\pi} + (\frac{\alpha_s}{\pi})^2(1.98 - .115N_f) + O(\alpha_s^3)\right) \tag{2.10}$$

where $N_f$ is the number of light flavors, and $q_i$ is the electric charge of the fermion. The difference between the total and the partial width to charged leptons and hadrons is the partial width into neutral particles, ($\Gamma_{\nu\bar{\nu}} = \Gamma_{total} - \Gamma_{visible}$). It is also possible indirect measurements of $Z^0$ width by measuring the cross sections at the peak.
Recent results from L3 experiment[8] at LEP gives the following values; $M_Z$=91.16±0.024±0.030 GeV/c$^2$ $sin^2\Theta_w$=0.2306±0.0003 and $\Gamma_Z$=2.539±0.054 GeV/c$^2$, ($m_t$ and $m_H$ were assumed to be equal to 100 GeV/c$^2$).

#### *2.2.1.2 Polarization and Asymmetries*

Due to the present knowledge of weak interactions, left and right handed fermionic particles interact in a different way. In order to explore this difference there are two possibilities. The first one is to prepare the spin state of the incident particle (polarization), and second is to analyze the spin state of outgoing particle. Due to the difficulty of measuring the polarization in the final state former is the preferred one.

The use of the polarized beams provides an effective increase in luminosity[9] of one to two orders of magnitude and improve the systematic uncertainties related to measurements without polarization. Therefore, at *SLC* considerable effort has been made to use the longitudinally polarized electron beams by making use of a polarized source, a spin rotator system and a system to monitor the beam polarization which is composed of two polarimeters (Möller $\frac{\delta P}{P} \approx 5\%$ and Compton $\frac{\delta P}{P} \approx 1\%$) in the electron beam extraction line. The longitudinal polarized beams (45%) of the *SLC* are expected to provide most stringent test of the SM through the measurements of asymmetries, in particular, left–right or polarization asymmetry.

- Definition of the Various Asymmetries:

  In the following will be defined various type of asymmetries.

  a) Unpolarized Forward–Backward (FB) Asymmetry;

  The forward–backward asymmetry, $A_{FB}$, for the process $e^+e^- \to f\bar{f}$, is defined by the expression,

$$A_{FB} = \frac{\sigma_{forward} - \sigma_{backward}}{\sigma_{forward} + \sigma_{backward}} \tag{2.11}$$

  where $\sigma_{forward}$ and $\sigma_{backward}$ are the cross sections for the fermion produced in the forward and backward hemisphere with respect to the $e^-$ axis. $A_{FB}$ is expected to be non zero due to parity violation in $Z^0$ decays.

  b) Polarized Forward–Backward Asymmetry;

  The sensitivity of the FB asymmetry is enhanced when polarized beams are used. We can define the polarized FB asymmetry as follows;

$$A^{pol}_{FB} = \frac{(\sigma_{LF} - \sigma_{RF}) - (\sigma_{LB} - \sigma_{RB})}{\sigma_{LF} + \sigma_{RF} + \sigma_{LB} + \sigma_{RB}} \tag{2.12}$$

  where $\sigma_{LF(RF)}$ is the cross section for producing the fermion forward with left(right) handed incident electrons.

  c) Left–Right (LR) Asymmetry;

  $A_{LR}$ can be measured by the sum of all final states and it is given as

$$A_{LR} = \frac{\sigma_L - \sigma_R}{\sigma_L + \sigma_R} \tag{2.13}$$

where $\sigma_L$, $\sigma_R$ are the total $e^+e^-$ cross sections with left and right handed electrons. If we write $A_{LR}$ in terms of vector and axial–vector couplings of the fermions to the $Z^0$ we obtain

$$A_{LR} = \frac{2v_e a_e}{v_e^2 + a_e^2} \cdot P \tag{2.14}$$

where $P$ is the polarization of the incident electron beam. Note that, $A_{LR}$ depends only on the incident electron couplings. If we rewrite this expression in terms of $sin^2\Theta_w$ as

$$A_{LR} = \frac{2(1 - 4sin^2\Theta_w)}{1 + (1 - 4sin^2\Theta_w)^2} \tag{2.15}$$

we observe that $A_{LR}$ is very sensitive to $sin^2\Theta_w$,

$$\delta sin^2\Theta_w = 1/8 \cdot \delta A_{LR}.$$

In Fig. 2.1 are shown the FB and LR asymmetries versus $sin^2\Theta_w$ and $M_Z$.

Because $A_{LR}$ depends on the total cross sections, systematic errors related to the final state are minimized and the error on $A_{LR}$ is dominated by statistics

$$\delta A_{LR} \approx 1/\sqrt{N} \tag{2.16}$$

where $N$ is the total number of the observed $Z^0$ decays.
Fig. 2.2 shows the accuracy of the test of the Standard Model as a function of number of observed $Z^0$ decays. We note that, at high statistics only the measurement of $A_{LR}$ show a precision comparable with the $Z^0$ mass measurement.

In conclusion, the LR asymmetry is more sensitive to deviations from the Standard Model than the FB asymmetry, because the measurements of $A_{LR}$

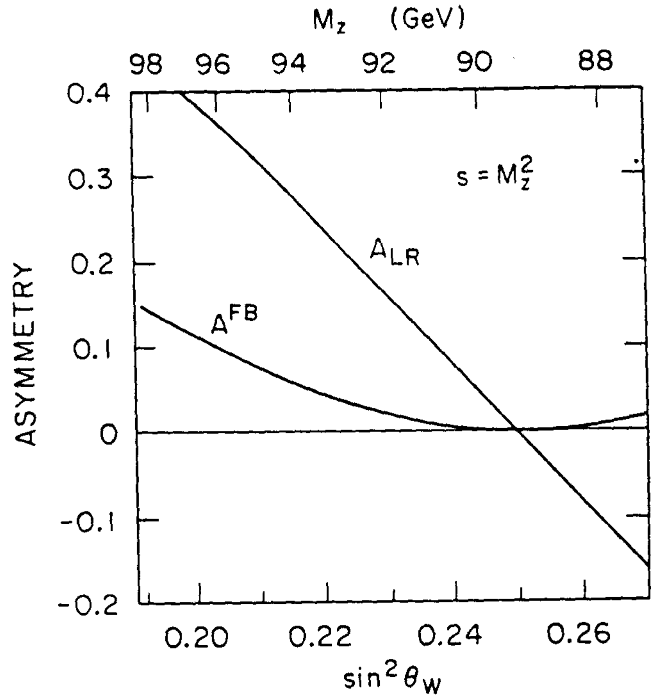


Figure 2.1. **The leptonic forward-backward asymmetry $A_{FB}$ and the left-right asymmetry $A_{LR}$ as a function of $sin^2\Theta_w$ and $M_Z$.**

makes use of all the observable channels. In addition, the energy dependence of $A_{LR}$ is small around the $Z^0$ peak and also the effect of the QED radiative corrections is rather small. Therefore, once $M_Z$ will accurately be measured, $A_{LR}$ can be used to set new limits on the top and Higgs masses.

The precise measurements of these asymmetries will benefit from the $4\pi$ coverage of *SLD* experiment both with precise electromagnetic and hadronic calorimetry and good charged particle identification.

### *2.2.2 Heavy Quark (B) Spectroscopy*

*B* spectroscopy is one of the most interesting aspects of the $Z^0$ physics. *SLD* is well suited to study *B* physics thanks to its vertex detector, particle separation capability and small beam pipe which all are crucial for a good *B* spectroscopy.

The major experimental results on *B* decays come from CLEO (Cornell–USA) and ARGUS (Desy–Hamburg) which collected good samples of $B^{\pm}$, $B_d$ decays

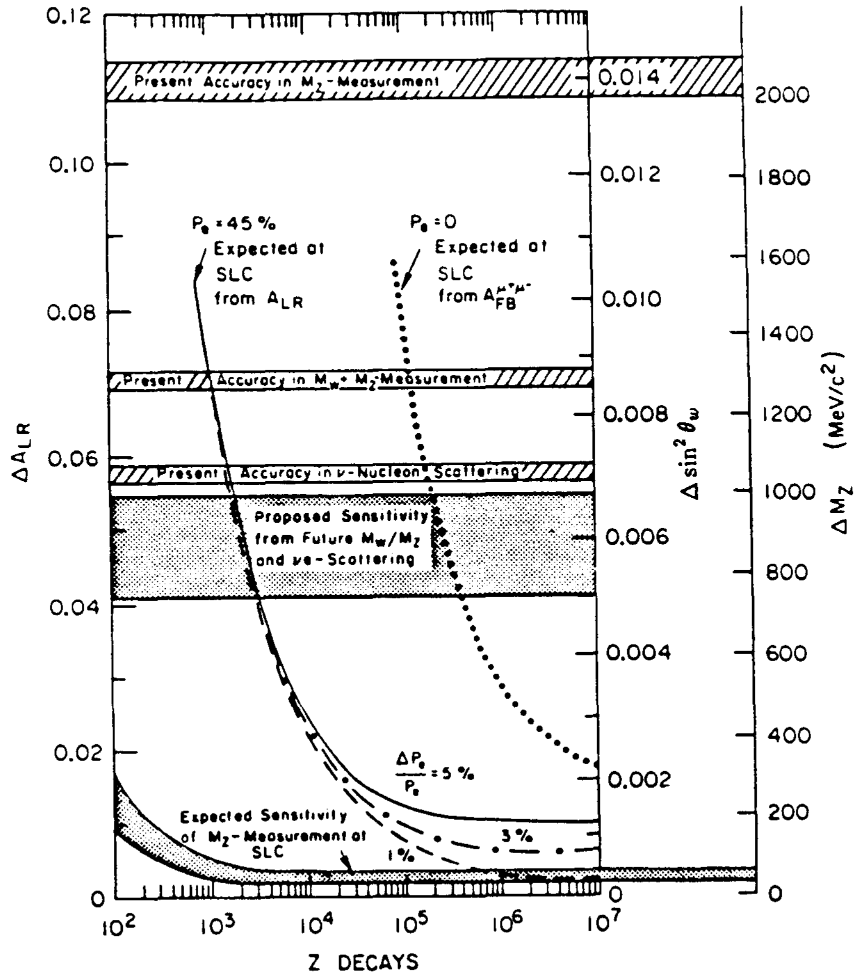


Figure 2.2. **The expected uncertainty of a measurement of $A_{LR}$ and corresponding uncertainty on $sin^2\Theta_w$ and on the mass of the $Z^0$ are shown as a function of the number of events used. The beam polarization is taken to be 45% and $M_Z$ is assumed to be 92.5 GeV.**

but smaller number of charmed ($B_c$) decays. Because of approximately 14% of the $Z^0$ decays into $b\bar{b}$ pairs, there are many interesting topics to explore in $B$ physics at a $Z^0$ factory like *SLC*. The *SLD* plans to study important part of them at the $\Upsilon$(4S) resonance bound state of the $b\bar{b}$ quarks which is above threshold for the production of $B$ meson pairs. These topics can be listed as the following:

a) measurement of the lifetimes of $B^{\pm}$, $B_d^0$, $B_s^0$, in particular $\tau^+/\tau^0$=$\tau(B^+)/\tau(B_d)$, and their semileptonic decay rates. The purpose of *SLD* is to measure the lifetimes with $\leq 10\%$ of accuracy from $10^5$ $Z^0$ events,

b) study of $B_s$ (mass measurements) and $B$–baryons,

c) study of hadronic decays like $B \to \pi\pi$, $K\pi$, $\psi K_s$ which could give the informations for a better understanding of CP violation,

d) study of rare decays like $B \to \psi X$ and $B \to K\mu\bar{\mu}$,

e) measurement of the K–M matrix element $V_{cb}$ in semileptonic decays as $B \to De\nu$ and $D^*e\nu$.

In order to obtain precise information on these topics approximately 100,000 (of which about 14,000 are expected to be $b\bar{b}$) $Z^0$ are needed.

*2.2.2.1 $B^0$–$\bar{B}^0$ Mixing*

Neutral mesons composed of charge conjugated quark pairs, eigenstates of strong interactions, may oscillate between the particle and the antiparticle and therefore flavor changing weak interactions can mix these states[10]. This mixing can be measured by observing the fraction of produced neutral $B\bar{B}$ pairs which decay as $\bar{B}\bar{B}$ or $BB$. The mixing parameter $r$ is defined as

$$r = \frac{\bar{B}^0 \to B^0 \to Xl^+\nu}{\bar{B}^0 \to Xl^-\nu} \qquad (2.17)$$

where $l$ is the lepton. The average value for $r$ obtained from the CLEO and ARGUS collaborations is $0.18 \pm 0.05$.

The capabilities of *SLD* with 45% polarized electron beam should allow to measure the time dependence of $B_d$ and $B_s$ mixing with about $10^5$ $Z^0$ events using polarization and inclusive vertex tagging techniques[4] which consists of looking for a chain of two decay vertices.

*2.2.3 Higgs Boson*

In the SM masses of weak bosons, quarks and leptons arise from the interactions of these particles with Higgs bosons generated by the spontaneous symmetry breaking mechanism.

In a high energy $e^+e^-$ collider the main processes for neutral Higgs boson production are $e^+e^- \rightarrow H^0 Z^0$ and $e^+e^- \rightarrow H^0 \nu_e \bar{\nu}_e$. Fig. 2.3 shows the Feynman diagrams for these processes. The cross section of $e^+e^- \rightarrow H^0 \nu_e \bar{\nu}_e$ is larger and therefore this channel gives the largest signal/background ratio.

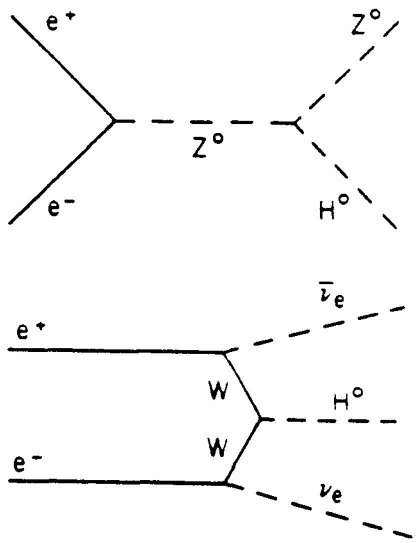


Figure 2.3. **Feynman diagrams for the Higgs production processes at a high energy $e^+e^-$ collider.**

In *SLD* the combined information of the tracking chambers and the calorimetry will minimize the background effects on the signal, maintaining the high efficiency for detecting Higgs particles. In a recent MonteCarlo study[11] has shown that *SLD* could easily detect the standard Higgs bosons with masses up to about 25 GeV/c$^2$ using a missing energy signature.

### *2.2.4 Neutrino Counting*

Another interesting topic for *SLD* is the measurement of the $Z^0$ decay into weakly coupled particles with masses less than half of $Z^0$ mass like additional neutrino generations or supersymmetric neutral particles. The ways to perform these measurements are the following[12];

a) comparison of the expected integrated decay rate of the $Z^0$,

b) determination of the "invisible" $Z^0$ by measuring the difference between the total width and the width of $Z^0$ decaying into charged leptons and hadrons. The difference is the direct measurement of the $Z^0$ width into neutral particles,

c) measurement of the cross–section for the process $e^+e^- \rightarrow Z^0 \rightarrow \nu+\bar{\nu}+\gamma$ where the single detectable $\gamma$ is the signature. Existence of an additional neutrino type leads to an increase of $\approx 30\%$ of the cross–section,

d) alternatively one can measure the branching ratio;

$$\frac{e^+e^- \rightarrow \nu + \bar{\nu} + \gamma}{e^+e^- \rightarrow \mu^+ + \mu^- + \gamma} \tag{2.18}$$

that is less sensitive to the knowledge of QED radiative corrections.

## .....AND BEYOND THE STANDARD MODEL,

### *2.2.5 Search for New Heavy Quarks, Leptons and $Z^0$'s.*

In any new colliding beam experiment exploring a new energy range, the search for new particles and states is one of the most interesting physics topics. These new particles (leptons or quarks) could be either members of standard sequential generations or object with more exotic quantum numbers.
If they exist, new "sequential leptons" should decay via charged weak current. In the following we see some possible scenarios for these leptons:
a) if $M_L > M_{\nu_L}$ and both are $< M_Z/2$ ,where $\nu_L$ is stable (without mixing) then $L^- \rightarrow W\nu_L$ decay occur and it is detectable via neutrino counting (charged lepton case),
b) if only $M_{\nu_L}$ or $M_L$ is $< M_Z/2$ then via mixing $\nu_L \rightarrow W^+l^-$ process occur (neutral lepton case). The decay rate of this process is proportional to the mixing parameter $|U_{Ll}|^2$.

The existence of fourth generation weak isospin -1/2 "sequential quark", known as "$b'$" quark, can be searched in *SLD* if it has $M_{b'} < M_Z/2$. In this case it could decay to a light quark and virtual W boson. Possible signatures for this process are the hadronic or leptonic decays of W boson. The first method (hadronic W decay) offers higher statistics while the second one is less efficient but leads to a completely clean signal[13].

As a conclusion, with $10^4$ $Z^0$ events *SLD* will be able to set the limits[14] on the sequential lepton's mass at about 40 GeV/c$^2$ and on the sequential $b'$ mass at about 45 GeV/c$^2$.

If they are sufficiently light, in *SLD* it could be possible to observe also additional $Z^0$s. The expected effects due to these new $Z^0$s includes the shifts of $M_Z$ or $\Gamma_Z$, modification of the hadronic and leptonic partial widths of the $Z^0$, creating measurable effects on the FB and polarized LR asymmetries.

### *2.2.6 Search for Supersymmetric and Technicolor Particles*

Finely segmented hadron calorimeter is required also in this case to reconstruct the jet–jet effective masses due to the decay of technicolor particles into heavy quark pairs such as $b\bar{b}$ or $t\bar{t}$. In the case of supersymmetry R–parity quantum number is expected to be conserved. Therefore, supersymmetric quarks and leptons will have a photino, gluino or Goldstino among their decay products which presumably do not interact with the detector. Thus a large solid angle hadron calorimeter is very important to provide the signature of large missing energy carried off by the neutral particles.

## 2.3 THE *SLC* MACHINE

The *SLC* is a new electron–positron accelerator which make uses of the existing 3 km long SLAC linac with some modifications. The modifications are in particular, the addition of two collider arcs and the increase of the beam energy from 24 GeV to 50 GeV (center–of–mass). The *SLC* should be able to achieve a luminosity of few $\times$ $10^{30}$cm$^{-2}$sec$^{-1}$. Fig. 2.4 shows the *SLC* layout.

A cycle of the *SLC* begins just before the pulsing of the linac[15]. At this time, the electron and the positron damping rings contain two bunches of about

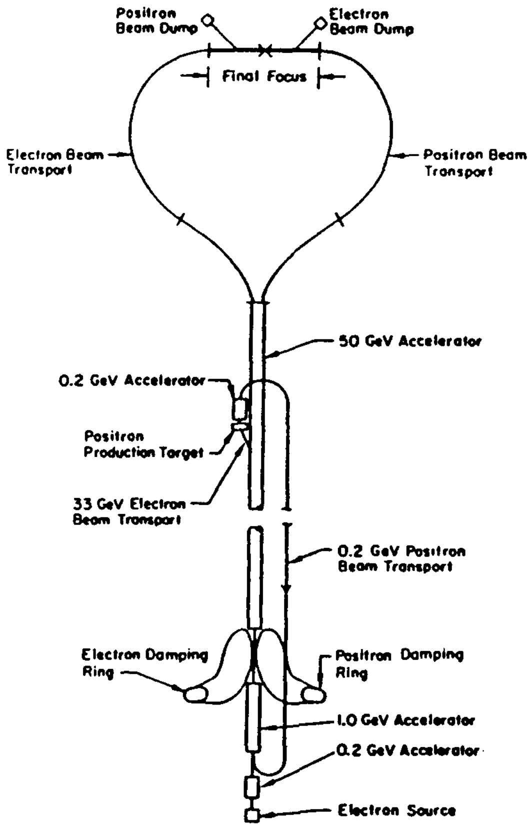


Figure 2.4. The layout of *SLC.*

$2.5\times10^{10}$ particles with energies of 1.2 GeV. One of the two positron bunches is then extracted from the damping ring and passed through a pulse compressor that reduces the bunch length from about one centimeter to about one millimeter size, after which the bunch is injected into the linac. Next, both electron bunches are extracted from the electron damping ring and injected behind the positron bunch. The distance between bunches is about 17.6 meters in the linac.

All three bunches of particles are then accelerated through the linac. At the two–thirds point, the rearmost electron bunch is extracted in order to produce the positrons. This 33 GeV beam is focused onto the target, which is a converter plate made of Tantalum–Tungsten. The electrons lose energy in the plate by giving off bremsstrahlung radiation; the bremsstrahlung photons produce $e^+e^-$ pairs and the positrons are collected by a focusing solenoid and accelerated to

200 MeV in a 1.5 meter long accelerator.

At the end of the linac, the two opposite charge bunches are separated by a DC magnet and passed through a transport system which matches the linac to the main collider arcs. At the interaction point, the electron and the positron beams are finally brought into collision by a sophisticated system of optics, called final focus.

## 2.4 Description of the Detector

In this section we will describe the main detector components of *SLD* starting from the inner part where the collisions occur to the outer parts.

### *2.4.1 Vertex Detector*

In order to have complete information about the decays, as well as good particle identification, efficient and precise tracking detectors are required. The vertex detector is the one of the two tracking components of *SLD* which is designed for the precise measurements of primary vertex and secondary vertices due to the decay of heavy quarks, and provides the reconstruction of the charged particle trajectories over 97% of solid angle.

The detector is composed of a total of 232 low temperature charged–coupled–devices (CCDs) which are placed in two barrel arrays B1, B2 (see Fig. 2.5) to cover a region very close to beam pipe; the space resolution of the detector is $\sigma$=5 $\mu$m.
The purpose of the detector is the accurate measurements of tracks within 1 to 2 cm of the interaction point, so to complete the information of an event including the determination of the number of vertices.

The lengths and radii are, 72 and 96 mm for B1 array, 12 and 24 mm for B2 array respectively, while the polar angle coverage of the detector is $\theta_{min} = 27°$.

The individual CCD has an efficiency of about 98% for the minimum ionizing particles with a spatial resolution of 40 $\mu$m between two tracks. Each

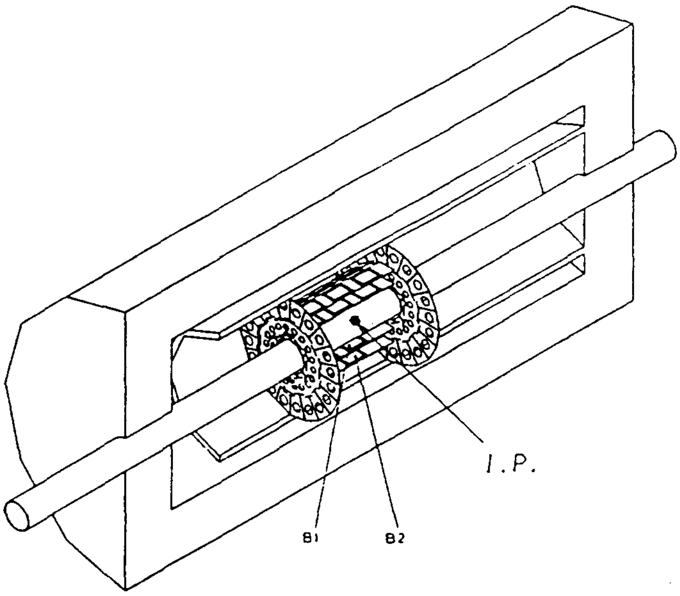


Figure 2.5. Layout of *SLD* Vertex detector. The two barrel arrays of CCDs, B1 and B2, surround the 10 mm radius beam pipe, and centered on the interaction point IP.

CCD covers approximately $9 \times 13$ mm$^2$ of area with $385 \times 578$ pixels (22 $\mu$m $\times$ 22 $\mu$m each pixel) and need to be operated below 200° K which is provided by a flow of cold nitrogen.

### *2.4.2 The Central Drift Chamber (CDC)*

The central drift chamber (CDC) is the other charged particle tracking detector of *SLD* which is a cylindrical annulus with an inner radius of 20 cm, outer radius of 100 cm and a length of 200 cm centered about the interaction point.

The CDC consists of 180 cm long wires placed parallel to the beam axis and arranged in 10 cylindrical superlayers of which 4 are axial and 6 are at small angles. Each layer is divided azimuthally into cells of approximately 6 cm wide and each cell has eight sense wires separated by two guard wires. In Fig. 2.6 the configuration of the basic drift chamber cell is shown.

The field wires provide a uniform electrostatic field ($\approx$ 1kV/cm) directed towards the sense wires. When a minimum ionizing particle passes through the CDC, it ionizes the gas (92%)$CO_2$+(8%)Iso molecules and ionization electrons drift with a constant velocity ($\approx$ 9 mm/nsec) along on the field lines toward the sense wires.

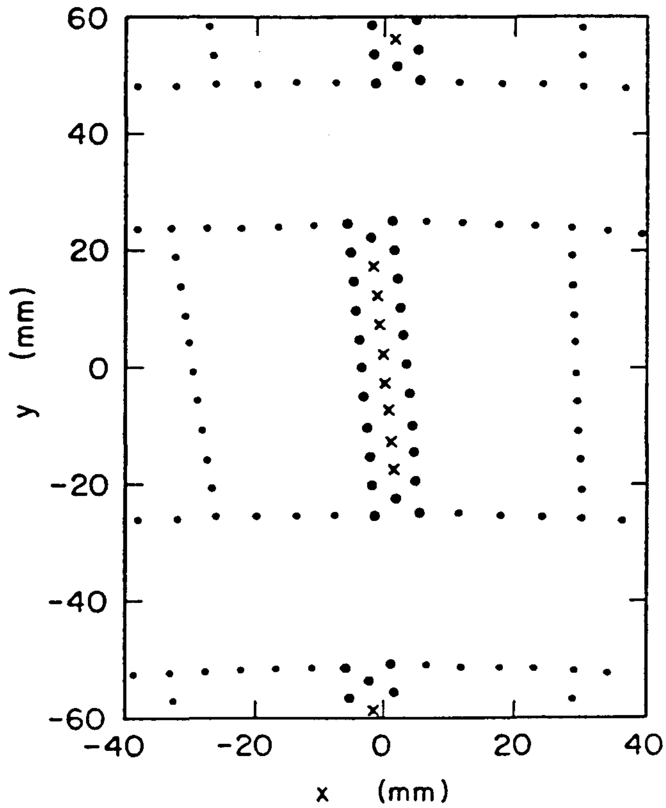


Figure 2.6. **The drift chamber cell design. The sense wires are represented by x, the guard wires by • and field wires by ·.**

The drift times measured by TDCs, are converted first into the drift distances and then into the fitted tracks. The hit position along the wire (z coordinate) is obtained by using the charge division. Fig. 2.7 shows a schematic view of the drifting electrons in a cell when traversed by a incoming charged particle.

The momentum resolution of the CDC which accomplished by a MonteCarlo simulations showed that over the interval $15° < \theta < 165°$ and including the

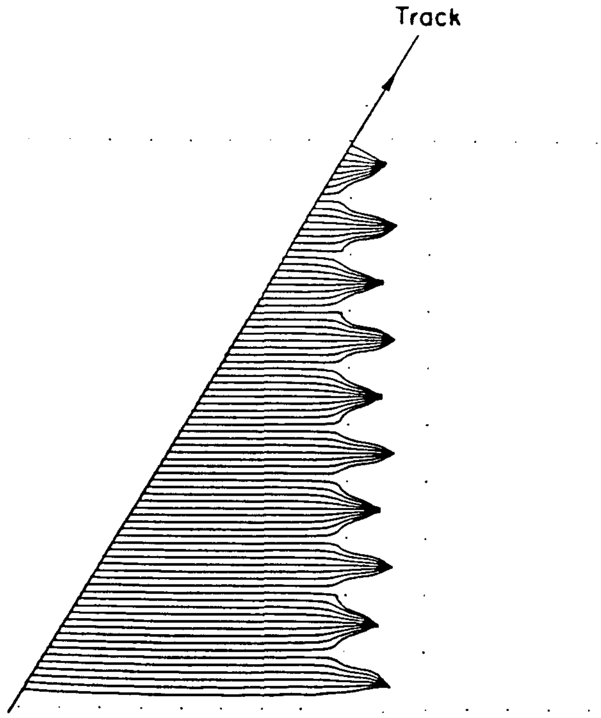


Figure 2.7. The drift path of the electrons when a charged particle traversing the cell diagonally.

CCD's can be parameterized as

$$\frac{\Delta_p}{p} = \sqrt{(.01)^2 + (.0025p(GeV/c^2)} \tag{2.19}$$

and,

$$\frac{\Delta_p}{p} = \sqrt{(.01)^2 + (.0015p(GeV/c^2)} \tag{2.20}$$

without the CCD constraint.

The tests realized with the CDC prototype[16] showed that in addition to its tracking capabilities, it is also possible to perform $e/\pi$ separation using the pulse heights up to at least 7 GeV/c$^2$ of momentum by measuring dE/dX in the CDC. The tracking spatial resolution achieved with a single wire of the prototype is $\sigma$=55 $\mu$m.

### 2.4.3 *Čerenkov Ring Imaging Detectors (CRIDs)*

The Čerenkov Ring Imaging Detector (CRID) will provide almost complete particle identification over 90% of the solid angle at the *SLC* using the barrel and the endcap segments[17]. The combination of the information achieved by the high precision vertex detector together with the final state particles identification, will give the possibility of having clean signals with high efficiency. The CRID, by making use of its liquid and gaseous radiators, will provide $\pi/K/p$ separation up to 30 GeV/$c^2$ and $e/\pi$ separation up to 6 GeV/$c^2$.
The operational principle of the CRID is the following:

When a charged particle passes through the thin liquid or gas radiator of the CRID, it produce a Čerenkov light. The light produced in the liquid or gas radiators is sent directly or focused back by spherical mirrors into a photon detector which is located between the radiators.
The photons in this detector create two electron ring images (one from each radiator) of which their radius are determinated by the velocity of the incoming charged particle and by the refraction index of the medium. In Fig. 2.8 the radiator system of the CRID and the ring image examples are shown.
The electrons created by the photoionization effect, drift towards the pick–up end of the photon detector with a constant velocity given by the applied uniform electric field. From the drift time of the photoelectrons one can reconstruct their initial coordinate and, the measurement of the ring radius can be determined the momentum of the incoming particle.

The 40 $C_6F_{14}$ liquid radiator trays, drift boxes and mirror arrays of the barrel CRID Vessel are contained in a cylindrical shell together with the $C_5F_{16}$ radiator gas. The inner and outer radii of the cylindrical shell of the CRID are 102 cm and 177 cm respectively and it is located between the CDC and Liquid Argon Calorimeter (LAC) of *SLD*.
The endcap CRIDs have the same geometry of mechanically separated wedge shaped sectors as the barrel. Fig. 2.9 shows a schematic view of the CRID's

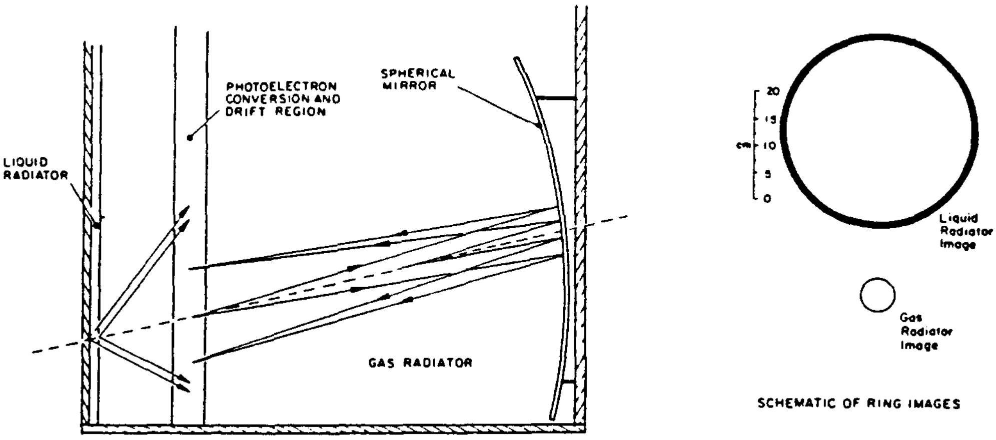


Figure 2.8. **Ring images produced at 90° in the liquid and gas radiators (right); and the two radiator system of the CRID (left).**

barrel and endcap sections while in Fig. 2.10 we see the particle separation of the CRID at 90°. On the vertical scale, the particle separation is given in terms of the standard deviations.

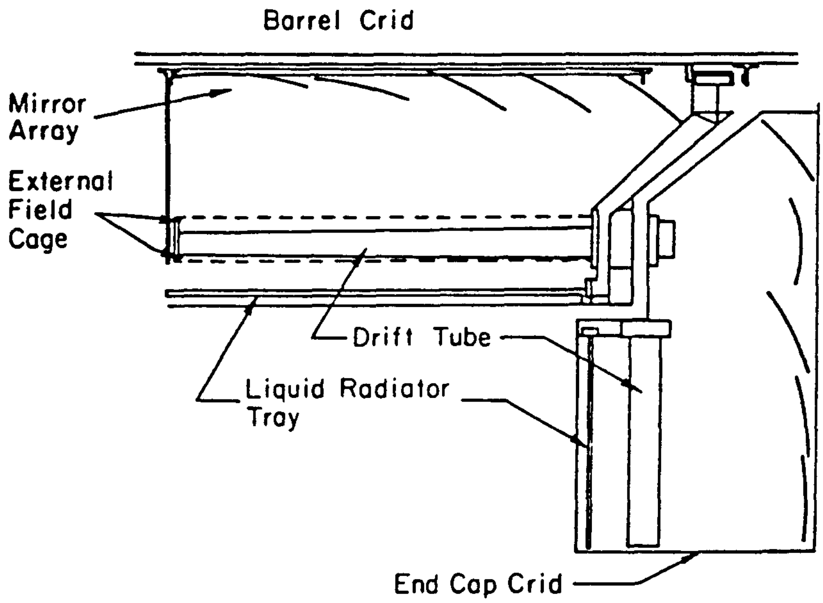


Figure 2.9. **The barrel and the endcap sections of CRID seen longitudinally.**

### *2.4.4 Calorimeters of SLD*

The past experience of $4\pi$ detectors like UA1 and UA2 show that how is

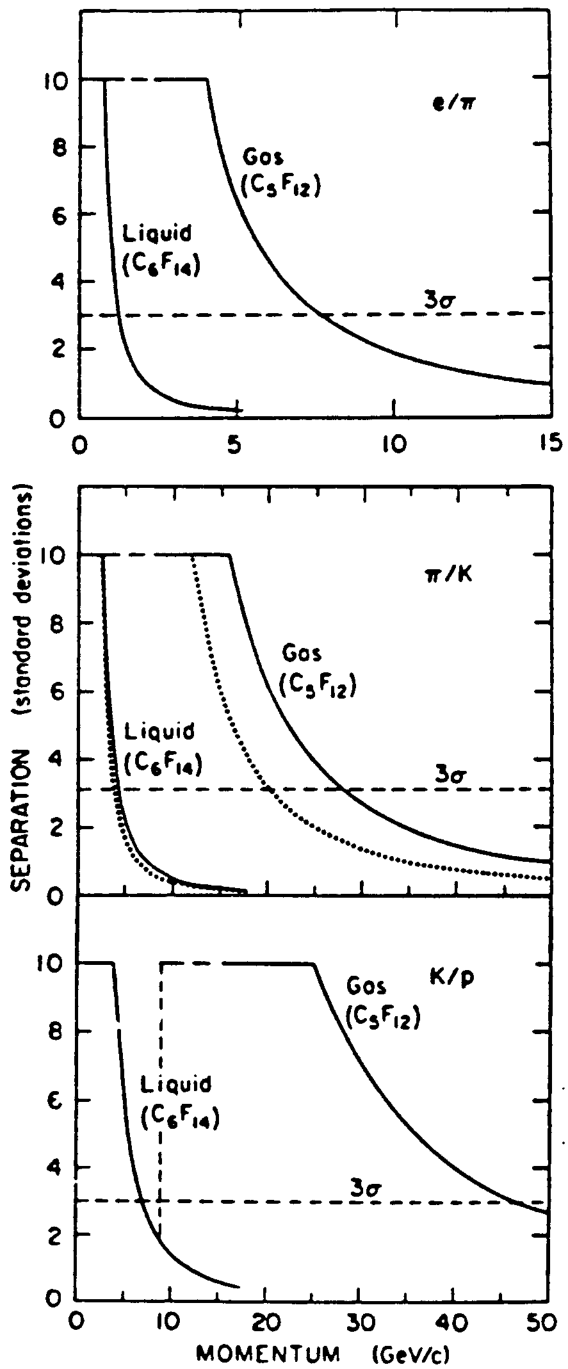


Figure 2.10. **Particle capabilities of the CRID at 90° versus momentum are shown for the liquid and gas radiators.**

important to have a good energy resolution coupled to complete coverage of the solid angle.

One of the goals of *SLD* is in fact to be a "Hermetic" detector, that is, to be able to accurately measure the electromagnetic and hadronic energy over the entire solid angle. To fulfill this goal, we should not have dead regions from which the energy may escape. The *SLD* calorimeter constituents[18] are, first, LAC which is a conventional argon sampling calorimeter that can absorb most of the energy from a $Z^0$ event. The LAC is followed by a gas sampled iron calorimeter, WIC, which is designed to detect the energies of the hadron shower tails and for the muon tracking. The WIC also serve as magnetic flux return.
The 0.6 $\lambda$ thick aluminum solenoid coil is located between the two calorimeters which are described in the following sections.

*2.4.4.1 The Liquid Argon Calorimeter (LAC)*

The LAC is placed inside the coil, which is a high resolution electromagnetic and hadronic calorimeter. The LAC measures the energies of the particles interacting in its lead–argon active volume by collecting the ionization charge produced in the liquid argon by the particles created in the radiator structure[19]. The total coverage of the solid angle for electromagnetic and hadronic showers are $\approx$ 99% and $\approx$ 95% of $4\pi$ sr, respectively.

The main part of the LAC is the barrel in which the particles leaving the interaction point at large angles can be detected. Two endcaps are provided in order to detect the particles with small angles.

The barrel LAC is composed of the stacks of the absorber metallic plates separated by a few mm of liquid argon gaps and the stacks are then inserted into a cryostat. The total thickness of the electromagnetic section of the LAC is $X_0 \approx 21$ and the total interaction lengths for the electromagnetic and the hadronic sections are $\lambda \approx .85$ and $\lambda \approx$ 2.00 respectively. In Fig. 2.11 shown is the schematic of the LAC barrel and endcap.

In the hadronic section of the LAC contained is approximately 80% of the overall hadronic showers with energies up to 20 GeV. The total energy

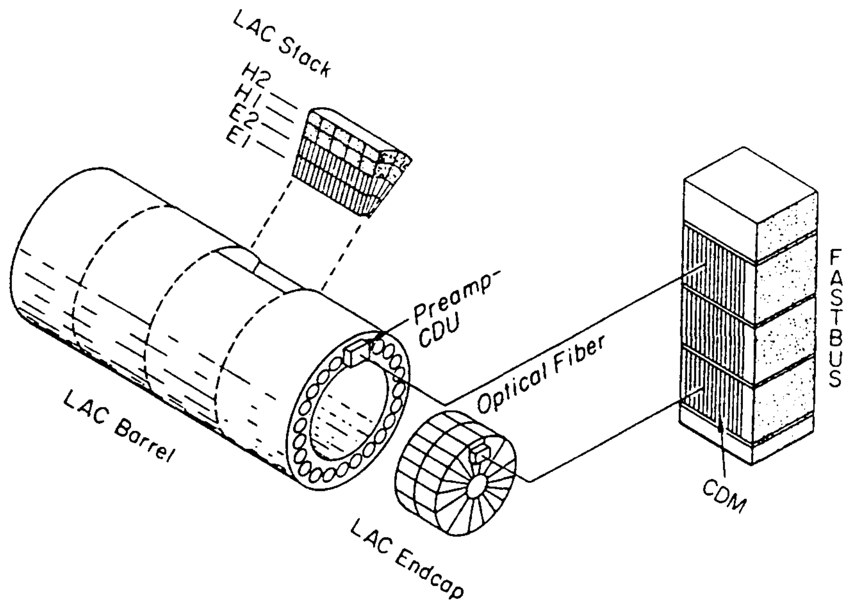


Figure 2.11. **Schematic of the LAC barrel and endcap with readout and trigger system.**

resolution of the LAC is expected to be better than $\sigma$(E)=55%$\sqrt{E(GeV)}$ while the electromagnetic energy resolution is about $\sigma$(E)=8%$\sqrt{E(GeV)}$. Furthermore, good position resolution for electromagnetic showers is obtained from the transverse shower profiles. Discrimination between the pions and the electrons is achieved by comparison of the energy deposition profile in the LAC and by signals in the CRID.

The calorimeter stacks are divided into readout towers that project back to the beam intersection point. In the azimuthal direction the angular segmentation for the hadronic sections is $\Delta\Theta_{polar} \times \Delta\Phi_{azimuth}$ = 66 mrad $\times$ 72 mrad and for the electromagnetic section is 33 mrad $\times$ 36 mrad. The choice of the segment sizes allow a good position resolution and high efficiency in separating near jets. Endcap LAC has the same configuration of the barrel and it covers the region of polar angle below 35°.

### *2.4.4.2 Warm Iron Calorimeter (WIC)*

Outside the magnet coil is placed the WIC that measures the $\approx$ 15% of the hadronic energy with a resolution of about $\sigma(E)$=80% $\sqrt{E(GeV)}$ which escapes the LAC. It serves a tracking device and muon identifier as well as the magnetic flux return because of its large iron structure. The total depth of the 14 iron plates of thickness 5 cm each, is about four interaction lengths[20]. These plates are separated by 3.2 cm gaps and gaseous detectors are inserted are into the gaps LSTs, sandwiched between the external readout electrodes (strips & pads). The cathodic signal is obtained by the induction of streamer discharge caused by the charged particles crossing the LST's cells.

In Fig. 2.12 shown is the cross section of a typical barrel octant together with the arrangement of the various chamber layers. The detailed description of the operational principles, construction and performed studies on the WIC chambers and LSTs can be found in the Chapters 4, and 6.

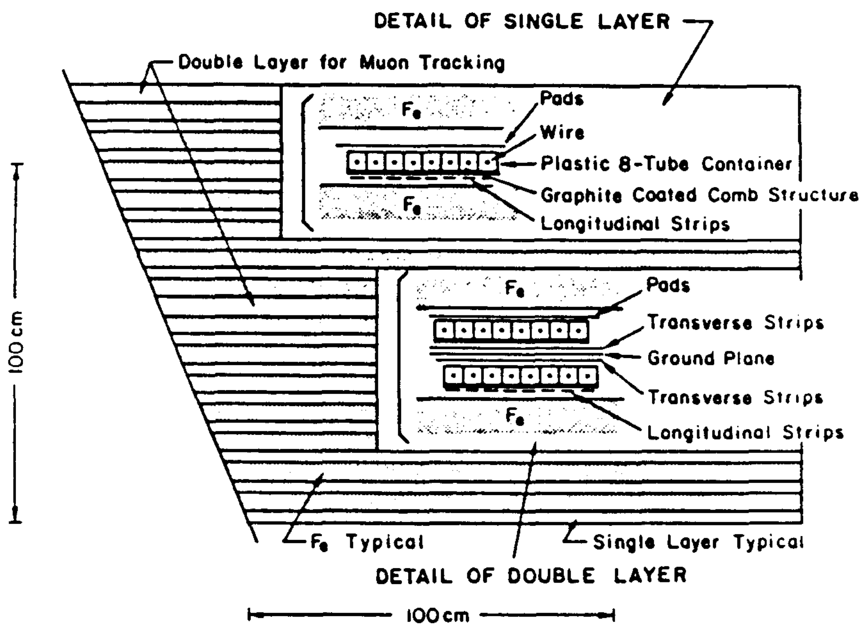


Figure 2.12. Cross section of typical barrel octant of the WIC.

The WIC consists of two parts; barrel and endcaps.

Barrel: Each of the eight barrel sections contains 14 iron plates sandwiched with 17 planes of LSTs. Both the $7^{th}$ and $14^{th}$ planes contain a double layer of LSTs with readout strips parallel (X) and perpendicular (Y) to the wires axis of which the (Y) strips provide to have the second dimension for the readout improving the tracking capability of the WIC.

Fig. 2.13 shows the longitudinal electrodes (strips) which are made of 1.6 mm thick fiberglass sheets laminated with 40 $\mu$m copper on both sides. One side is routed in order to obtain the readout channels along the wires while the other side is used as ground plane. These strip foils are then glued on the top side of the WIC chambers. The number of LST in each layer of the barrel section varies from 32 to 43 going from the innermost to the outermost layer and the total number of LST in the eight barrel sections is 40,336.

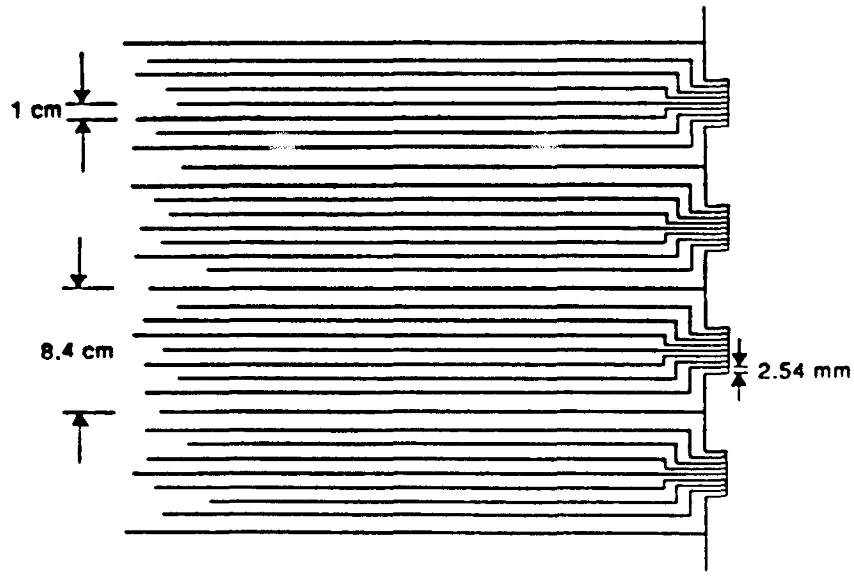


Figure 2.13. Layout of the longitudinal (X) strips.

The opposing electrode sheet is an array of quadrilateral pads which are made of 0.8 mm thick fiberglass with a 40 $\mu$m thick copper foil attached on one side with sizes of 20 to 30 cm. The pads are connected to form the projective "towers" and their signals are summed accordingly. Fig. 2.14 shows a typical pad pattern for the barrel and endcap WIC. The size of the pad shapes is chosen by the intersection of the WIC planes with planes of the LAC barrel towers.

The readout of the pads makes use of an analog system; the WIC towers

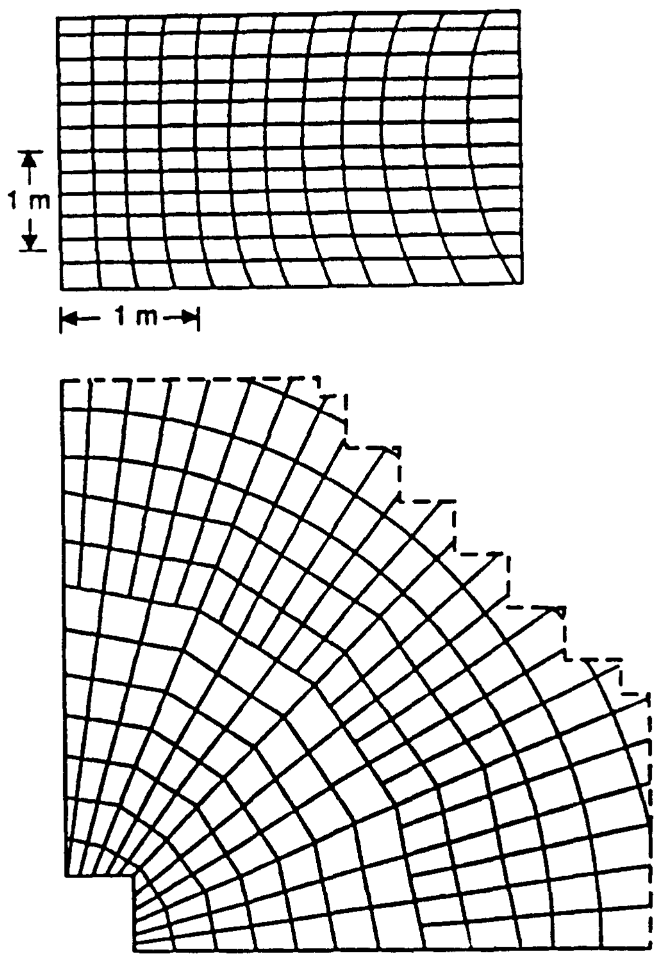


Figure 2.14. Pad structure of the barrel (upper) and of the endcap regions (lower).

are divided into two segments (inner and outer) in depth and each segment has seven layers each except for the outer barrel segment. The signal of a segment tower is integrated over 5 $\mu$s by a hybrid preamplifier, read by a sample–and–hold circuit and then digitized by an ADC. Approximately 8,600 channels are needed for the pads.

The strips[21] readout is digital with a pulse height threshold of the order of 1 mV. The data acquisition chain for the WIC strips is the following; the signals of the eight strips channels of a LST are first sent to preamplifiers and from the preamplifiers to discriminators and the discriminator outputs are then sent to shift–registers. All these components are packaged in a single hybrid and four hybrids are packaged in 32–channel boards (produced by SGS). One layer then contains typically 10 daisy–chained boards. The total digital readout channels of the WIC is approximately 90,000. Detailed information on the WIC strips readout electronics can be found in reference[21].

The solid angle coverage of these two systems (pads & strips) is 99.2% of $4\pi$ and the total covered area is about 4500 $m^2$. In Table 2.1 are summarized the general features of the *SLD*.
In section 6.9 the results of the WIC prototype (beam) test will be presented.

## 2.5 The *SLD* Data Acquisition System

The large amount of *SLD* readout channels has required the development of a new generation[22] readout electronics.

*SLD* will use a total of about 200,000 readout channels. Approximately 50,000 are waveform recording channels, needed for the drift chambers and CRIDs in order to perform time and charge division measurements with good multihit capacity. Similarly, about the same amount of sample–and–hold[23] channels are needed for the calorimeters and finally approximately 100,000 channels are used for the strip readout. These systems, with appropriate preamplification and shaping are mounted on the detector subsystems which are then communicated through analog fiber optics with the Fastbus processing modules.

The low repetition rate (180 Hz) of *SLC* makes it possible to have lowest level trigger rate with less than 10% of dead time[24] then allows approximately 50 msec for readout of the full detector system by the Fastbus modules. Fig. 2.15 shows the data acquisition system layout where the principal elements of the trigger system are also shown. The main component of the trigger system is the Trigger Processor (TP) which is an intelligent master that decides whether or not to store the data on the basis of drift chamber and calorimeters data and

Table 2.1. Summary of performance parameters of the *SLD*.

| | |
|---|---|
| **Drift Chamber System** | |
| Spatial Resolution ($\sigma$) | $\leq 100\ \mu m$ |
| Magnetic Field | 0.6 Tesla |
| Momentum Resolution | |
| $\sigma(1/p)$ measurement limit | $1.3 \times 10^{-3}\ (GeV/c)^{-1}$ |
| $\sigma(p)/p$ Coulomb scattering limit | $(1-2) \times 10^{-2}$ |
| Two-Track Separation | 1 mm |
| **Calorimetry** | |
| Electromagnetic | |
| Energy Resolution $\sigma_E/E$ | $8\% / \sqrt{E\,(GeV)}$ |
| Segmentation | $\sim 33$ mrad $\times$ 36 mrad |
| Angular Resolution | $\sim 5$ mrad |
| **Hadronic** | |
| Energy Resolution $\sigma_E/E$ | $\leq 55\% / \sqrt{E\,(GeV)}$ |
| Segmentation | $\sim 66$ mrad $\times$ 72 mrad |
| Angular Resolution | $\sim 10$ mrad |
| **Vertex Detector** | |
| Segmentation | $22\ \mu m \times 22\ \mu m$ |
| Precision Transverse to Line of Flight | $4 - 20\ \mu m$ |
| Two-Track separation | $40\ \mu m$ |
| **Particle Identification** | |
| $e/\pi$ | $1 \times 10^{-3}$ |
| $\mu/\pi$ (above 1 GeV) | $2 \times 10^{-3}$ |
| $K/\pi$ (up to 30 GeV) | $1 \times 10^{-3}$ |
| $K/p$ (up to 50 GeV) | $1 \times 10^{-3}$ |
| **Solid Angle Coverage** | |
| Tracking | 97% |
| Particle Identification | 97% |
| *EM* Calorimeter | $\geq 99\%$ |
| Hadron Calorimeter | 97% |

is responsible for the coordination of timing signals sent to the various elements of the detector electronics and of the acquisition system.

New developed VLSI circuits for the waveform recording (Analog Memorv Units, AMU) and calorimetry (Calorimetry Data Units, CDU), both having

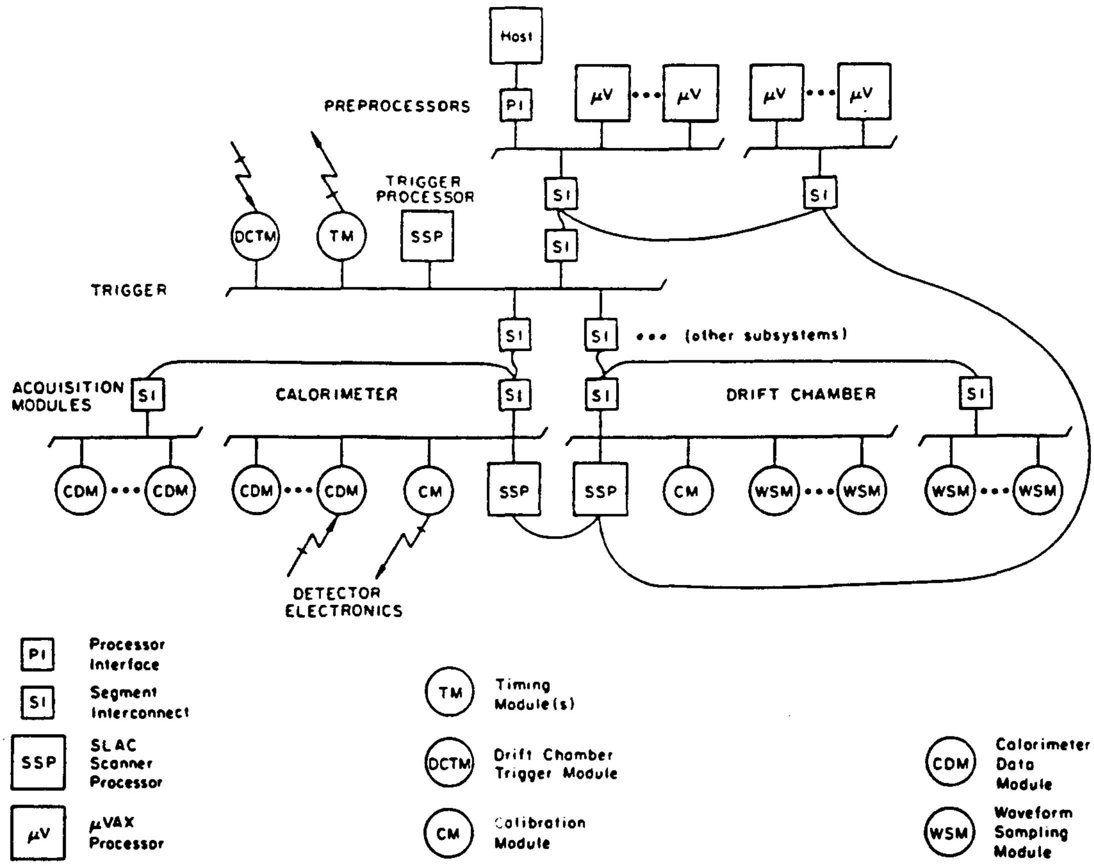


Figure 2.15. **Fastbus configuration of** ***SLD.***

1 MHz outputs, are multiplexed and received by the Fastbus modules that correct and compact the data before sending them to the programmable processors (SSPs) in each crate. The data passed over the Fastbus arrives to the central trigger processors which computes a trigger decision in about 2 ms. The subsequent data flows into the Fastbus VAXes first for the secondary trigger decision and finally to the on–line host computer (see Fig. 2.16) which is a VAX 8800. The host handles the data storage and the acquisition system control, and the monitoring and analysis of the data by accumulating the summary of the events and showing the event display. The monitoring and control of the various subsystems are provided by MicroVAXes.

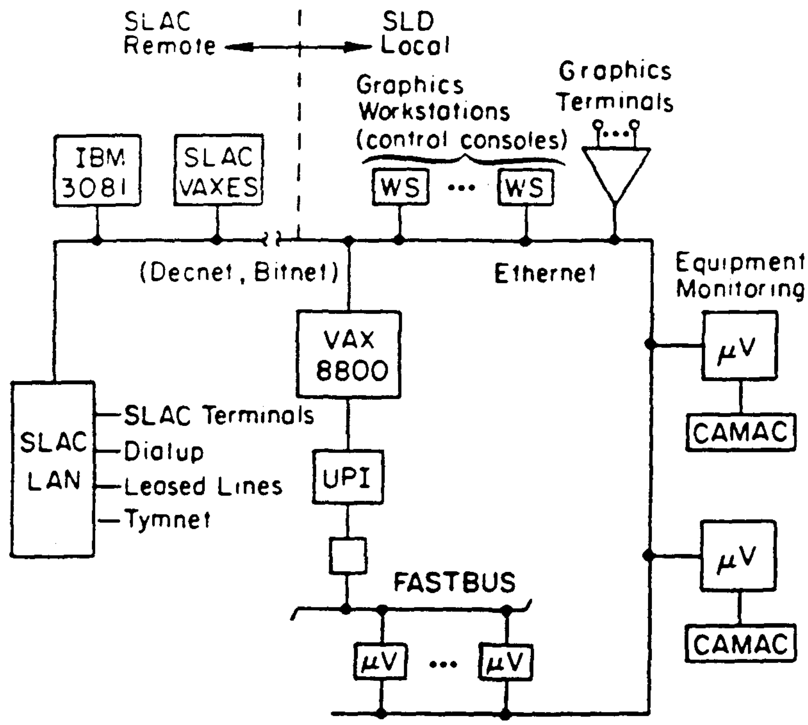


Figure 2.16. **Host computer configuration.**

# Chapter 3. Properties of Gas Detectors

## 3.1 INTRODUCTION

In this Chapter we will summarize, in general, the properties of gas detectors. We will also discuss in detail the limited streamer mode of operation and the LSTs which are used in the *SLD* WIC chambers.

## 3.2 PROPERTIES OF GAS DETECTORS

Before discussing the LSTs and their properties it is useful to recall some of the physical phenomenon involved in gaseous particle detectors, such as energy loss, primary and total ionization, drift of electrons in gases, and influence of the wire diameter on the detector operation. A more detailed treatment of the subject can be found in the F. Sauli's work[25].

### *3.2.1 Energy Loss*

An incoming charged particle, interacting with atoms or molecules in the gas, loses its energy due to this interaction. A formula that describes the average differential energy loss is given by Bethe–Block,

$$\frac{dE}{dx} = -K\frac{Z}{A}\frac{\rho}{\beta^2}\left(\frac{\log 2mc^2\beta^2 E_m}{I^2(1-\beta^2)-2\beta^2}\right), \qquad K = \frac{2\pi N z^2 e^4}{mc^2} \tag{3.1}$$

where N is the Avogadro number, $m$ and $e$ are the electron mass and charge, Z, A and $\rho$ are the atomic number, mass and density of the medium, I is the effective ionization potential which is in general a measured value for each material, $z$ is the charge of the particle and $\beta = v/c$ is the velocity of the electron. $E_m$ is the maximum energy transfer for each interaction,

$$E_m = \frac{2mc^2\beta^2}{1-\beta^2} \tag{3.2}$$

From measured values[25] of dE/dx for the mixture of Argon and Isobutane, one can compute the differential energy loss for the "standard mixture" used for the tests of the WIC LSTs chambers. The mixture used is one part of Argon and three parts of Isobutane, and the energy loss results

$$\frac{dE}{dx} = .75\frac{dE}{dx_{\text{iso}}} + .25\frac{dE}{dx_{\text{ar}}} = 3.99\text{KeV/cm} \tag{3.3}$$

The interval of momenta where all the particles lose the same amount of energy per unit length is called the minimum ionizing region. For most of the materials, the computed values[25] show that the minimum ionizing plateau is approximately between few hundreds MeV and about 10 GeV while above 10 GeV/c starts the relativistic rise of the energy loss (Fig. 3.1). In the case of the *SLD* hadronic calorimeter the operational energy range is up to about 10 GeV, thus does not involve the relativistic rise.

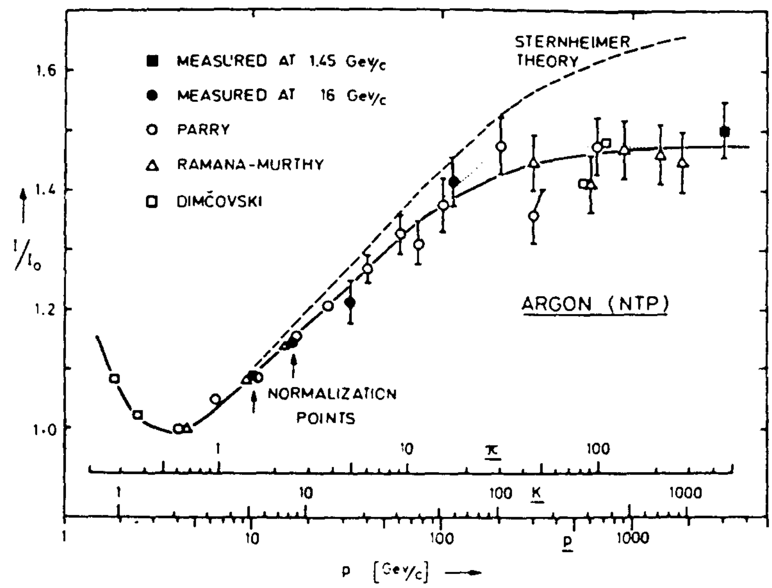


Figure 3.1. Relativistic rise of the energy loss in argon as a function of particle mass and momentum; operational range of the limited streamer tubes is in the minimum ionizing region.

### *3.2.2 Drift of Electrons & Mobility of Ions in Gases*

The velocity distribution and the mobility of electrons are very different from the gas molecules because of their low masses. The drift velocity of electrons is strongly related to the gas purity and the gas compositions[26]. In drift chambers, the drift time measurements are important to obtain the space coordinates of ionizing tracks. The mobility of electrons except in the case of very low fields, depends on the applied electric field. In fact, under the influence of an electric field electrons increase their energies between the collisions with the gas molecules. According to Townsend formulation, the electrons drift velocity can be written as

$$w = \frac{e}{2m} E\tau \tag{3.4}$$

where $\tau$ is the mean time between the collisions as a function of electric field $E$.

For ions mobility, the situation is different. Their drift velocity $w^{\pm}$ is linearly proportional to the reduced field $\frac{E}{P}$ ($P$ is gas pressure) up to very high fields. The mobility values ($\mu^{\pm}$) of the ions are constant for a given gas and can be expressed as

$$\mu^{\pm} = w^{\pm} \left(\frac{E}{P}\right)^{-1} \tag{3.5}$$

and their average energy does not change even with the very strong fields.

The mobility $\mu_i^+$ of ion $G_i^+$ in a mixture of gases $G_1, G_2, \ldots, G_n$ can be written by the Blanc's law:

$$\frac{1}{\mu^{\pm}} = \sum_{i=1}^{n} \frac{P_j}{\mu_{ij}^+} \tag{3.6}$$

where $P_j$ is the volume concentration of gas j in the mixture, and $\mu_{ij}^+$ the mobility of ion $G_i^+$ in gas $G_j$. It should be stressed that the electrons drift velocity does not play an important role on the localization of the avalanches.

### *3.2.3 Primary and Total Ionization*

As it was mentioned above, depending on the charged projectile energy, the applied electric field and the energy of the liberated electrons, it is possible that, the further ionizations after occur the initial ones. The total number of the produced ion pairs is then given by

$$n_T = \frac{\Delta E}{W_i} \tag{3.7}$$

where $\Delta E$ is the total energy loss in the considered volume of gas, and $W_i$ is the effective average energy needed to produce a pair. From the measured values[25] of $W_i$ in Ar and Iso ($C_4H_{10}$) we can compute the number of primary and total ion pairs in 1 cm of (Ar+Iso $\rightarrow$ 1+3) mixture at normal conditions,

$$\begin{aligned} n_t &= \frac{2440}{26}0.25 + \frac{4500}{23}0.75 = 170 \quad \text{pairs/cm} \\ n_p &= 29.4 \times 0.25 + 46 \times 0.75 = 42 \quad \text{pairs/cm} \end{aligned} \tag{3.8}$$

Primary ionization density is then one pair every 250 $\mu$m at STP and each primary pair produces approximately 3 secondaries.

The probability to have the number of primary pairs in the interval $n_p \pm \rho$ is 68.3%, and we can apply the Poisson statistic to obtain the probability of the actual number $m$ in one event,

$$P(m, n_p) = \frac{m^{n_p}}{n_p!}e^{-m} \tag{3.9}$$

where $n_p$ is the average number of the primary interactions.

## 3.3 Operational Modes

In the following, we will describe the various operation modes in gas detectors.

### *3.3.1 Proportional Operation Mode*

When a fast electromagnetically interacting particle passes through a gaseous medium, it interacts with the molecules or atoms of the gas by producing ionizations. Depending on the applied voltage and on the detector geometry, the mode of operation is different for devices as multiwire proportional chambers, (MWPC), drift chambers, limited streamer tubes, Geiger counters etc.

A charged particle which has enough energy to ionize the gas molecules or atoms will cause ionization processes and liberate free electron–ion pairs. The liberated electrons of this primary ionization process start to drift toward the positively charged anode wire. If the primary electron has an energy greater than the minimum ionization potential of the medium, secondary ionizations will occur while the primaries continue their trip to the anode and positive ions to the cathode. At the vicinity of the anode wire (according to measurements[25] and calculations at several wire radii from the surface of wire) the electric field is strong enough to start the gas multiplication and a single free electron can create an avalanche of $10^5$ or so electrons that surrounds a limited length of wire. Figure 3.2 shows the typical shape of an avalanche.

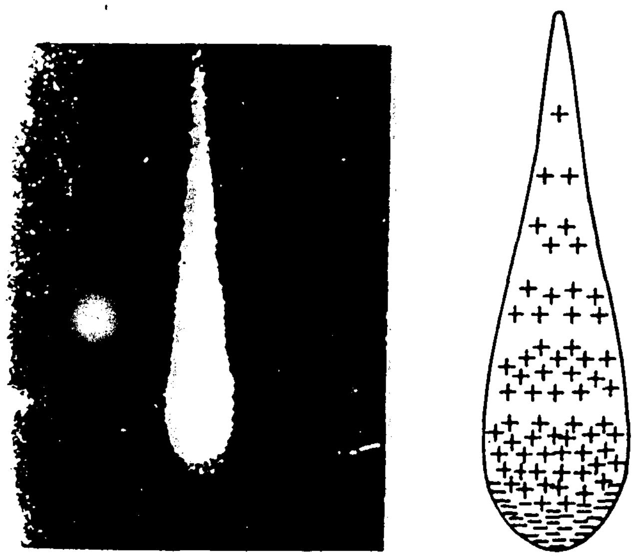

Figure 3.2. Drop–like shape an avalanche showing the positive ions left behind the fast electron front.

The avalanche is completed within a fraction of nanosecond and the electrons created during the multiplication reach to the wire. The positive ions, having a drift velocity $\approx 1000$ times lower than electrons because of their masses, will drift towards the cathode along the same field line followed previously by the free electrons. The multiplication process creates an electronic pulse detectable at the wire. The signal, having negative polarity on the wire and positive on the cathodes, is mainly produced due to the motion of the positive ions. In the case of device running in proportional mode, the amplitude of the signal is proportional to the charge created by the primary ionization. The spatial resolution and the drift time depend essentially on the gas mixture, pressure and on the applied high voltage.

### *3.3.2 Operation in Geiger Mode*

During the development of the avalanche, the atoms excited emit ultra-violet photons. When the photon energy exceeds the highest atomic energy level, these photons will ionize other atoms or molecules and the avalanche will tend to spread along the whole length of the wire and cause a discharge. This discharge is independent from the initial ionization and the wire will remain dead until when the positive ions reach the cathode. Because of the low drift time of these ions, the dead time[26] of the device in this regime is of the order of $10^{-4}$ s.

Due to this fact the spatial resolution of a Geiger counter is poor. To improve it the TPC collaboration[27] tried to interrupt the Geiger discharge by using nylon separators. They succeeded to stop the Geiger streamers, but they had some dead or inefficient regions near the nylon.

Another technique used in Geiger regime to improve the spatial resolution is to add a polyatomic gas for quenching the UV emissions produced during the avalanche process[28]. The quenching efficiency of a polyatomic gas increases with the number of atoms in the molecule, therefore, for high gain operations as Geiger or streamer, isobutane is one of the mostly used gases.

### *3.3.3 The Limited Streamer Mode*

The streamer mode, known as high gain, thick wires, and large signals mode, has been studied by Charpak *et al.*[29] in the multiwire chambers already in 1975. They operated with voltages higher than in the proportional mode and used a lower percentage of quencher than that of the generally used in "magic gas" mixture. They observed a transition from proportional regime to the so–called "limited Geiger" regime by obtaining large pulses ($\approx$ 40 mV on 50 $\Omega$) with an approximately 10 mm of spatial extension along the wire and 300 $\mu$s dead time. After the original investigation, the first systematic work on the streamer mode with plastic LSTs started at Frascati for the Adone experiment using 18 mm diameter, resistive coated plastic tubes (10$\div$100 K$\Omega$ sqr)[30] and since then followed by many other groups.

In the streamer mode, because of the high electric field, the amplification during the avalanche process is very large and the avalanche tends to spread both along and radially with respect to the wire. The presence of the quencher, stops the growth of the streamer along the wire after few mm. The direction of the streamer is then from the wire to the primary ionization point, along the same field line followed by the primary ionization electrons; therefore, space charge distribution around the wire is not symmetric for a streamer.

In the region where the streamer develops, the electric field is greatly reduced due to the presence of a large quantity of ions and thus few mm of wire remains dead for about one msec, that means, during the dead time other incoming particles cannot be observed. This fact does not reduce the detection efficiency by more than few percent if the flux of particles is below few $10^2$/s.cm$^2$. This is one important feature of the streamer mode in comparison to the Geiger mode. In this mode, the number of primary ionization electrons does not reflect on the streamer pulse size as it happens in the MWPC. The independency of the streamer discharge from the initial ionization reduces the statistical fluctuations on the avalanche size fact which is relevant to increase the energy resolution of calorimeters. The typical anode pulse charge is about 25 pC which corresponds to about $1.3\times10^8$ electrons.

In an interesting study[31] done by the M. Atac *et al.*, it has been observed that the streamer pulse shape does not vary if the load resistor is changed (from r=75 Ω to r=1 KΩ). The independency of the pulse shape from the RC of the circuit indicates that the pulse essentially depends on the motion of the positive ions drifting towards the cathode. They also photographed the streamer discharges by using (50%)Argon+(50%)Ethane mixture. They observed that the streamer discharges are filaments of a few mm lengths developing radially from the wire and spreading approximately 100÷150 $\mu$m along the wire.

The Efficiency Plateau:

Depending on the tubes geometry and on the operation parameters like the gas mixture, gate duration, dead time of electronics and threshold value, there is a voltage range where the counting rate of the tube remains constant and reach the highest counting efficiency (about 95%); the so–called "efficiency plateau". The knee of the single rate curve is a transition region between the proportional and the streamer modes of operations and "depending strongly on the threshold", the plateau starts where the transition is completed. The dependency of the efficiency plateau on the various parameters and test set–up configurations will be discussed in section 5.2. Here it is important to point out another significant difference between the streamer pulses and the proportional ones, that is, all the streamer pulses have a minimum amplitude larger than a certain value.

Rising to higher voltages or reducing the quencher composition in the gas mixture will cause the generation of afterpulses. The delay time between the after pulses and the primary pulses is constant for a given geometry[30].

The generation of after pulses is due to the UV photons emitted by the excited gas atoms or molecules created during the avalanche development. Some of these photons escape from the avalanche region and extract a secondary electron from the cathode. These photoelectrons drift from the cathode to the wire with a drift time that corresponds to the delay with respect to the initial streamer and cause afterpulses near the wire but outside the dead region formed by the primary streamers. Another reason for the creation of afterpulses is the extraction of electrons from the cathodes due to ion interactions. These afterpulses have time delays of the order of few ms with respect to the primary streamer. The after pulses represent one of the mechanisms which are responsible for the rising tail and for the width of the single rate curve (plateau).

Multiple streamers may also arise from the particles crossing the detector and making small angles with the wire. In this case, the primary electrons are created over a wire length greater than that the typical width (few mm) and can create two or more streamers, so–called "multiple streamers", almost simultaneously.

Secondary (or multiple) streamers have been studied[30] using the collimated and uncollimated $\beta$ ($Sr^{90}$) sources and cosmic rays varying the angle of the incoming particles with respect to the wire. Fig. 3.3 shows the dependence of the multiplicity and of the efficiency on the projected impact angle obtained by the CHARM II Neutrino Detector group[32] with cosmic rays.

Reference[32] also contains the results about multiple streamer generation and probability curves as a function of the track angle and HV values. Their observations also support the result that probability of multiple streamers increase with the smaller angles of the incoming particles and with the applied HV.

## 3.4 Structure of the Plastic LSTs

There are two main versions of the plastic LSTs. The first has a resistive top cover and the second is coverless. The original version (with cover) is the one used in the Mont Blanc proton decay experiment[33].

The coverless version is adopted in most recent experiments, including *SLD*. (Fig. 3.4) shows cutaway view of LST module used in *SLD* WIC.
If the resistive top cover is removed, the positive ions produced in the streamer process drift toward the insulated top side (inner face of the PVC container

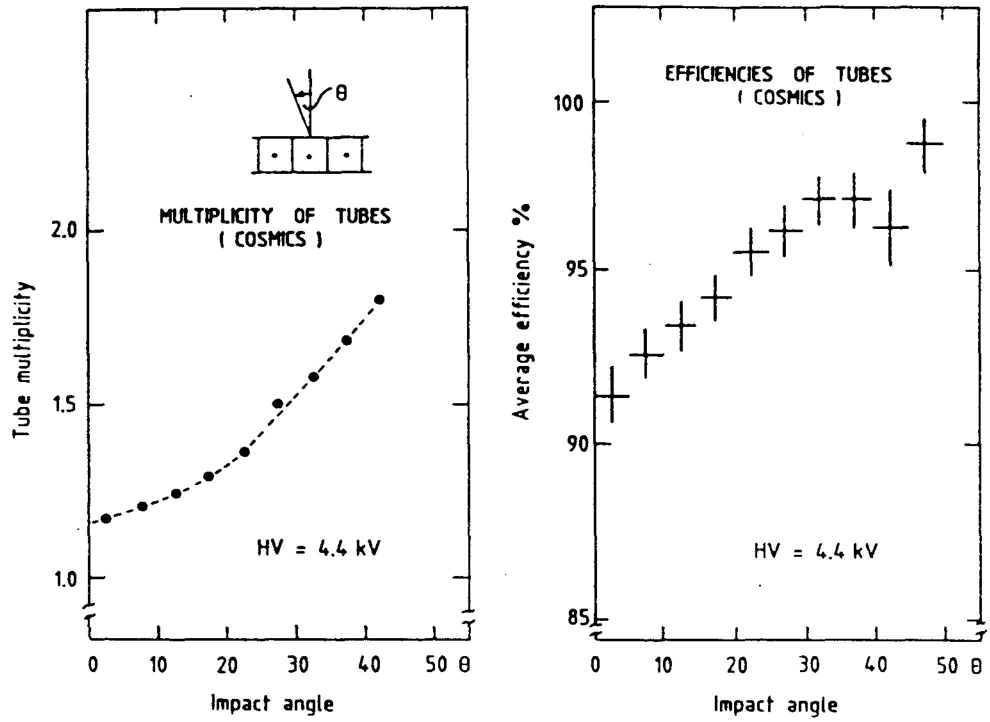


Figure 3.3. **The LST multiplicity (left) and the efficieny (right) versus the projected impact angle for cosmics.**

which is not conductive) and accumulate there. This modifies the electric field lines, as shown in Fig. 3.5, but it does not reflect as an appreciable change on the streamer charge. The charge accumulated on the inner side of the PVC sleeve can be neutralized, if necessary, by applying a low reverse voltage (i.e -1000 V) between the electrodes for few minutes.

The only operational difference between the two versions is that the efficiency plateau curve[33] starts at higher voltage ($\approx$ 150 V) in the case of the coverless tubes. The operational performance does not change neither for the external pick–up elements nor for the tube itself, but not having the top cover reduces, the time/cost of the chamber construction by about 30%.

The LST used in *SLD* are PVC extrusions coated with resistive graphite paint and cut in five different lengths (up to 8 meters). The resistivity ranges from 50 K$\Omega$ to 2 M$\Omega$ per square, which provides a uniform electric field and it

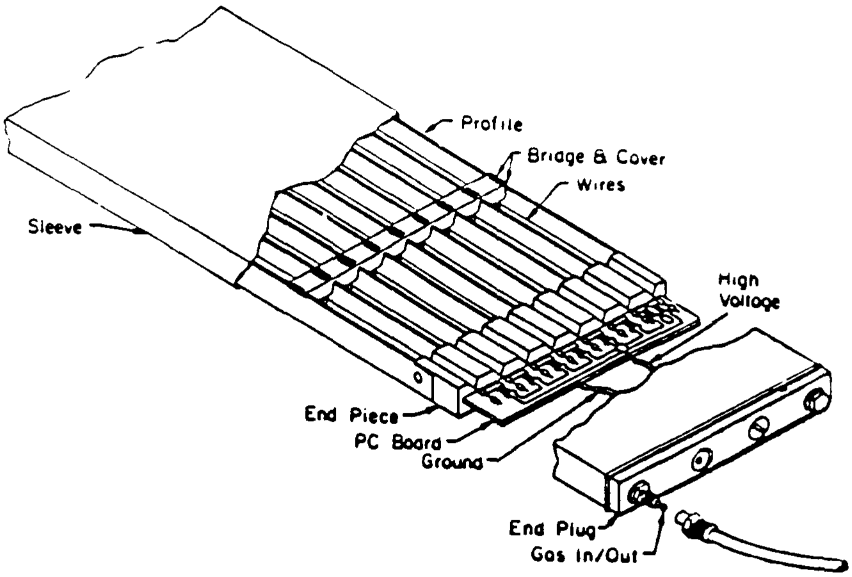


Figure 3.4. **Coverless version of a LST used in *SLD* WIC.**

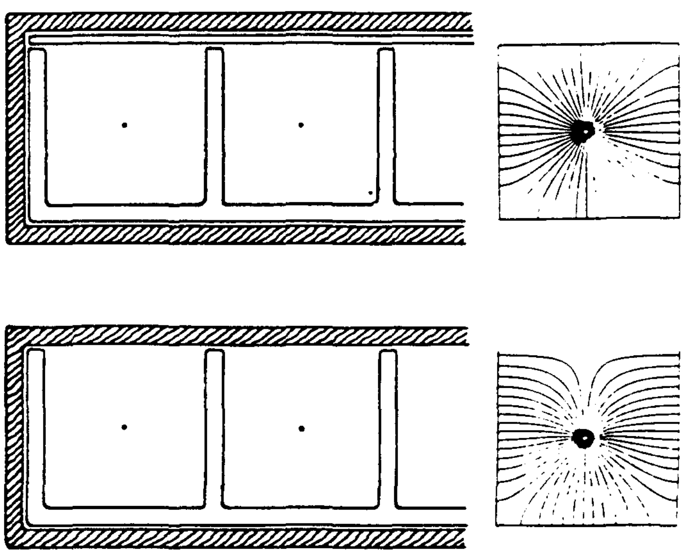

Figure 3.5. **The geometry and the electric field lines for the LST with (upper) and without (lower) top cover.**

is also transparent to the fast transients induced by the streamer on the wire. This allows the detection of the induced signals on the external cathodes (pads and strips (X,Y)). Each profile contains eight open square cells ($0.9\times0.9$ mm$^2$) separated by 1 mm thick walls. A 100 $\mu$m thick silvered Be–Cu anod wire is fixed in the center of the cells and held every 50 cm with plastic spacers and bridge covers. The electrical isolation between the individual wires are provided by eight 220 Ω series resistors connected to the HV bus. The resistor–network is placed on a (G–10) ceramic card and plugged on the HV end of the profile. The profiles are then inserted in extruded PVC containers through which the gas, HV and ground connections are provided. The endcap modules of *SLD* are inserted into the double sleeves that allows a simple replacement of the modules in the chambers in case of failure. Further information about the construction details of the modules and their electrical fundamentals will be given in Chapters 4 and 5 respectively.

### 3.5 GAS MIXTURE

One of the most important parameters for gas detectors is the gas mixture used. For an uncritical, noiseless and stable streamer operation a sufficiently quenching gas mixture is required. The correct choice of the gas mixture is related to other parameters like wire diameter, cathode material, tube dimensions etc. To understand this relation, better we will do an overview of the studies done by various groups on different compositions of gas.

At the beginning, the gas selected for the Nusex proton decay experiment was (Ar+Iso → 1+3) but recently for safety reasons it has been substituted with ($Ar+CO_2$+n-pentane → 1+2+1) which contains less hydrocarbon and practically, from the point of view of the performances, is equivalent to (Ar+Iso → 1+3).

Iarocci *et al.*[30,34] have studied the variation of the pulse shape and single rate curves by varying the quencher quantity in the gas mixture. Figure 3.6 shows the single rate curves for different argon–isobutane concentrations.

The single rate curves have been obtained with an aluminum tube with 100 μm wire diameter. Increasing the isobutane concentrations, the high voltage plateau width increases and its knee moves to the higher values. The

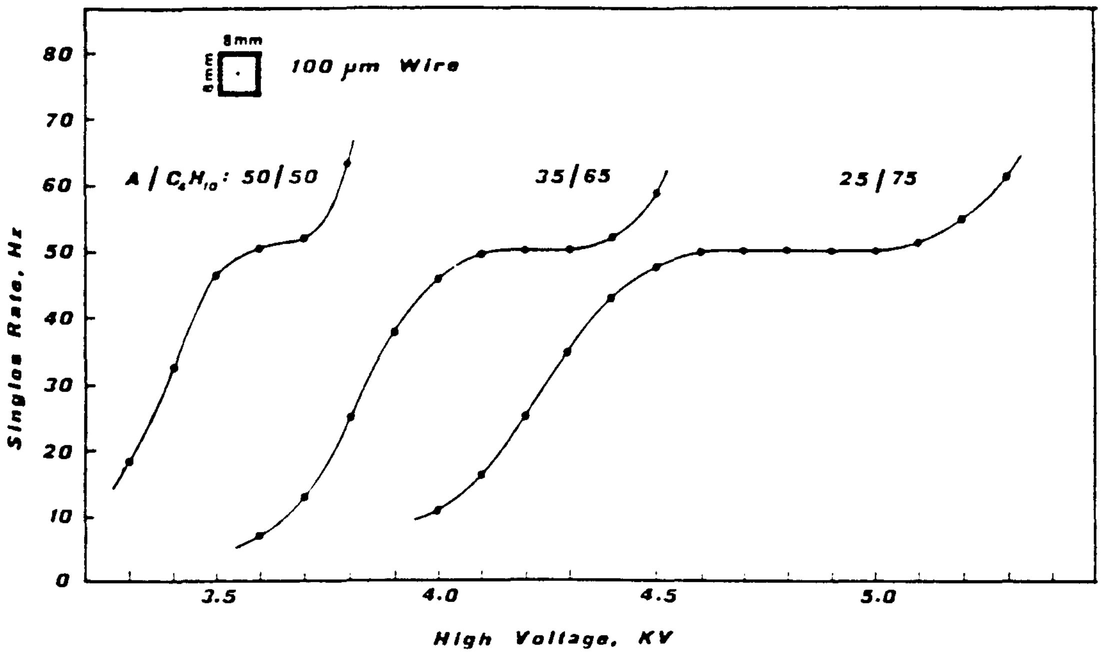


Figure 3.6. Single rate curves of an 8 × 8 $mm^2$ aluminum tube for different concentrations of the Ar+Iso gas mixture. The dead time was 0.5 $\mu$s, the threshold 30 mV/50 Ω.

measurements have shown also that smaller tube dimension requires more quencher gas. An explanation for this could be that in the streamer mode, the distance which must be considered is the one between the tip of the streamer and the cathode rather than the classic wire–cathode distance as in the case of proportional devices. In smaller tubes the distance cathode–tip of the streamer discharge cone, where the electric field is very strong, has to be smaller, that is the size of the streamer must be shorter, which implies more quenching gas.

Increasing the quencher (isobutane) concentration the peak amplitude, the rise time and the shape does not show a dramatic change. Only the width becomes smaller due to the development of the streamer over shorter distances.

For safety reasons further studies on alternative low hydrocarbon gas mixtures have been done by P. Rapp for the hadron calorimeter of the OPAL detector at LEP[35]. In Fig. 3.7 we see the charge spectra for two mixtures of $Ar/CO_2$ mixed with 42% n–pentane; in both cases the resolution is comparable to the Ar/Iso mixture. Increasing the $CO_2$ content and decreasing the voltage (300 V) the efficiency and the resolution does not change and the collected charge increases by a factor two. This was the best flammable mixture obtained by these authors having a rather low hydrocarbon content. Further measurements with various mixing of $CO_2$, ethan, ethanol gives secondary peaks, long tails and breakdowns near to the beginning of the plateau efficiency; therefore, none of these are useful for the limited streamer operation mode. As we will see in Appendixes A and B, studies performed in the framework of the *SLD*–WIC collaboration have shown that other three component non–flammable mixtures exist that are very suitable for use in the large LST systems.

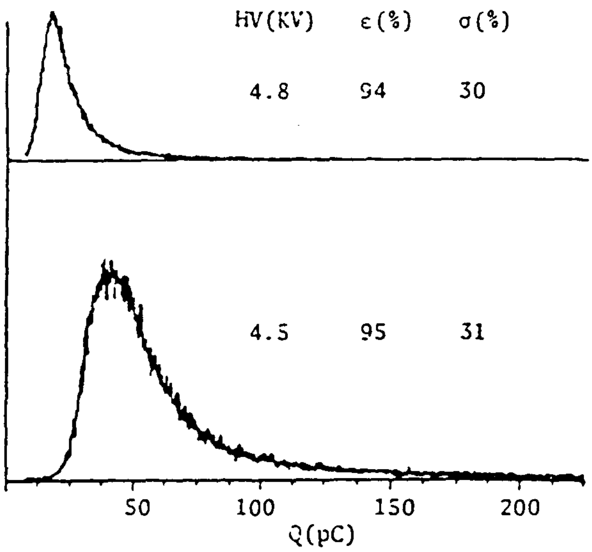


Figure 3.7. **Charge spectra for Ar+$CO_2$ passed through n-pentane (42%) (upper) Ar+$CO_2 \rightarrow$ (1+4) and, (lower) Ar+$CO_2 \rightarrow$ (4+3), with the efficiency ($\epsilon$) and the resolution ($\sigma$).**

## 3.6 Influence of the Wire Diameter

The wire diameter is an important parameter determining the operation point and the width of the efficiency plateau. By increasing the wire diameter, the intensity of the surrounding electric field decreases which means, for a larger wire diameter, higher voltages must be applied to obtain the same efficiency in this case the knee of the plateaux moves to higher HV.

The electric field at a distance $r$ from the wire surface can be written as

$$E(r) \propto \frac{1}{r}C, \qquad C = \frac{2\pi\epsilon_0}{ln(b/a)}\frac{1}{r} \tag{3.10}$$

where $a$ is the wire radius, $b$ is the distance from the wire to the cathode, $C$ is the capacitance per unit length of the system and $\epsilon_0$ is the dielectric constant (for typical gases $\epsilon_0 \approx 8.85\ pF/\mathrm{m}$). Fig. 3.8 shows how the shape of the single rate curve changes by changing the wire diameter.

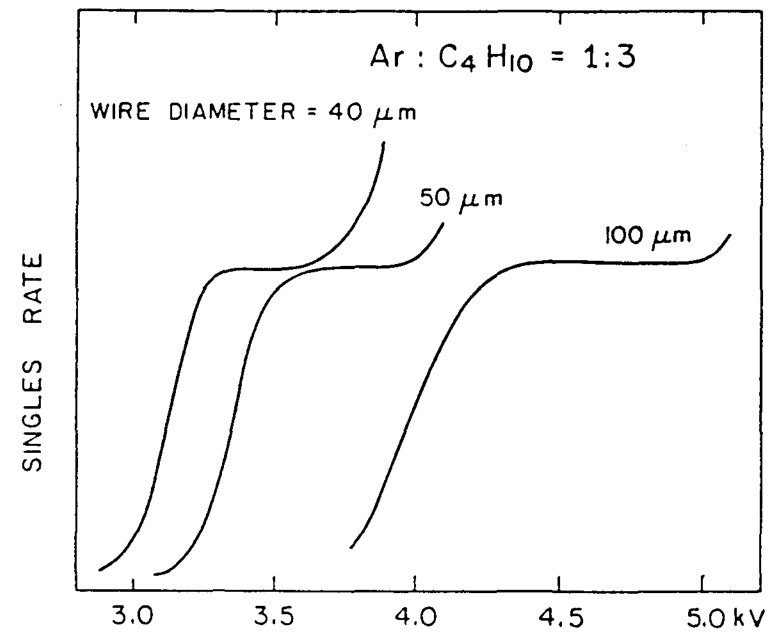


Figure 3.8. The single rate for different wire diameters of the same gas mixture.

The choice of the 100 $\mu$m diameter wire for the WIC chambers was determinated by the fact that the 100 $\mu$m wire is mechanically robust with respect to the thinner wires, and also it is possible to operate the chambers closer to the proportional/streamer transition voltage thanks to its lower relative gain in the proportional mode.

## 3.7 Cathode Material

Since the beginning of the development of the LST technology, usually two types of cathode material have been used. Aluminum as in the CHARMI Neutrino detector, and graphite coated plastic (PVC) as in NUSEX, CHARMII, *SLD* and other experiments.

In the case of the graphite coated resistive PVC extrusions, the induced pulses can be picked up from the outside (top and bottom) placed electrodes (strips, pads). Because of the cathode transparency to electrical transients, the strips, placed parallel to the wires, are well suited to measure which wire has been hit by the track while the pads are used for the energy measurements. On the other hand, in the case of U–shaped aluminum extrusions it is possible to read only the top of the side placed pick–up elements because of the shielding effect of aluminum. The wire readout is the same in both cases (Al and PVC). It is then important to understand the behavior of the cathodic material to obtain good operational performances.

Studies performed on different cathodic materials have shown that the aluminum cathode requires more quenching gas than graphite coated one. The reason for that is, the work function of electrons for aluminum is lower than for graphite and so it is easier for UV photons to extract electrons from an aluminum cathode.
Figure 3.9 shows two single rate curves for different cathode materials in the same conditions.

In the case of the transparent resistive cathode, a uniform cathodic resistivity is important to avoid some inconvenients which degrade the operational performance of the device. One can say that the operational stability depends on the coating uniformity as much as the high voltage and the gas compositions. The studies performed by various groups like Aleph and Opal at LEP[36,37] have shown that some microscopic uncoated points can cause positive ion accumulation and then a very high electric field. This could cause the extraction of cathodic electrons due to Malter effect[38]. Observations using an electron microscope to investigate the relation between the observed glow points

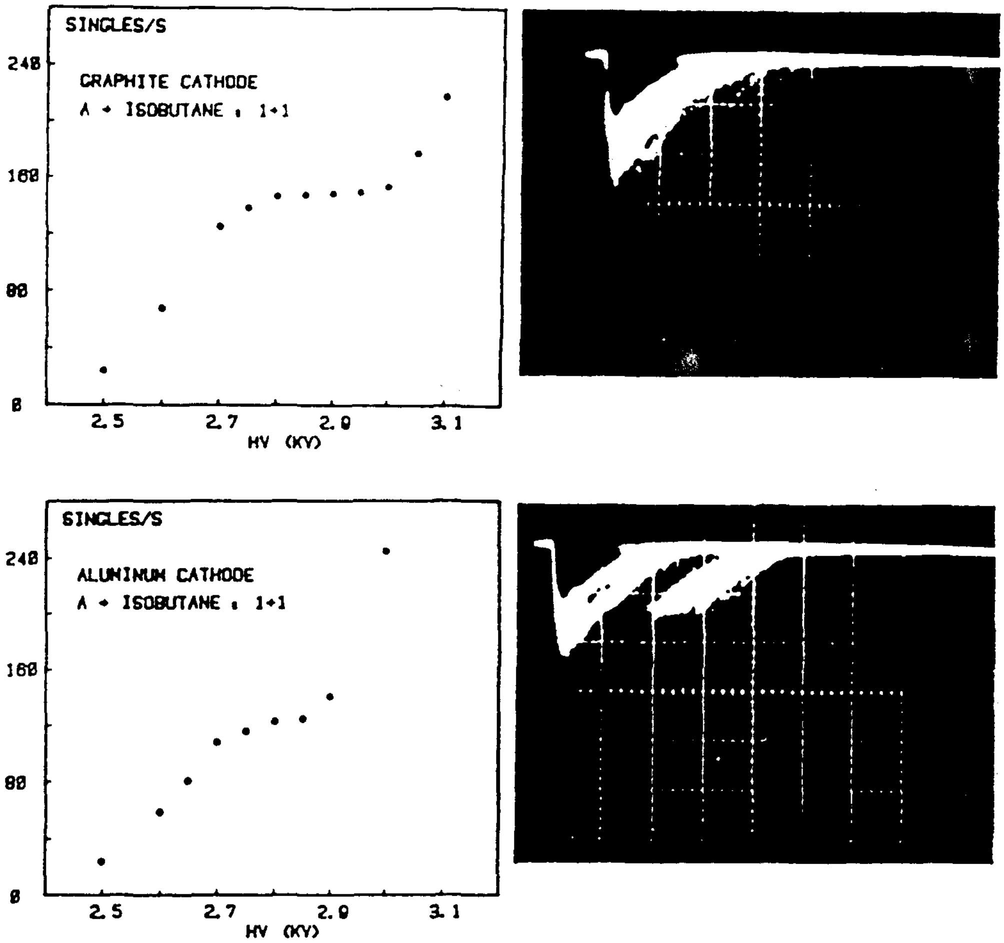


Figure 3.9. Single rate curves and wire pulses for two modules (40 $\mu$m wire) different only for the cathode material; graphite (upper) and aluminum (lower).

and these little isolated dots, suggest that most glow points correspond to the these microscopic unpainted regions[39]. Therefore, the Opal Hadron Calorimeter group[37] has tried to overcoat the graphite coating with an antistatic liquid called BREOX; they obtained a significant reduction of the instabilities without any unwanted secondary effect and a substantial improvement of the failure rate after BREOX overpainting.

### 3.8 Resistive Cathode Transparency and Pick–Up Strips

The conductive cathodes show a shielding effect, but if the cathode is resistive, the streamer discharge can induce a pulse through the resistive cathode

without being shielded and can be collected from outside cathodes connected to the readout electronics. There is a minimum value of the cathode resistivity above which the induced pulses are efficiently picked up by the strips which operate as terminated transmission lines. A full transparency to the induced pulses is essential if one wants to reconstruct the streamer position from the distribution of the charge appearing on the strips.
The cathode transparency is defined as the ratio between central and side strip peak amplitudes and normalized to the limit of the case of very high resistivity.

Let us consider the equivalent circuit[40] shown in Fig. 3.10 for the wire–resistive cathode–pickup strips–ground chain.

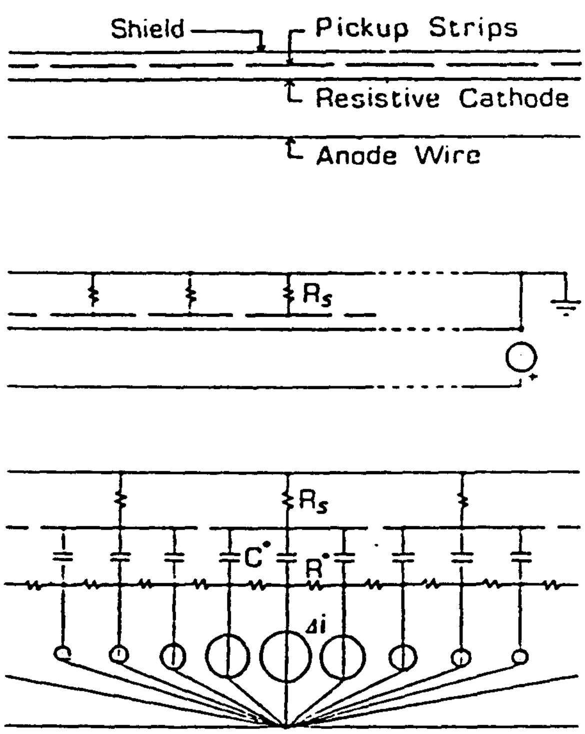


Figure 3.10. The schematic cross of a wire device with resistive cathode and external pick–up strips (upper); the electrical connections (middle); equivalent circuit with current generators to simulate the induction from an avalanche near the anode wire.

In this circuit, the cathode is connected with a $R^*$ resistance and $C^*$

coupling capacitance to the strips, and the strips are grounded via an input $R_s$ resistance. The wires are parallel to the tube cells and the strips are orthogonal to the wires. Using this equivalent circuit to simulate the strip readout, a group at Frascati[40] studied its behavior and made a comparison with the experimental data. They simulated very short current pulses with a computer program together with its development. During the short pulse time the current charges up the cathode–strip $C^*$ capacitance, through the $R_s$ resistance. On the central strips they obtained pulses with very long negative tails which correspond to the discharge of $C^*$ through the $R^*$. For the side strips, the tail following the initial pulse is positive and then goes negative. The reason for that is, any lateral $C^*$ element receives an extra charge more than the central ones through the $R^*$.

The data have demonstrated that to obtain undistorted pulses through the resistive cathode, the pulse duration must be larger than the $R^*C^*$ integration time. That means, ignoring the cathode–strip capacitance which is negligible (1.5 $pF/m^2$ for the 2 mm PVC), the only effective parameter is the cathode resistivity[40].

The same authors have compared these data with a systematic test on the cathode transparency, realized with a small chamber with replaceable graphite coated top (1 mm PVC plates) which permits the test of different resistivities.

Figure 3.11 shows the pulses on the central and the side strips with various cathode resistivity values. We see from the figure that from reducing the cathode resistivity, the peak amplitude decreases on the central strip and increases on the side strips. This is because at lower resistivities the shielding effect of the cathode lets the amplitude distribution of the pulses spread over the side strips, the so–called "broadening effect". The same transparency characteristics have been obtained by increasing the capacitance value by a factor two reducing the thickness of the PVC from 2 mm to 1 mm, or reducing the resistivity by a factor two[40].

The above discussion has been made by considering the case of the strips

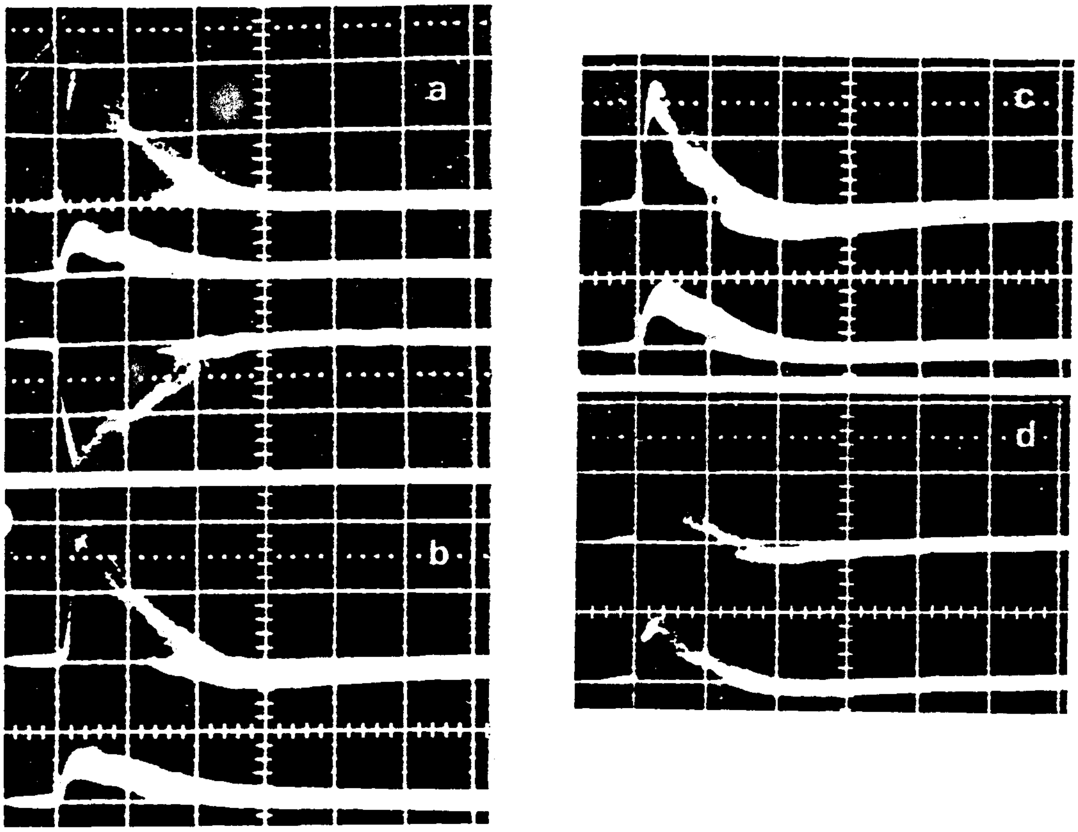


Figure 3.11. (a) Pulses on the central strip, side strip and wire, from upper to lower respectively, for a cathode resistivity R=7 MΩ/sqr. Strips and wire are terminated by 50 Ω; the scales are 10 and 50 mV/cm vertical (strips and wire respectively), 20 ns/cm horizontal. Pulses on central and side strips, for R=200 kΩ/sqr (b), 30 kΩ/sqr (c), 10 kΩ/sqr (d).

which are perpendicular to the wires. When the strips are parallel to the wires then the situation is different. In the parallel strip case one wire is facing to just one strip and there is no direct connection between one strip and different wires. This means that the strip amplitude distribution is affected less by the partial cathode shielding. There is another effect which must be taken into account; on perpendicular strips a single track produces on average many hits; while on parallel strips this effect is much more reduced, because the hits always occur along the same wire/strip.

Figure 3.12 describes the propagation of pulses on perpendicular and parallel strips. The behavior of strip lines and wires is similar to unterminated transmission lines. In the perpendicular strip case (Y–strip) the pulse travels on the wire–strip line and on the strip–ground plane line independently, that means the wire–strip load does not reflect on the Y–strip pulse shape. But in the X–strips case, the wire pulse and the strip pulse travel along the same direction, that is, the X–strip current is the image of the current on the wire. Then, the pulse shape on the X–strip depends on the load resistance of the wire–ground line. The tests performed on the transmission line behavior of the strip–tube–ground planes and the strips L, R, C characteristics will be discussed in Chapter 5.

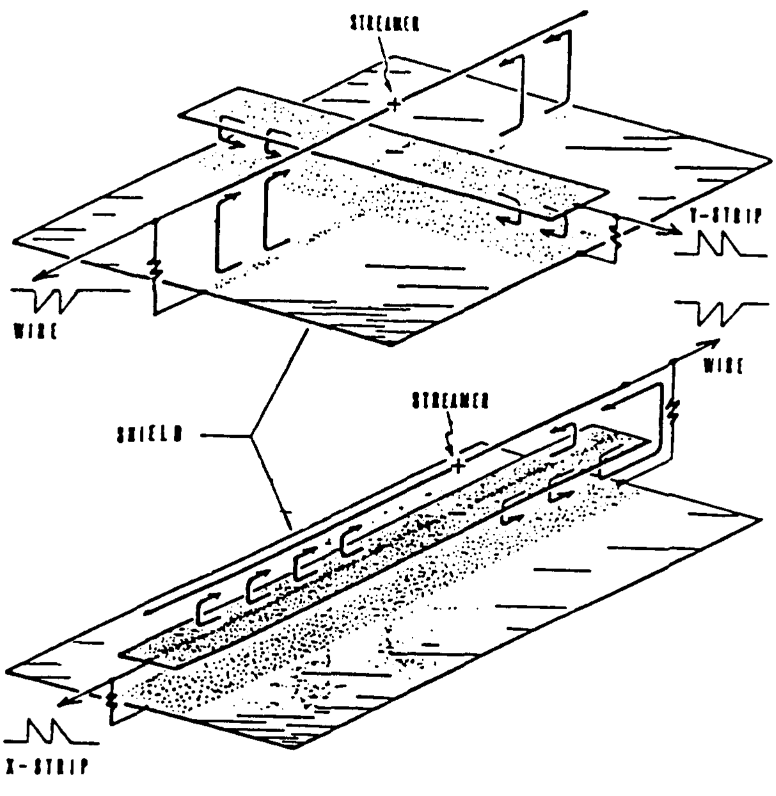

Figure 3.12. Schematic drawing the propagation of pulses on strips perpendicular (upper) and parallel (lower) to the wires.

## 4.1 Introduction

In this chapter we will describe the construction details of the LSTs and of the WIC chambers with their substructures (pads and strips).

## 4.2 Limited Streamer Tube Modules Construction

Once the PVC extruded profiles are provided by the company[41], LST construction consists of mainly two steps. First, the PVC extrusions are graphite coated in order to have the cathode transparency and, second, the graphite coated profiles are wired and inserted into the sleeves and tested for gas tightness. Approximately 10,000 LST modules were built with lengths ranging from 1.9 to 8.6 m.

### *4.2.1 Frascati Graphite Coating Factory*

#### *4.2.1.1 Coating Machine*

The coating machine used at the Frascati National Laboratory (INFN) is shown in Fig. 4.1. On one end of the machine there are mechanisms for loading the profiles on the transport line followed by a vacuum cleaning station under which the profiles pass. The profiles are then driven through the coating station situated at the center of the transport line and preceded by a brush for the final cleaning of the profile. At the other end of the transport line, a drying station blows hot air onto the profiles which are then ejected to a work bench where the resistivity of the coating layer is measured.

The coating station consists of a system controlling the flow of the coating liquid onto the profiles regulating the air flow regulating the valve of a flowmeter

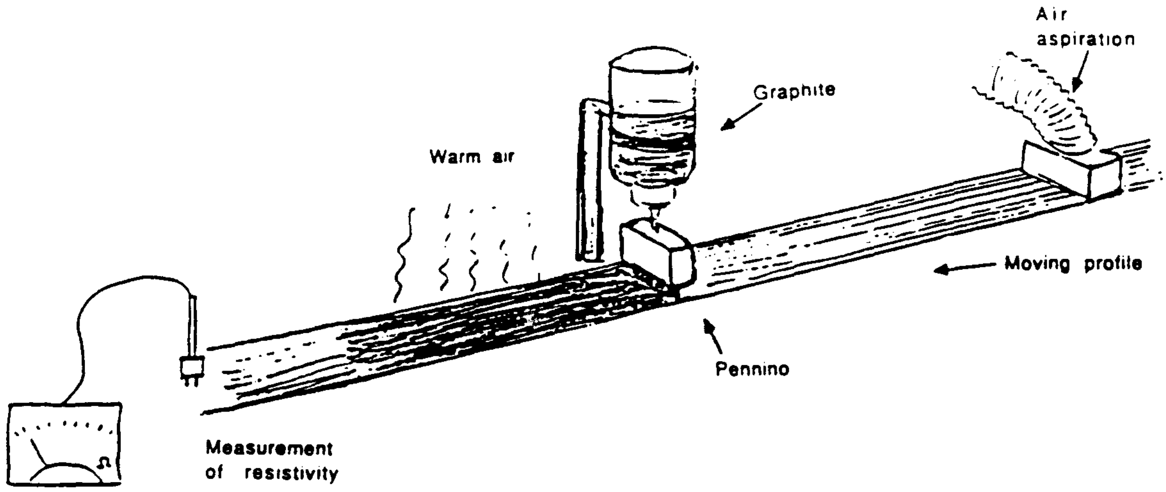


Figure 4.1. **Sketch of the Frascati coating machine.**

(approximately 0.25 cc/s into a plastic bottle containing 860 cc of liquid). The liquid drops from the bottle into a brush made of three sponges cut with a special tool so as to fit the shape of the profiles. The brush holder can be regulated in height and spreads the liquid over the whole width of the profiles. The mixture in the bottle is made by 760 cc of Metyl–Iso–Butyl–Ketone (MIBK) and 100 cc of colloidal graphite DAG–305. One bottle was enough to paint approximately 40 profiles.

On the work–bench, the coated profiles were first checked for visible coating or extrusion imperfections like pin holes or variation of the profile thickness. In the first case the profiles were discarded, in the latter case they were sent back to the factory.

#### *4.2.1.2 Monitoring of the Resistivity*

The three parameters which affect the resistivity of the coating are; 1) the flow of the liquid from the bottle (related to the air flow into the bottle), 2) the velocity of the profile under the coating station, 3) the height of the sponges over the profile. The resistivity is very sensitive even to small changes of only one parameter.

The coating resistivity was measured on–line as soon as the profiles came out of the drying station. The resistivity probe was made by two 5 mm diameter conductive sponges separated with 10 mm of distance. The resistivity of each channel was measured approximately one meter away from the last coated end of the profile.

A final resistivity window was required between 0.05 and 2.0 MΩ/sqr. Since the resistivity drops by a factor 2 to 4 in the first hour after painting, the on–line resistivity window was set to 0.2 $\leftrightarrow$ 5.0 MΩ/sqr. In Fig. 4.2 shown is the resistivity distribution of about 2000 finished profiles.

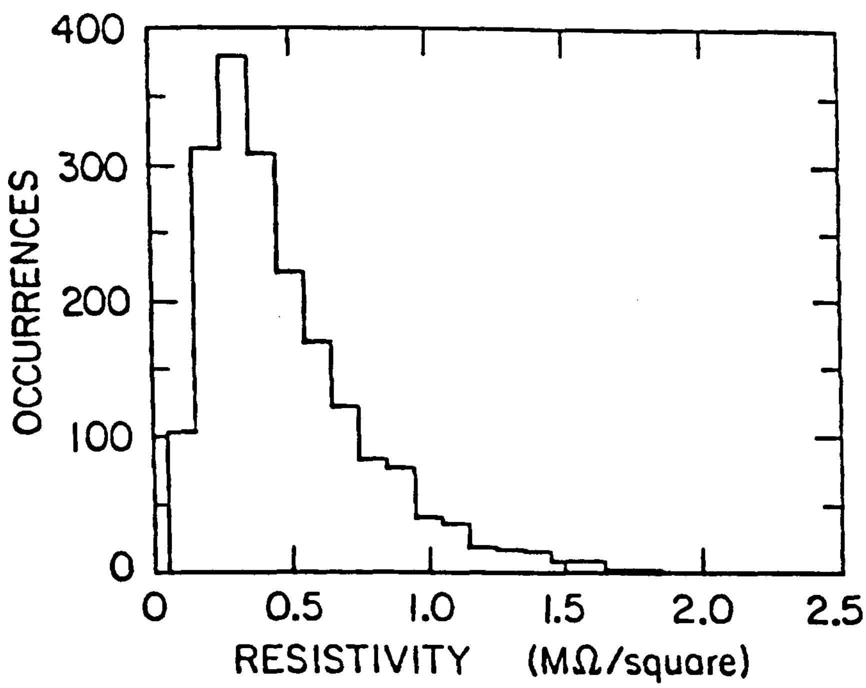


Figure 4.2. Surface resistivity distribution of about 2000 profiles.

When the measured values were showing a too low on–line resistivity, the three parameters were tuned and the profile was discarded, since an acceptable way to increase its resistivity has not been found. If the resistivity was too high or only marginally low, a parameter tuning was again carried out but the profiles were put aside and checked again later. During the second check, the profiles with a resistivity still higher than 2.2 $M\Omega/sqr$ were polished with a felt pad. This operation reduced the resistivity by a factor 2 to 5, depending on how many times the pad was rubbed against the coating layer.

#### *4.2.1.3 Remarks*

The three coating parameters are obviously correlated. This means for instance that there is no optimal value for the air flow, but it depends on the set profile velocity.

Lowering and raising the sponges could also be used to increase and decrease the resistivity of the coating layer; however, a layer too thin makes the resistivity to vary widely from point to point and from channel to channel. A good coating shows variations of resistivity between different points of the same channel smaller than a factor 1.3.

It has been noticed that the profiles can show inhomogeneous coating at the extremities. With regard to the last coated end, it is because it stays under the drying station less time than the first end, and it is not completely dry when the profile is ejected. Instead, the first end can be inhomogeneously coated because the profile edge moves the sponges passing under them.

Among the accepted and recovered profiles, every $13^{th}$ profile was put aside as a check sample and about 5% of the extrusions produced during each coating period have been wired, assembled and tested with the usual testing procedures as a further quality control check. At this stage the overall rejection rate including the manufacturing defects was about 25%.

### *4.2.2 Wiring*

At the beginning of this stage profiles and the sleeves were cut to given lengths and then the top of the walls were recoated with a felt pad in order to reduce the possibility of having high electric field caused by coating discontinuities in the original coating. In addition, the HV input end of the profile was painted with a brush in order to provide a conductive path to a piece of copper tape on which the ground connection was made.

Two end pieces with ceramic printed boards (one of which having a network of 220 $\Omega$ resistors one for each wire) were attached to the extremities of the profiles; along the extrusion, the bridges were placed every about 35 cm. At the next stage, all eight wires were strung in one pass each having a nominal tension of 250 g provided by a constant drag mechanism and then they were soldered to the ceramic boards at both ends. After checking the tensions, wires are fixed into the bridges with plastic bridge covers; the wired profile was then inserted into a extrusion sleeve of 1 mm thick and 1 cm $\times$ 8.15 cm of cross section. Vacuum cleaning of the extrusion and automatic control of the wire positions were provided during the insertion. The ground wire was soldered to the above mentioned copper tape and HV connection was provided by the soldering on the ceramic board at the same end of the ground connection. Both wires, HV and ground, were then soldered to the appropriate electrical connections on the HV endplug and both endplugs were sealed into the sleeve with a PVC solvent cement.

## 4.3 Fabrication of the Pads and Strips

The WIC chambers' external electrodes (pads & strips) were built in three facilities; at Perugia and Ferrara (Italy) and Fermilab (USA). Raw strip sheets were made of two 40 $\mu$m thick copper foil sandwiching 1.6 mm thick fiberglass.

For the strip production a raw strip passed through the following steps;

1) after mounting on a computer controlled routing and milling machine station of 9 $\times$ 2 m$^2$ surface, longitudinal strips were routed such a way that to correspond the each LST channel to a path on the strip of 9 mm width. The separation between the channels was 1 mm. At the edges of each group of eight channels an additional space was left in order to detach the channels of a LST from the

adjacent ones. For the connection to the readout electronics, each group of eight channels was terminated to form a standard PC board (2.54 mm step) connector. The strip was then cut to a given dimension using the same machine,
2) the connectors were then gold–plated on both faces (routed and ground) in order to provide good contact with the mass–termination connector terminating a flat multiconductor cable,
3) at the end, all cut and routed strips were quality controlled, cleaned and labeled.
Transverse strips (Y–strips) were cut with a 2 cm pitch for the endcap and 4 cm for the barrel. Because of geometrical constraints, the flat cable wires were soldered directly to the copper foil for the endcap longitudinal strips and for all the transverse strips.

The raw pad sheets were 0.8 mm thick fiberglass with a 40 $\mu$m thick copper foil attached on one side and the pad patterns were created using the same machinery described above.
For both barrel and endcap chambers a single sheet was used to cover one half length of a chamber. The readout for the barrel pads was provided by soldering the wires of the multiconductor flat cable which was then daisy chained using a standard mass–termination connector. In the case of the endcap pads, which geometrically are more complex, the readout was provided by making use of additional jumpers. In the barrel chambers, a 0.85 mm thick PVC–Al–PVC insulating sheet was used as ground plane and insulation; a 40 $\mu$m thick copper laminated, 0.5 mm thick fiberglass sheets were used for the same purpose in the endcap chambers.

In Fig. 4.3 shown are wiring of a typical row of pads of barrel and endcap chambers.

## 4.4 Chamber Construction

A "chamber" is a completed detector element containing several (from 3 to

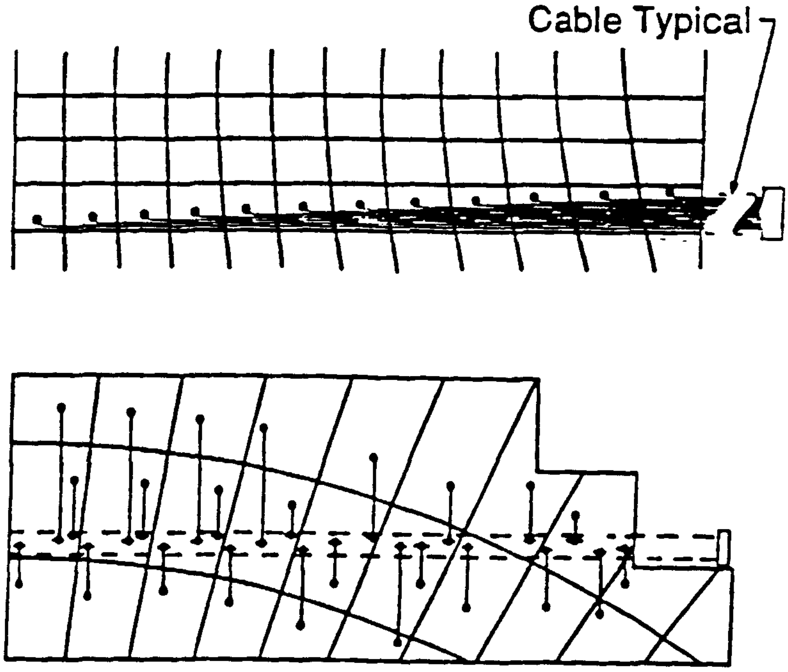


Figure 4.3. Barrel (upper) and endcap (lower) typical pad patterns and wire connections.

22) LST modules sandwiched between the electrodes (X & Y strips, pads).

The first step of the barrel chamber assembly procedure[42] was to clean the surface of the strips sheet on the lamination table. Then pressure sensitive adhesive was applied over the cleaned surface of the strip. The LST modules were then cleaned and placed on the adhesive and aligned with the strip channels; 0.75 mm thick paper strips were inserted between the modules to obtain a better glueing. At this stage of the procedure, another adhesive layer was applied on the exposed surface of the modules, and the matching pad sheets were prepared a part; on the wired surface of the pads the filling material was first attached between the wires in order to eliminate the possible bounces caused by the cables and finally it was glued to the insulated ground sheet. To complete the chamber, this part was then laminated to the exposed face of the modules. The chamber was then covered with a flexible membrane which was evacuated for about 330 min in order to assure good glue bonding and the flatness of the chamber. Pad and strip ground planes were connected with short jumpers, and the modules within the chamber were connected in series with short plastic tubes to provide the gas flow.

The assembly of the endcap chambers was performed in a similar way with the main difference that in these chambers the empty plastic extrusion sleeves were installed instead of LST modules. The LSTs were then inserted into the double sleeves and interconnected for gas flow. Double sleeve system gives the possibility to replace failed modules easily creating only a slightly more dead area in the chamber.

# Chapter 5. Studies of LST Properties & Related Substructures

## 5.1 Introduction

The tests performed with the LSTs of the *SLD* Warm Iron Calorimeter can be divided in two groups. The first group includes the test and measurements made on a small number of prototype tubes in order to ascertain the characteristics of the LSTs. The second group includes the tests on large number of tubes, in order to establish the quality of the final product and to search for rare phenomena and effects that occur only on very large number of tubes $\star$ workingtime. In this chapter we will discuss the first group of tests.

## 5.2 Operating Point and Characteristics

In this section we will give the summary of detailed studies performed on the main operational characteristics of LSTs.

### *5.2.1 Electrical Fundamentals and L, R, C Characteristics of LSTs*

#### *5.2.1.1 HV Circuit and Electrical Fundamentals of LSTs*

Fig. 5.1 shows the HV circuit designed for *SLD* LSTs. The components shown inside the dotted line are placed on the "HV board" while all other components are mounted on the LST itself. The electrical separation of wires is provided by the 220 $\Omega$ resistor placed on the ceramic printed board located at the HV end inside the sleeve. The design[43] of the HV circuit derives from the requirement of a good muon tracking and hadron calorimetry. The most important is that, the signals on strips other than the "hit" one (cross talk) should be minimized without affecting the operating point of the detector. It follows that the values of the compensating capacitor and the terminating

resistor $R_T$ must be selected appropriately. Fig. 5.2 shows how the strip–to–strip cross talk varies for different values of the resistor $R_T$.
The same attention should be paid also for the choice of the capacitor value; it should be larger than the tube capacity and small enough to avoid a voltage drop of the signal. In our case, we have chosen the components in such a way to provide a good two track separation while minimizing the reflections. The 20 MΩ resistor isolates the HV power supply from the LST and reduces the electrical cross talk.

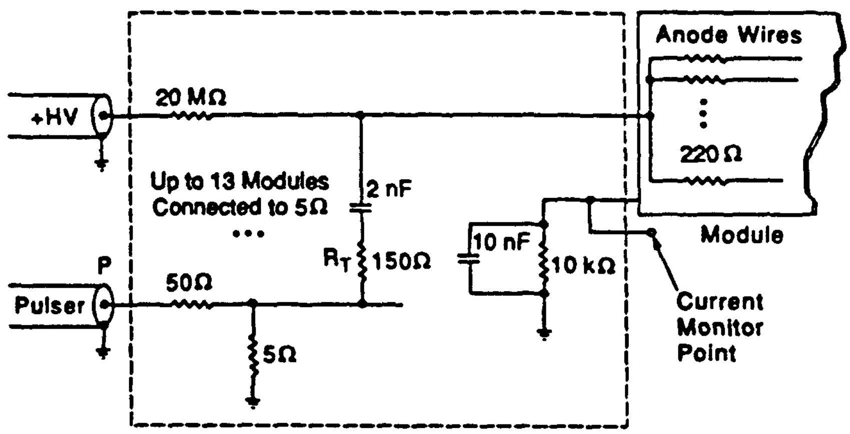


Figure 5.1. HV circuit for the LST of *SLD*. $R_T$ reduces the strip–to–strip cross talk. In order to test the readout electronics the individual LST can be pulsed at the point "P".

Another important feature of the HV board is that it is possible to pulse the wires in order to check the strip and pad readout. The average current drawn by the single LST is also monitored at the point indicated in the Figure 5.2.

### 5.2.1.2 *L, R, C Characteristics of LSTs*

In the following we study the transmission line behavior of the LSTs.
Let us assume that the current is injected at one point of the line and forget about the reflections for the moment. The input current is divided into two

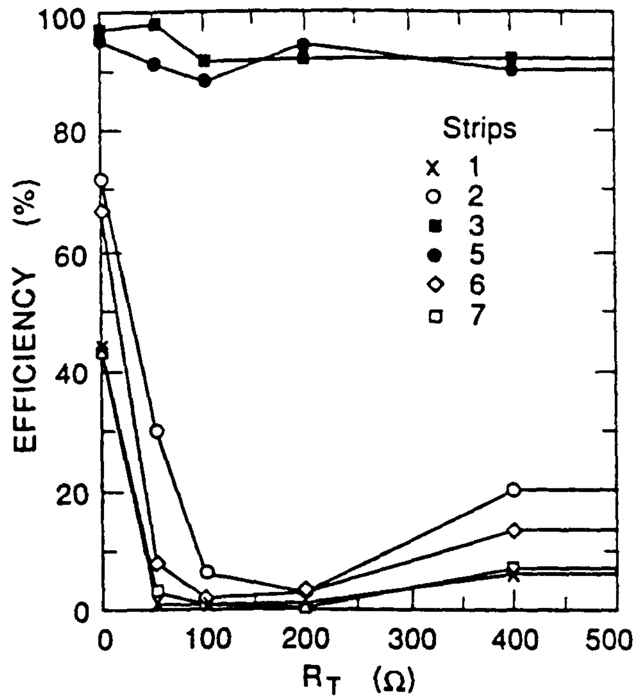


Figure 5.2. **Efficiency versus terminating resistance for 1 mV discriminator threshold (strip 4 is selected to be the central strip). Strip–to–strip cross talk is minimum for $R_T$=150 Ω which is the value that needed to terminate the wire–strip transmission line.**

halfes flowing in two opposite directions along the wire. The propagation of the signal is described by the modified telegraphers equations[44];

$$\begin{aligned} \frac{\delta v}{\delta x} + L\frac{\delta i}{\delta t} + Zi = 0 \\ \frac{\delta i}{\delta x} + C\frac{\delta v}{\delta t} - J = 0 \end{aligned} \tag{5.1}$$

where $v = v(x,t)$, $i = i(x,t)$, and, L, C, Z are the inductance, capacitance and resistance per unit length of line which can all be functions of x (in our case they are 1 $\mu$H/m, $\approx$ 12 pF/m and Z $= \sqrt{L/C} \approx 290\ \Omega$ respectively). $J(x,t)$ is the space–time distribution of the injected current density and the transconductance (leakage across the line) is assumed zero.

If the line is short compared with the risetime of the pulse, the line can be considered as a capacitor. For a long line, the signal reflects back and forth and at the end is approximately twice what it would be if the line was terminated.

The following equation gives the general expression for the time distribution of the signal at the end of a line with reflection coefficient F at each end.

$$
\begin{aligned}
V(x_0,t) = i_0 Z_0 \frac{(1+F)}{2} [ & \\
& \sum_{m=1}^{m_1} F^{2m-2} exp\{-(t + \frac{x_0}{V} - (2m-1)\frac{L}{V})/t_d\} \\
+ & \sum_{m=1}^{m_2} F^{2m-1} exp\{-(t - \frac{x_0}{V} - (2m-1)\frac{L}{V})/t_d\}]
\end{aligned}
\tag{5.2}
$$

where;

$$
\begin{aligned}
m_1 &= INT\{(x_0 + vt + L)/2L\}, \\
m_2 &= INT\{(vt - x_0 + L)/2L\}, \\
x_0 &= \text{position of the source along the line}, \\
V &= \text{propagation speed along the line}, \\
L &= \text{length of the line}, \\
t_d &= \text{mean decay time of current signal}, \\
Z_0 &= \text{line impedance.}
\end{aligned}
$$

It is easy to show that the mean voltage along a line is equal to the total charge which has flowed into the line divided by the total capacity.

## 5.3 X & Y Strips and Pads as External Readout

In section 3.8 we discussed the basic mechanisms for pulse induction and propagation along parallel and perpendicular strips. Here we will describe the various studies performed on X and Y strips and pads readout. In the following we should keep in mind that because of the space occupied by the walls of the LST, the efficiency for normal incidence is about 92%. The charge collected by the external electrodes is proportional to the total charge of the streamer on the anode wire and the polarity of the pulses on the external electrodes is positive.

### *5.3.1 X–Strips*

The X–strips of the WIC chambers, are located parallel to the wires and one strip covers one wire (there are some special chambers for the endcaps in which one strip covers two wires). They are facing the graphite coated bottom side of the PVC extrusions. Wire–strip and strip–ground lines act as two independent transmission lines. The first one has quite high impedance ($Z_1 \approx 400\ \Omega$) which corresponds roughly to an attenuation length of the order of 20 m and the second one has a lower impedance ($Z_2 \approx 33\ \Omega$). The strip readout electronics is matched to the latter and is connected to the strip transmission line through a short flat cable ($Z \approx 80\ \Omega$).

Because of its high impedance, the graphite coated cathode of the LST, located between the strip and the wire, does not affect significantly the pulse on the wire–strip line. Since the wire–strip distance is constant, the magnitude of the induced pulse on the strip is independent from the position of the incident particles. Fig. 5.3 shows the configuration of the transmission line of the X–strips.

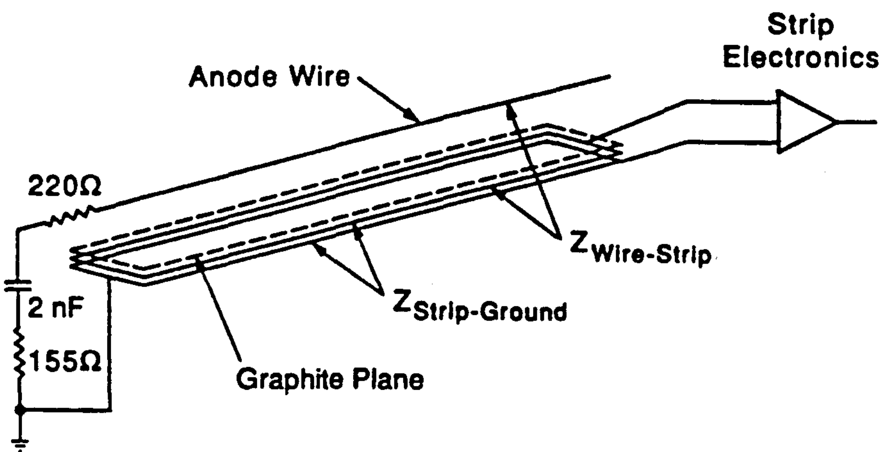


Figure 5.3. **Equivalent circuit for the X–strip readout showing the equivalent transmission lines.**

When the streamer occurs near to HV end of the wire, due to the reflection from the open end, the pulse induced on the strip is double–peaked and two times smaller than on the anode wire (see Fig. 5.4 and Fig. 5.5). This fact is very important when discussing the spatial uniformity of the strip readout, in particular if the discriminator used for the readout is voltage–sensitive. On the other hand, the efficiency of the X–strips does not depend on the position along the strip if a charge–sensitive discriminator is used. Fig. 5.6 shows the strip efficiency as a function of HV at two positions along the LST and using a voltage sensitive–discriminator.

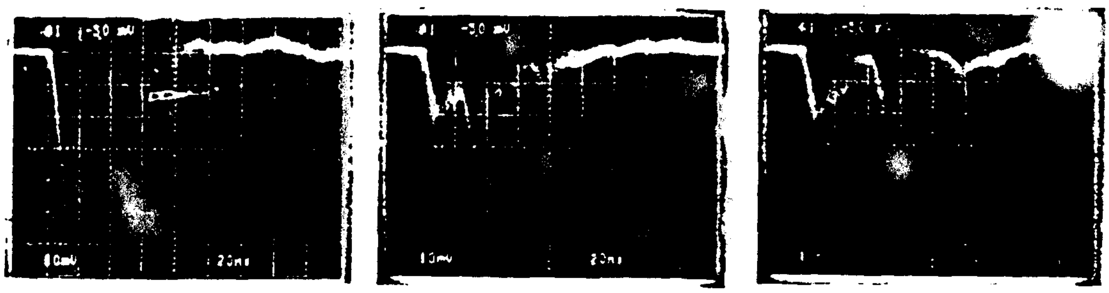

Figure 5.4. **The typical anode wire pulses into 50 $\Omega$, far from (left), midway (middle) and close (right) to HV end of a 6 m LST. The LST was operated with the "standard mixture" at 4.8 kV.**

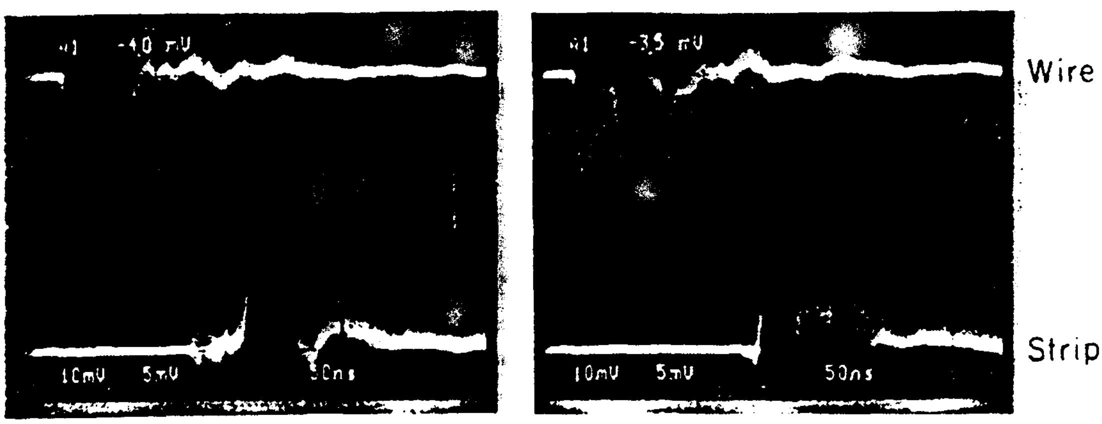


Figure 5.5. **Corresponding strip pulses to the pulse from the wire, far from (left) and close to (right) HV end of a LST chamber.**

Good muon tracking requires the lowest possible strip–to–strip cross talk which can be reduced by tuning the terminating resistor $R_T$ in HV board, as we discussed above. Furthermore, the cross talk between the strips can be

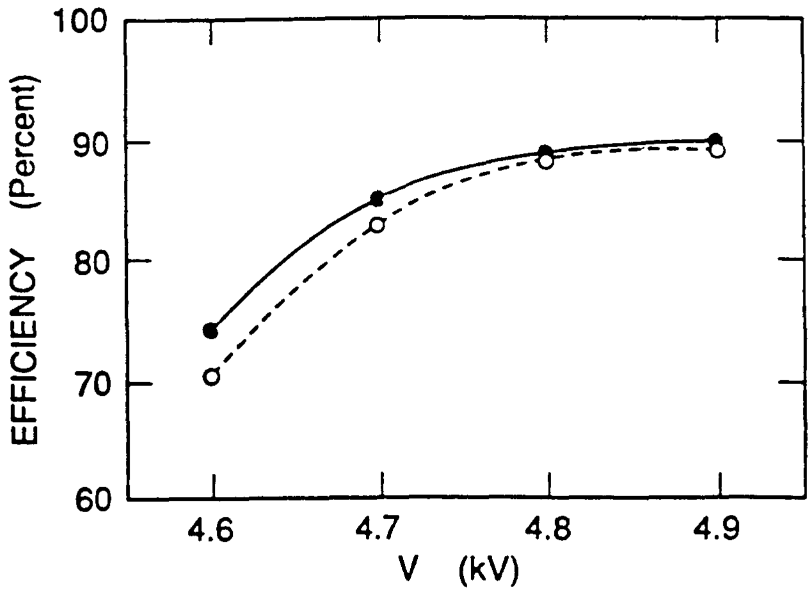


Figure 5.6. Strip efficiency versus HV at the positions; near the HV input (open circle), and far from the HV input (closed circle). The discriminator threshold was setted to 3 mV.

diminished by raising the discriminator level of the strip electronics until the strip efficiency is not decreased.

Fig. 5.7 and Fig. 5.8 show the strip efficiency as a function of cell number for different $R_T$ values and distances from the HV end for different discriminator levels. The measurements[45] were made on a 6 m long tube using the cosmic rays and for the trigger three 1.5 m tubes are used. Two of these cosmic trigger tubes were made with only one wire and the third one was constructed with the wire missing in "logical complement" to serve as a veto. All three LSTs were operated at 4.65 kV with the "standard mixture". In Fig. 5.7 shown is that the lower threshold is required for the tracks penetrating the chamber near the HV input than for tracks close the strip readout (opposite end), while Fig. 5.8 shows that the decrease in efficiency when increasing the discriminator level is more rapid in the center of the tube than at the edge.

For the final setup of the WIC chambers, the front–end electronics of the

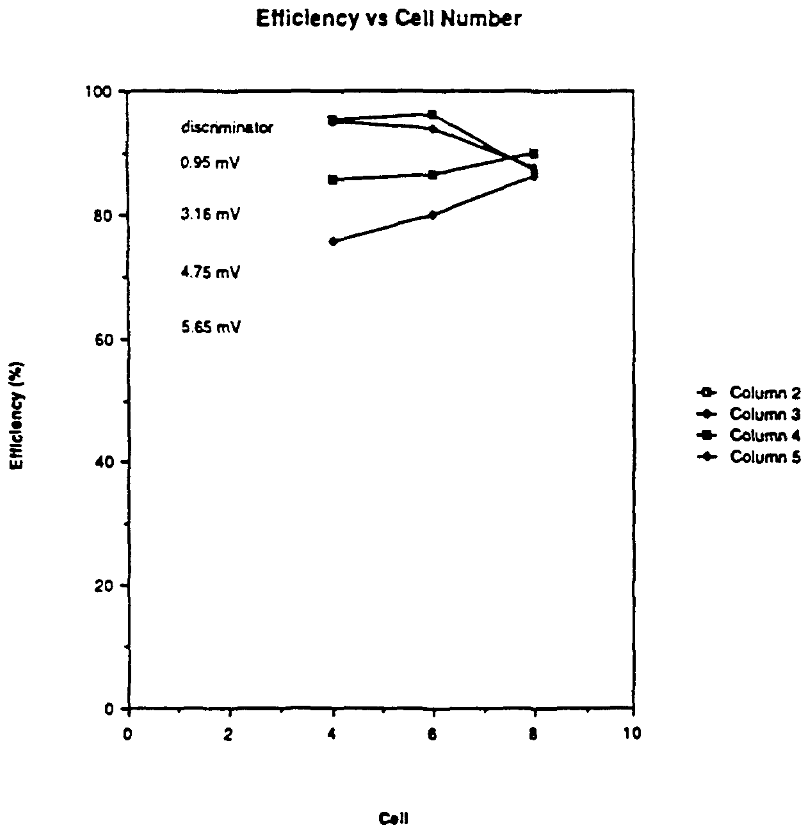


Figure 5.7. The strip efficiency as a function of the cell number for various $R_T$ values. The discriminator threshold was 1 mV.

strips has been modified by adding two–stage 50 times gain preamplifier, in order to maintain the possibility of operating the detectors also in proportional regime. Fig. 5.9 and Fig. 5.10 show the strip efficiency curves versus the threshold voltages. In both figures threshold values were set on the front–end electronics[46] (SGS) board after the 50 times preamplification.

Fig. 5.11 shows the average plane efficiency and the average cluster size as a function of the discriminator threshold for muon tracks measured with the barrel chambers of *SLD*. The cluster size is defined as the number of contiguous hit strips in a given chamber layer along the muon track. As we can see from the figure, a threshold of 3 mV corresponds to an average cluster size of three strips with an efficiency of 90%.

Several tests have been performed to determine the dependence of the

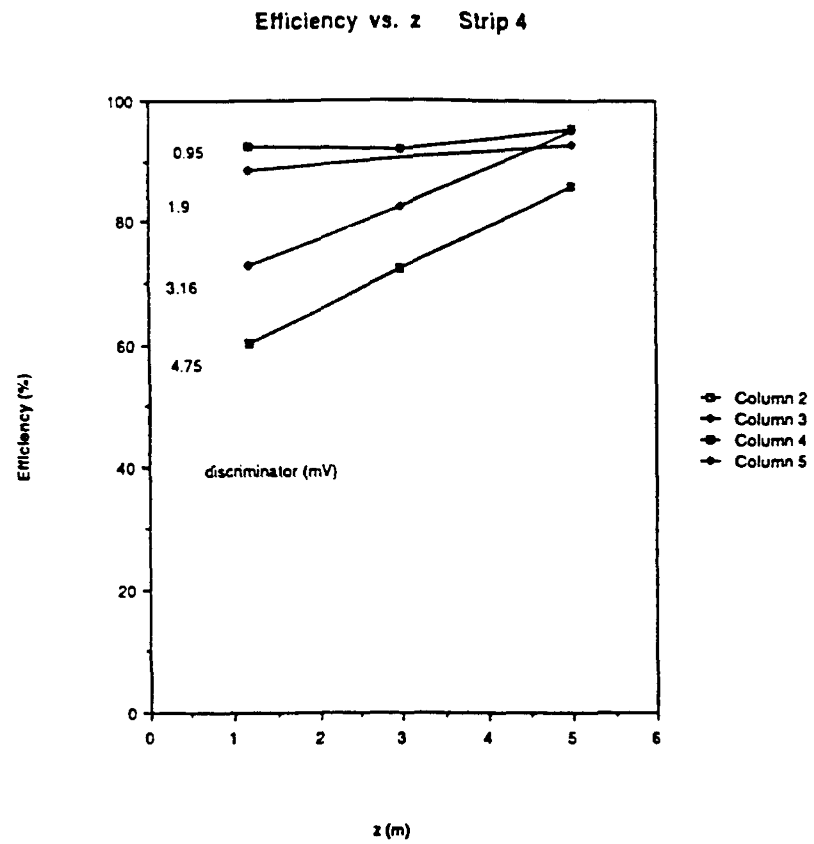


Figure 5.8. The efficiency of the central strip for various discriminator levels as a function of the distance from the HV end.

efficiency on the incidence angle. The results will be discussed in section 6.7.2 together with the results of other cosmic rays tests on the finished WIC chambers.

### 5.3.2 *Y–Strips*

The Y–strips are mounted on the top side of the extrusions, perpendicular to the wires. Their transmission line behavior is different from that of X–strips. The width of the Y–strips is 4 cm for the barrel chambers and 2 cm for the endcap ones. The pulse amplitude and shape is similar as for the pulses observed on the X–strips and the same readout electronics (SGS) is used.

When the streamer pulse propagates along the wire, it couples to adjacent Y–strips. For that reason, various questions had to be answered when designing

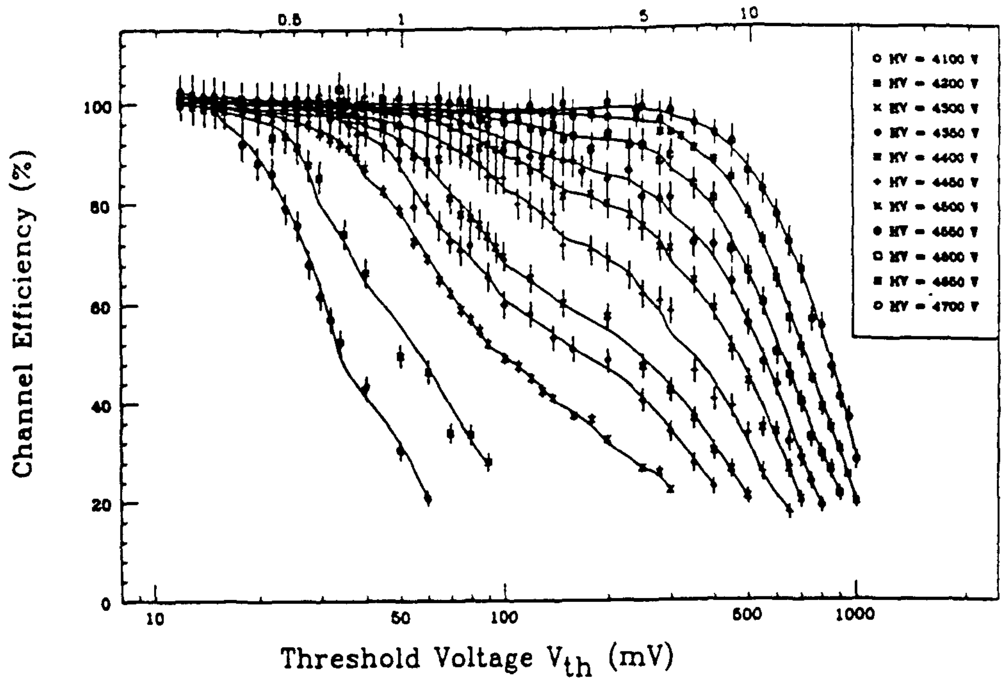


Figure 5.9. **Channel efficiency versus various values of the threshold voltages.**

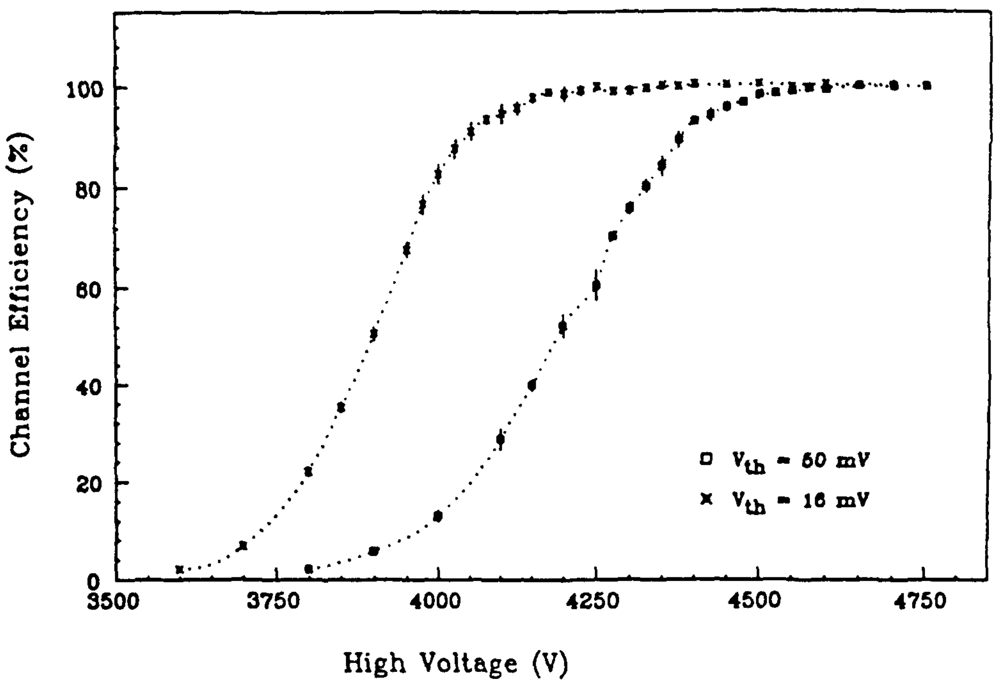


Figure 5.10. **Efficiency curves as a function of HV for two different threshold values.**

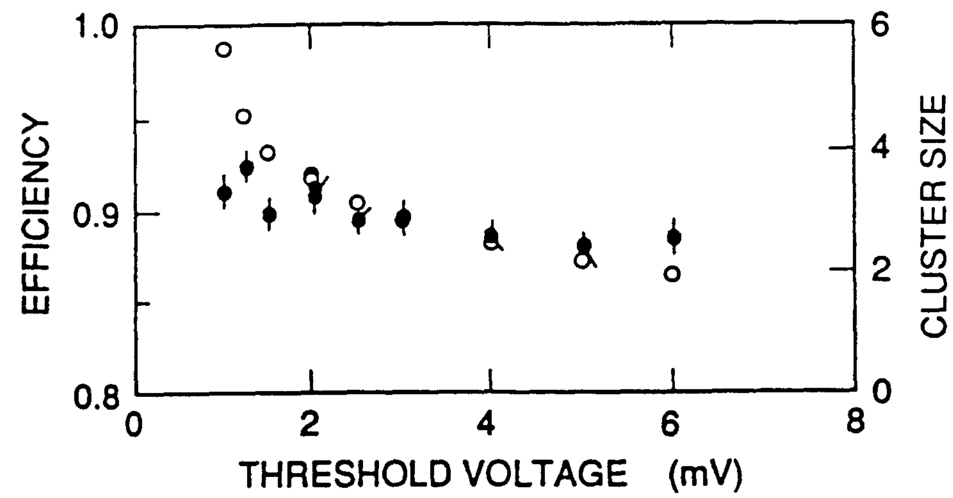


Figure 5.11. The average X–strip efficiency (closed circles) and cluster size (open circles) for cosmic rays versus the SGS–discriminator threshold. The data were taken with the WIC chambers installed in the barrel region of the *SLD* operated at 4.75 kV with the "new mixture".

the Y–strip chambers of the WIC, for example:

- Should the Y–strips face the bottom (graphite coated) or top (open) side of LST?
- Which is the efficiency and cluster multiplicity as a function of the discriminator threshold?

We have studied[47,48] in detail the above questions and our conclusion was that, in the case of the bottom placed Y–strips it is difficult to have at the same time the low multiplicity and high efficiency, while, this would be quite possible for an appropriately chosen discriminator threshold for the Y–strips placed on the top side. Fig. 5.12 clearly shows the difference between the two Y–strips mounting configurations. The very narrow shape of the X–strip distribution with respect to the Y–strips confirms that the perpendicular strips have greater multiplicity than the parallel strips. Fig. 5.13 shows that for top mounted Y–strip configuration one can obtain high efficiency ($\approx$ 90%) and the same time low multiplicity (small cluster size $\approx$ 2 Y–strips FWHM) at the same time, while for bottom placed Y–strips configuration, in order to reduce the average multiplicity one should also lower the layer efficiency.

### 5.3.3 *Pads*

The pads are segmented pick–up electrodes placed over the open top side of LSTs. They do not behave as transmission lines as in the case of the strips, but more like as capacitors. The calorimetric measurements of the WIC chambers will be done through the measurements of the deposited energy on the pads. The typical "tower structured" average pad pattern sizes are 20 cm $\times$ 20 cm with a capacitance to ground of $\approx$ 2 nF. These pads can cover several LSTs in a chamber and there are several pads along a single LST.

A pad can be treated as a capacitor in an A.C. circuit[49] in which the induced currents are attenuated with a time constant smaller than the pulse rise–time. Measurements performed[50] with LST chambers operated with the "standard mixture" at 4.65 kV show that, both with cosmic rays and $Ru^{106}$ source pads pulse size is about half of the wire pulse size.

The readout of the WIC chambers' pads is analogic and consists of a charge–sensitive amplifier connected to an LSI sample–and–hold device[51]. The integration time is 5 $\mu$s and the integrated charge depends on the integration time. It is important to note that, the current integrator will always measure the same signal induced by the streamer into the pad independently from the pad size. However, the noise increases with the capacity and the voltage signal is inversely proportional to the pad area.

The studies made on the pad cross talk have shown that the cross talk does not significantly affect the total energy resolution, while for X and Y strips low cross talk is essential in order to obtain good tracking resolution. The measurements have been made by using cosmic rays, and a $Sr^{90}$ source was placed over a pad. Fig. 5.14 shows the pulses on the center pad and on the adjacent pads along the same LST chamber. As is shown in Fig. 5.15, the cross talk between adjacent pads along the same LST is about 10% and it is essentially

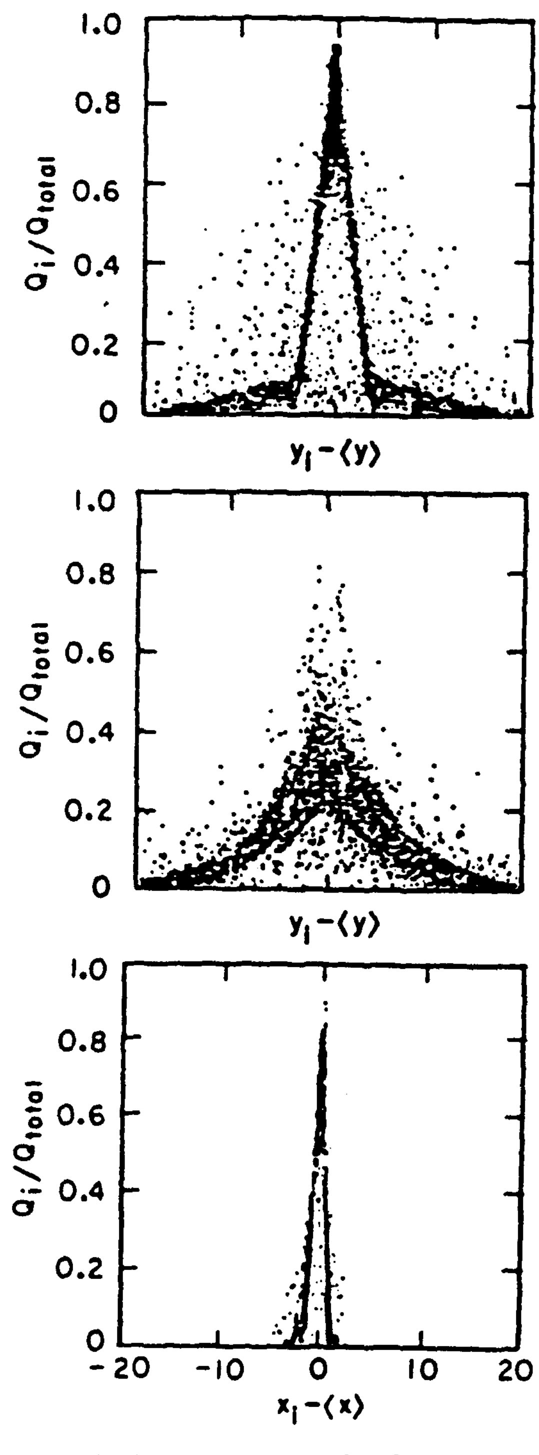


Figure 5.12. The distribution of induced pulses on Y–strips, normalized to the central strip; (upper) the 4 cm wide Y–strips are mounted on the top of the LST, (middle) the 4 cm wide Y–strips are mounted on the bottom of the LST, (lower) the corresponding charge distribution on 1 cm wide X–strip.

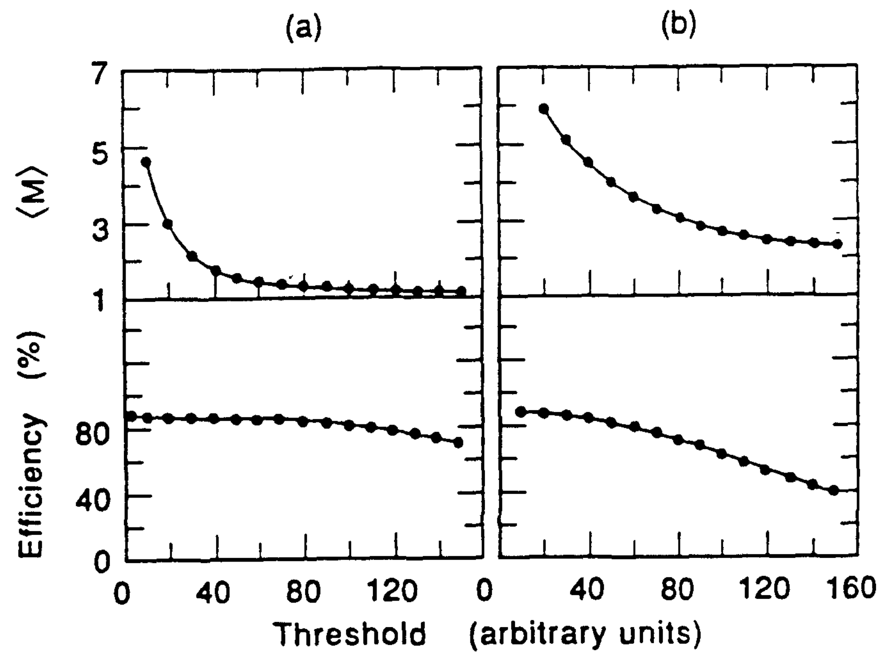


Figure 5.13. Correlation of the Y–strip efficiency with the Y–strip multiplicity for the Y–strips mounted (a) top of the LST and (b) bottom of the LST. In horizontal scale 100 units is approximately 2.22 mV.

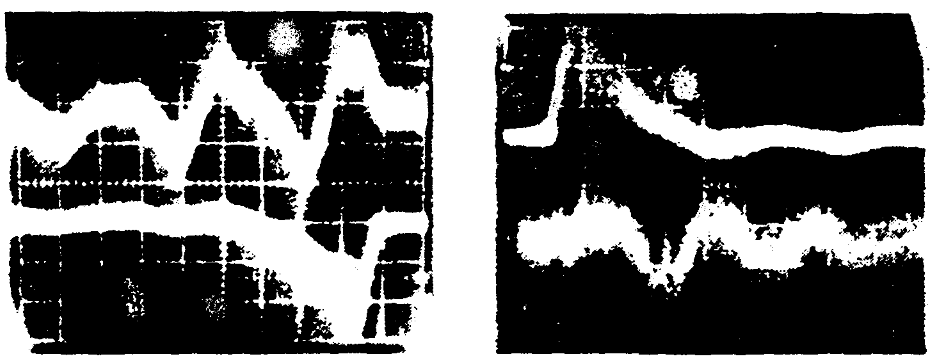

Figure 5.14. The pulses on the central (upper left) and adjacent (upper right) pads into 50 Ω. Pads adjacent along the module (lower left) have larger cross talk than those adjacent but not sharing a LST module (lower right).

zero for the adjacent pads covering two different LSTs.

In Fig. 5.16 is shown that since each electrode covers about one–half of the total solid angle around the streamer, the charge collected from one electrode

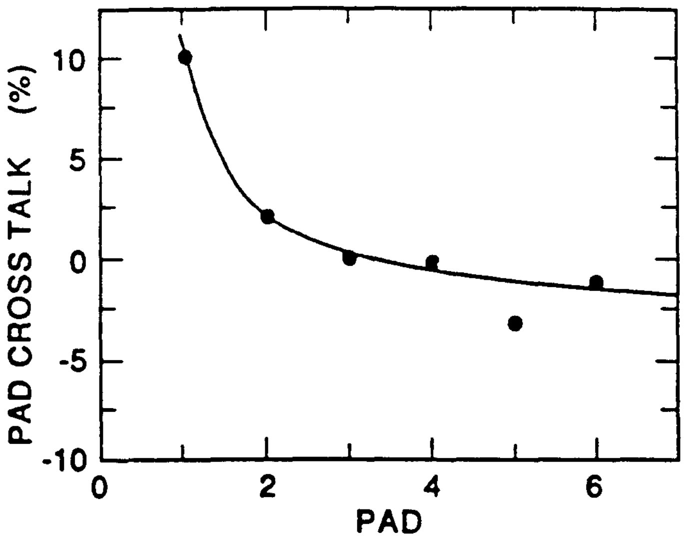


Figure 5.15. The pad–to–pad cross talk along the same LST chamber. The center pad was in the middle of a 6 m long LST.

should be equal to one–half of the charge on the wire, therefore, sum of the charge accumulated on both electrodes is expected to be equal to the wire charge. Fig. 5.17 shows how the geometrical fluctuations of the streamer pulse may reflect on the charge collected by electrodes. That means, if the nearest primary electron pair reaches the wire from the bottom side of a LST chamber, the streamer will then propagate towards the bottom side; in this case the charge collected on the strip will be larger than the top placed pad charge. These fluctuations do contribute to the cathodic pulse height resolution but they are dominated by the fluctuations of the streamer formation itself.

Fig. 5.18 gives the summed pulse height of one electrode versus the other for a LST chamber operated with the "new mixture".

## 5.4 Spatial Uniformity of the LSTs

A study[52] of the spatial uniformity of the *SLD* LSTs has been made by using the eight 6 m long tubes operated with the "standard mixture" at 4.65 kV. Four of the eight LSTs were graphite recoated on the top of the walls which is the standard procedure and the other four were not recoated.

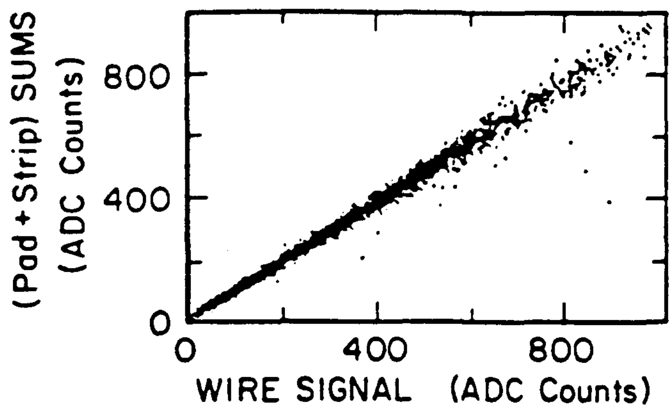


Figure 5.16. The charge collected on the wire versus on the sum of the external electrodes.

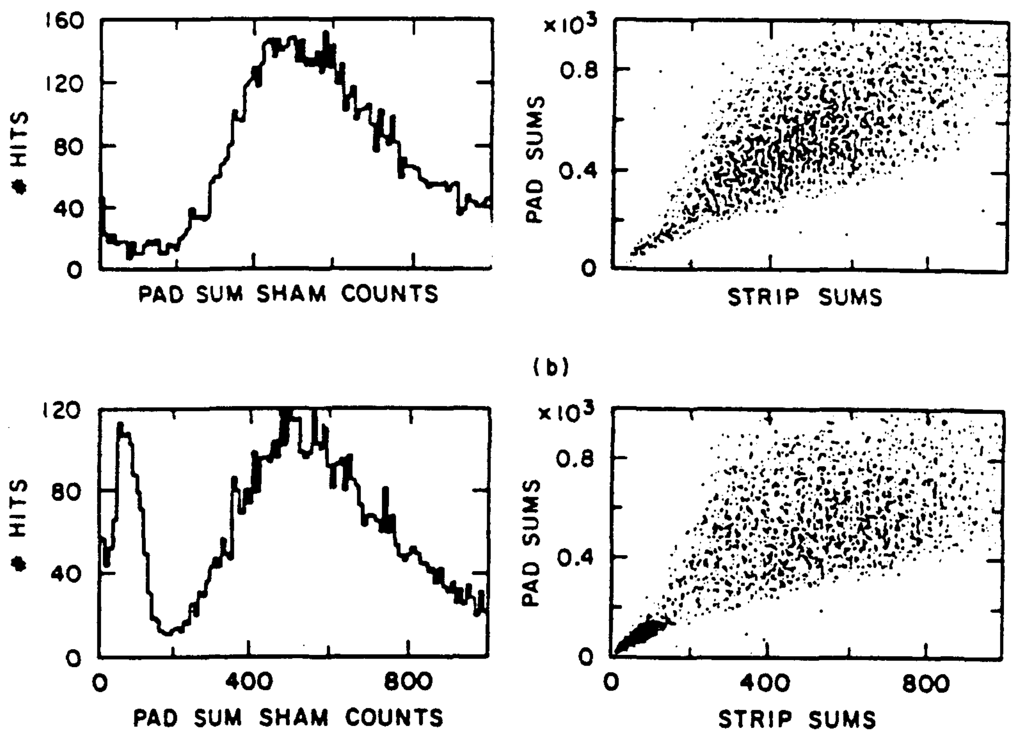


Figure 5.17. The sum of the charge collected on the pads versus the strips charge for a LST chamber operated with argon (25%) - isobutane (75%) at 4.65 kV (upper) and argon (35%) - isobutane (65%) at 4.10 kV (lower). The pulse heights are given in arbitrary units.

The longitudinal uniformity was measured by placing a $Ru^{106}$ source at the center of the LST for every two feet starting from the HV end. The

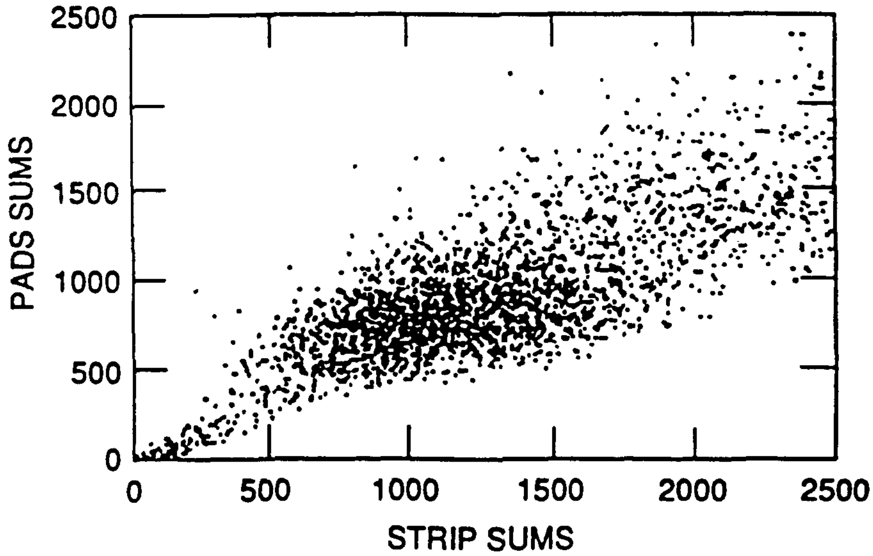


Figure 5.18. The sum of the charge collected on the pads versus the strips charge. The LST chamber was operated with the (2.5%)Ar+(9.5%)$C_4H_{10}$+(88%)$CO_2$ mixture at 4.75 kV. The pulse heights are given in arbitrary units.

pulses on the wires were sent into a QVT and a scintillator was used for the trigger. The measurements have shown that with the threshold used, there are no systematic variations over the length of a single LST, but average charge varies from one tube to another. Fig. 5.19 shows the histogram of the ratio $\frac{Q_i}{<Q>}$ for 80 measurements. Note that the LST response is uniform along the its length within $\approx$ 7.6% (the width of the normalized distribution). The Q spectrums taken along the LSTs show that the spatial nonuniformity does not affect the LST spatial resolution.

A detailed study on the spatial resolution of WIC chambers with the cosmic rays will be presented in section 6.7.2.

## 5.5 Operating Point

In order to obtain efficient calorimetry and muon tracking in the WIC, the definition of the chamber operating point is very important. The *SLD* WIC group has performed many tests in order to determine the optimal parameters taking into account the requirements of the experiment.

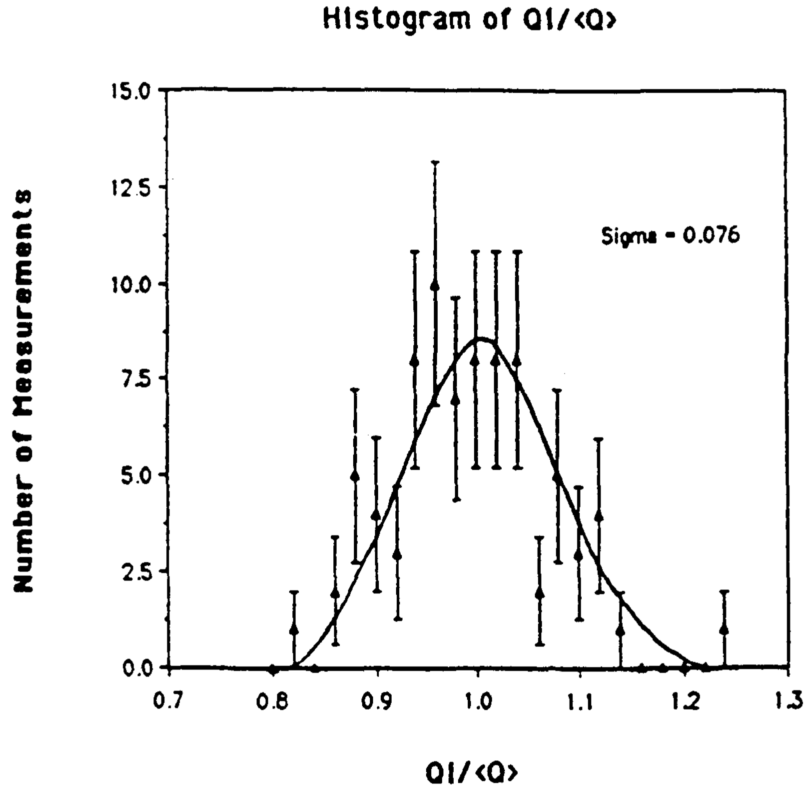


Figure 5.19. **Histogram of the normalized peak $Q_i$ values over the mean charge $<Q>$ for each tested extrusion.**

The studies performed have shown that the most important parameters for defining the operating point are; the gas mixture, the applied HV, the discriminator threshold and the ambiental conditions (temperature and pressure). These parameters are discussed in the following.

- At the beginning, (as we mentioned also in Chapter 2) the gas mixture used for the tests of the WIC LSTs was the (1+3 $\rightarrow$ Ar+Iso), so–called "standard mixture". In order to understand the operational characteristics of these detectors, the standard mixture has been studied in detail by the group, including the long term test of which results will be mentioned in Chapter 6. Meanwhile, because of the *SLD* safety requirements, we have started the search of alternative "non flammable" gas mixture(s) having similar operational characteristics to the "standard" one. We have developed a three component mixture (Isobutane (9.5%), Argon (2.5%), $CO_2$ (88%)) which has good operational characteristics and it is nonflammable. Details of this study will be given in Appendix A.

The operating point for the "standard mixture" has been established at 4.65 kV as the point where 95% of the avalanches are in streamer mode. Fig. 5.20 shows the pulse height distribution,versus HV; the proportional to streamer transition can easily be seen for different concentrations of Argon–Isobutane as a function of applied HV. In Fig. 5.21 and Fig. 5.22 are shown the single rate curves of two 6m long tubes (with and without bottom graphite coating) with cosmic rays and the pulse height distribution for various argon–isobutane compositions, respectively.
Using the same criteria to define the operating point for the "standard mixture", we have defined the operating point for the "new mixture" at 4.75 kV.

- We also studied the effects due to a change of the applied HV. The measurements have shown that, the collected charge on the pads depends on the HV following the relation $dQ/Q = 8\ dV/V$. The HV power supplies used for the WIC chambers, soddisfies the restrict requirement of having $dV/V$ better than 0.1%.
- Increase of the pressure reduces all streamer spatial dimensions leading to a reduction of the pulse height. The reason is that the gas density increase at higher pressure decreasing the electron mean free path and the energy gain between collisions, reducing also the number of secondary ionizations per unit length. Fig. 5.23 shows how the average pads charge change as a function of the temperature.
  From the data we find the following relations between the operating voltage, the temperature and the pressure;

$$\frac{dQ}{Q} = K_T \frac{dT}{T} \tag{5.3}$$

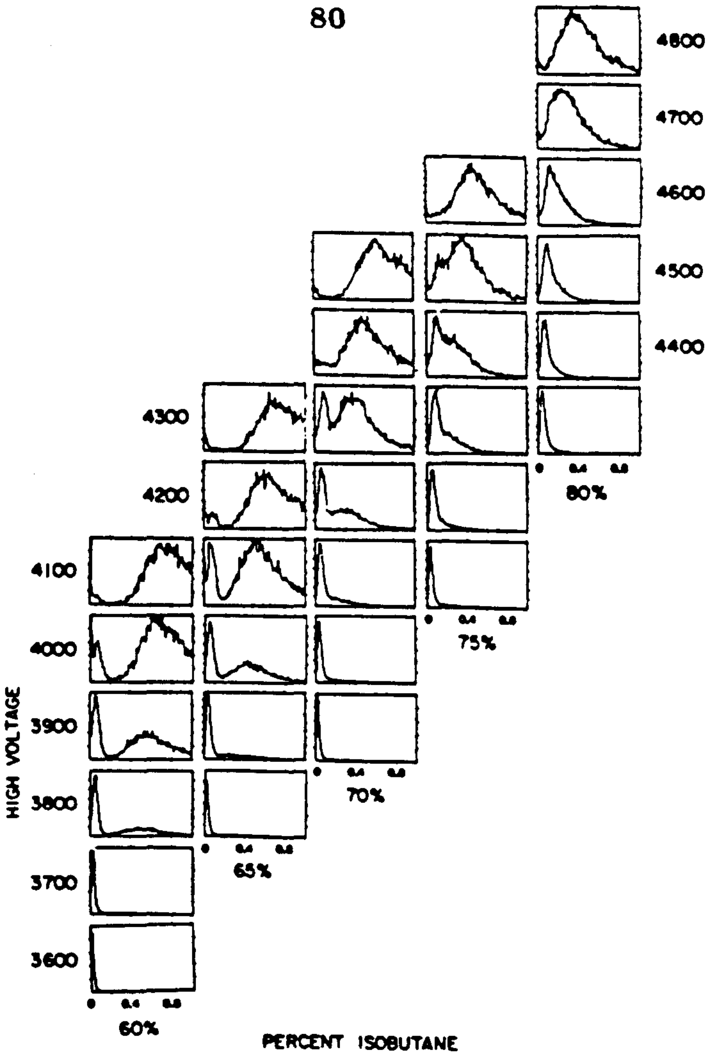


Figure 5.20. **Pulse height spectra as a function of HV and the isobutane concentration for various argon–isobutane mixtures. Note that at 4.6 kV for the "standard mixture" (75% isobutane) one has the fully streamer pulse.**

$$\frac{dQ}{Q} = -(9.1 \pm 1.0)\frac{dP}{P} \tag{5.4}$$

where T is the absolute temperature in Kelvin, P is the pressure in bar, $K_T = 10.4 \pm 0.5$ for the "standard mixture", $7.5 \pm 0.5$ for the three component nonflammable "new mixture". The relation (5.4) has been obtained for the "standard mixture" at 4.65 kV.

From (5.3) and (5.4) we can write a general expression where the operating

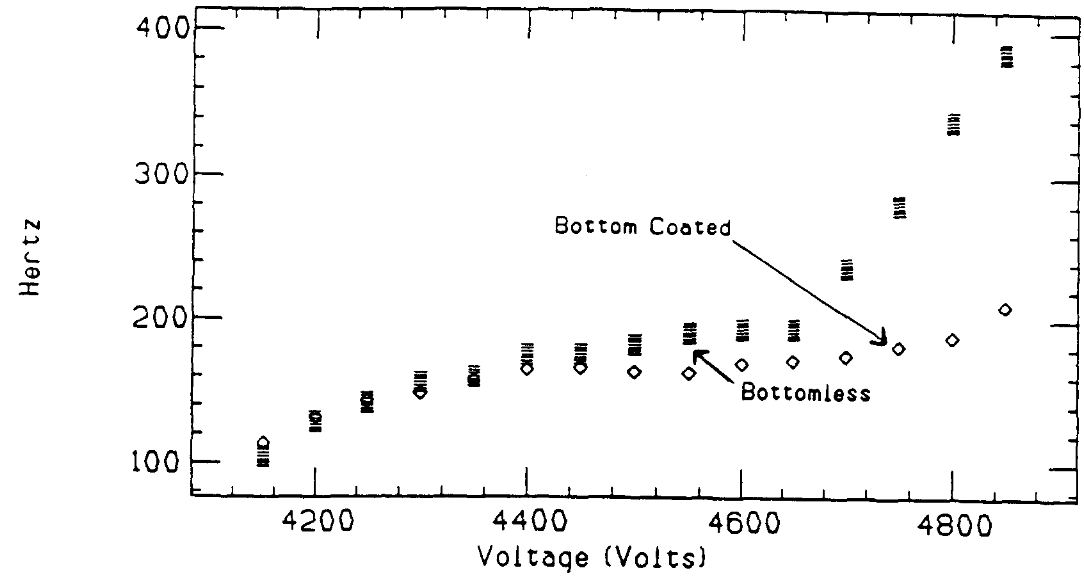


Figure 5.21. **Single rate plateau curve with cosmic rays of two 6 m long LSTs with and without bottom graphite coating. Threshold was 1 mV (at tube level), discriminator dead time was 500 $\mu s$ and the tubes were operated with the "standard mixture".**

**voltage, the pressure and the temperature are all present, as**

$$\frac{\Delta V}{V} = \frac{K_T}{K_V}\left(\frac{\Delta T}{T} - \frac{\Delta P}{P}\right) \tag{5.5}$$

**V is in kV.**

**The knowledge of the dependence from the temperature and pressure is very important because the transition between the proportional and the streamer mode is strongly affected by changes in these quantities.**

- **The dependence of the LST performance from small changes in the gas mixture and purity[53] has also been studied. The measurements have shown that the charge resolution, dQ/Q, varies as dQ/Q=dA/A for the "new mixture" and, dQ/Q=4.5 dA/A for the "standard mixture", where A is the Ar concentration in the mixture. In the second case it corresponds to a change of 18-19% on the mean pad charge for ± 1% variation of the relative concentrations of argon and isobutane. The investigation on the gas purity in particular, on the water contamination in the gas**

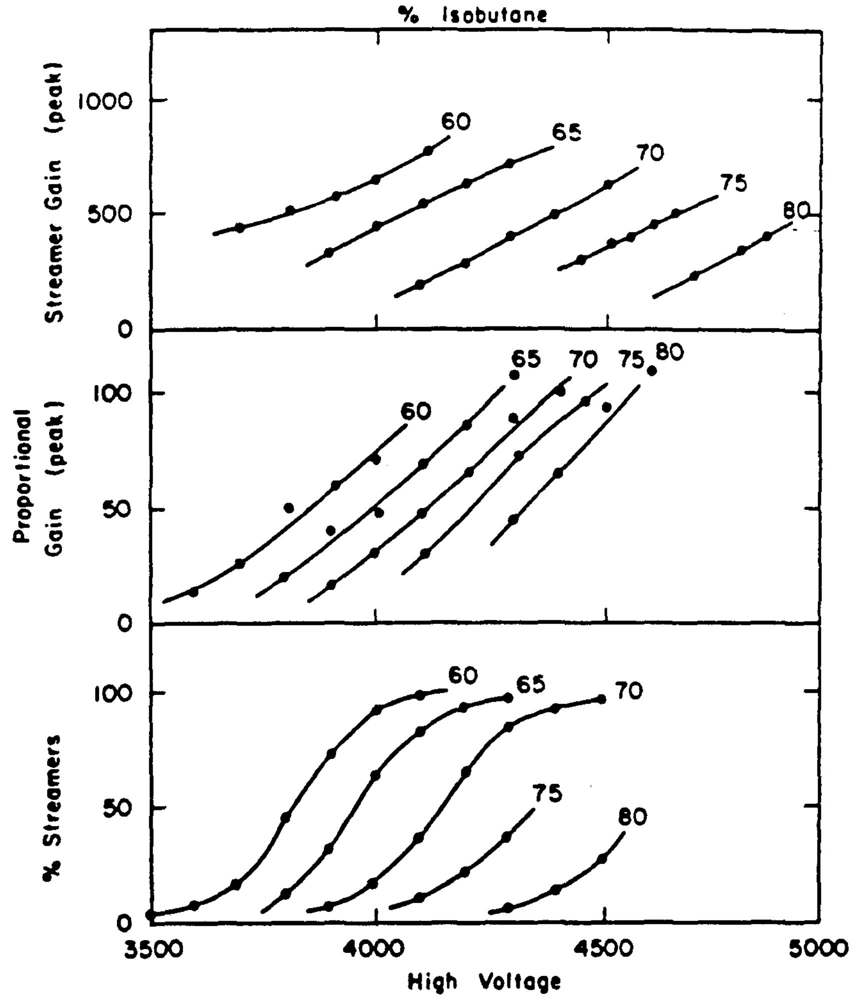


Figure 5.22. **The peak of the; streamer pulse height distribution (upper), proportional pulse height distribution (middle), and the percentage of the pulses in the streamer mode (lower), for various concentrations of isobutane in argon versus high voltage.**

through the PVC sleeves has shown that only rather high concentration of the water does affect the operating point since it is electronegative and extremely polar. Fig. 5.24 shows the percent of water as function of ambient humidity inside the modules when the total gas volume changed every 10 hours. Fig. 5.25 shows the strip efficiency as a function of the discriminator setting for three different concentrations of water. As a result of these studies we can say that, if the water content in the gas

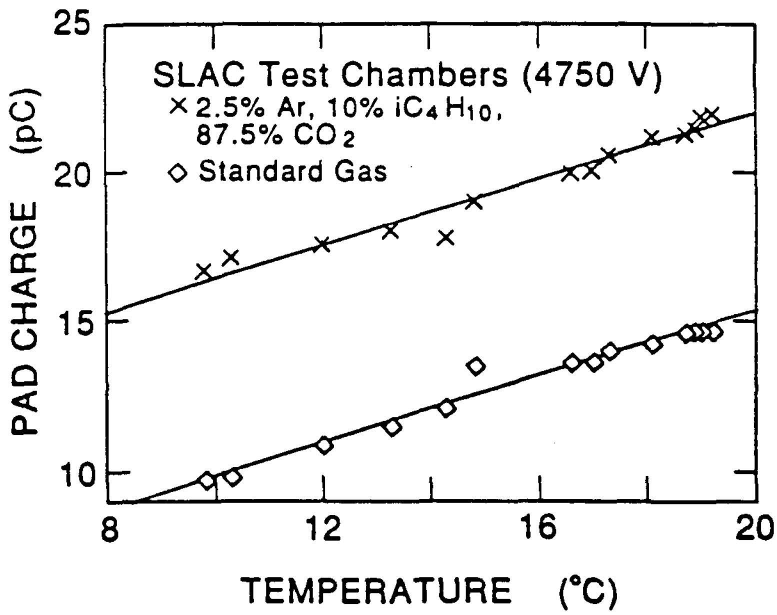


Figure 5.23. The integrated pad charge versus ambient temperature at constant pressure for two different gas mixtures.

volume is less than 1%, it does not affect the operating characteristics of LST chambers; if the percentage of the water is higher, charge and spatial resolutions on pads and strips tend to decrease.

The other impurities found in the bulk grade gas (propane $\approx$ 1.4% and butane $\approx$ 7%) did not affect the operation of the LST chambers.
Also changes in the gas flow rate (from one volume change every few hours to one every 48 hours) did not demonstrate any difference in the operational performances of the LSTs.

The conclusion of our study was that careful monitoring of high voltage, temperature, pressure and the gas composition is necessary during the experiment operation.

### *5.5.1 Analysis on the Proportional Mode*

The *SLD* WIC group has also analyzed the operational performances of the LST chambers operating in proportional mode[54] in order to establish to which extent this mode could be an alternative to the streamer one. We found that

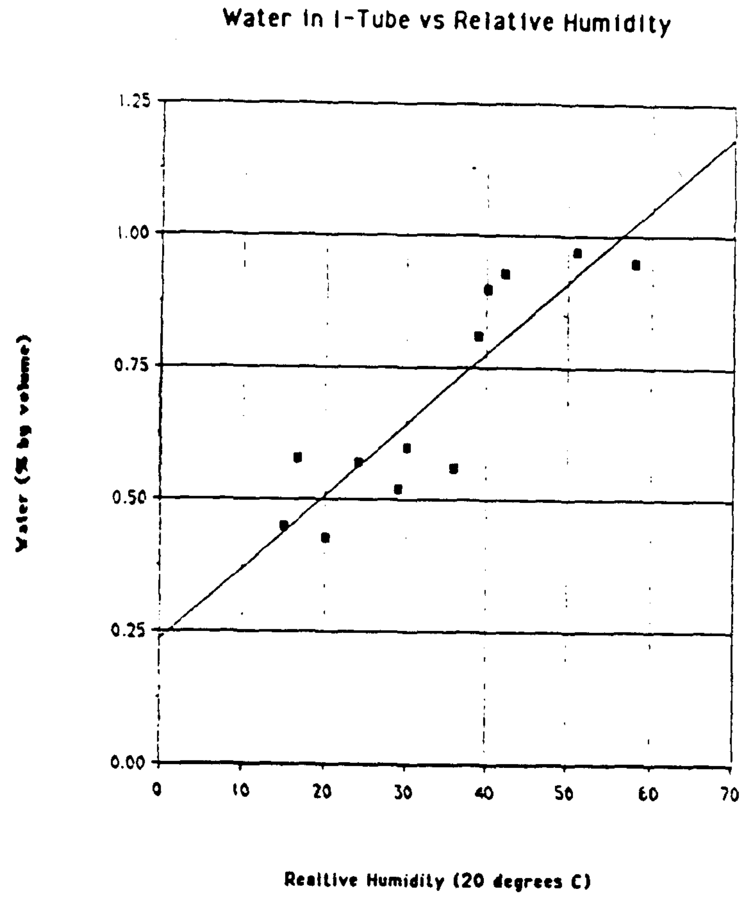


Figure 5.24. Water in the LST versus relative humidity at 20° C.

the amplitude of the proportional pulses are about a factor 5 smaller than the streamer pulses for cosmic rays.

Running in the fully proportional region requires first of all, a lower discriminator threshold and this could create problems worsening the signal/noise ratio. Raising the voltage up to the so–called saturated proportional regime (4.2÷4.3 kV) where the avalanche is not proportional anymore to the energy loss reduces the problem of the signal/noise.

The tests have been performed with a LSTs chamber equipped with pad and strip readout placed between two 65 cm long photomultipliers; one LST had only 1 wire in order to get the single strip pulse and all pulses from the strips were sent into a 16 channel (×10) amplifier and than into a QVT. Fig. 5.26.

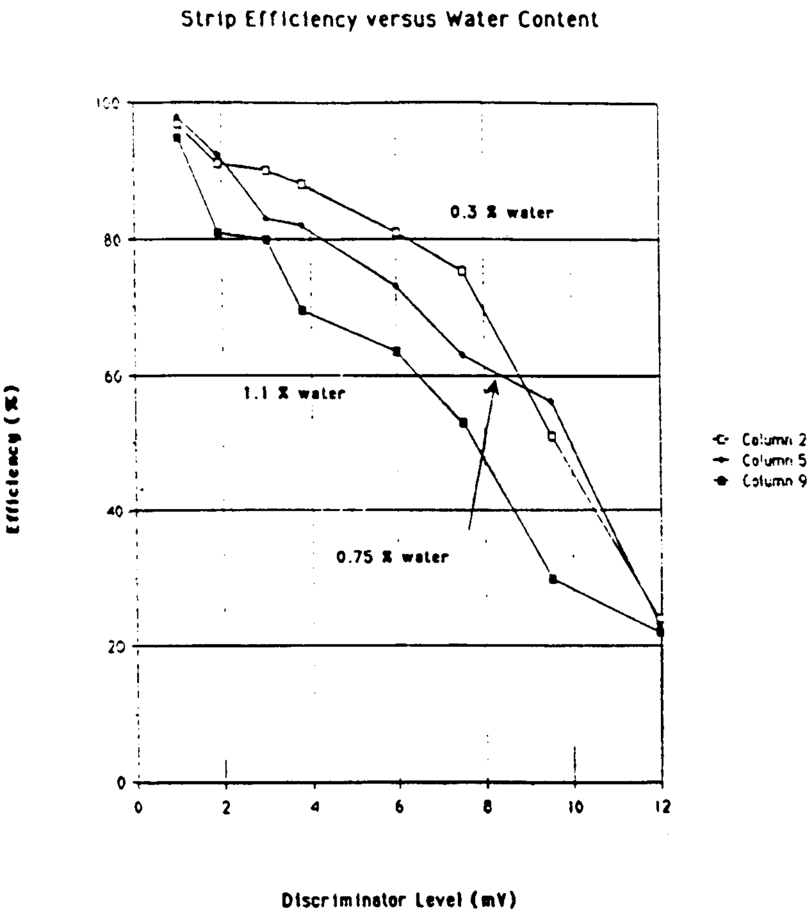


Figure 5.25. Strip efficiency versus water content for various discriminator levels.

shows the charge distribution for the wire, hit and adjacent strips.

The conclusion of this study was that in the case of the strips, appropriate threshold setting and good shielding of the system were essential in order to reach a viable signal/noise ratio and high efficiency. The problem was found less important in the case of pads readout.

## 5.6 Radiation Damage Studies

When a gas counter is exposed to radiation, during the avalanche process, the hydrocarbon polymerization can occur at the vicinity of the wires[55]. This causes film deposits on the anodic wire reducing the performance and the

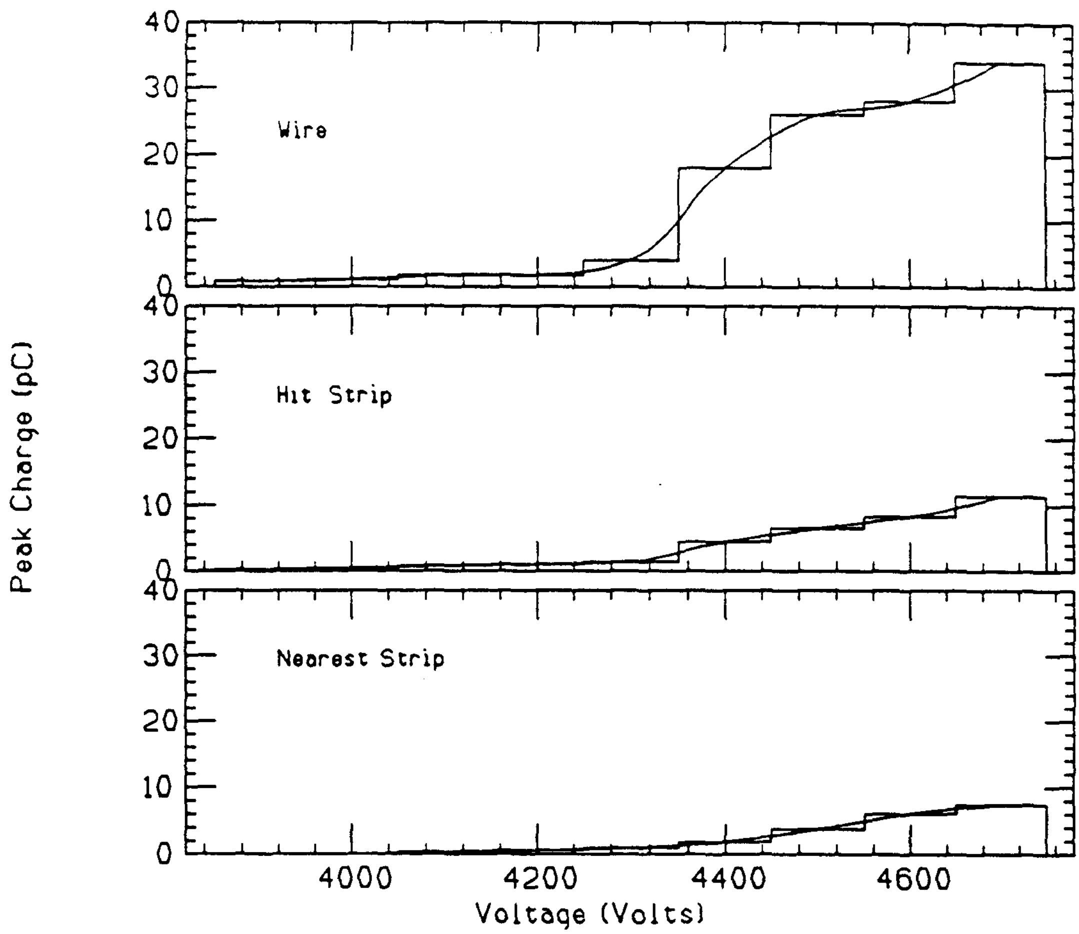


Figure 5.26. **Charge distributions of wire, "hit" and nearest strips versus operating voltages. The mixture used was the "standard" one.**

longevity of the chamber.

Radiation damages on WIC LSTs was induced[56] by a 16 $\mu$C $Ru^{106}$ $\beta$–source (3.5 MeV endpoint energy). The mean pulse height was normalized to the average pulse of two fiducial regions adjacent to the irradiated region to correct the possible instabilities that can occur. For the measurements a 6 m long LST was operated at 4.65 kV with the "standard mixture" containing also roughly 1% (by volume) of water because of humidity.

The $Ru^{106}$ source was placed directly on the ground shield of the LST and was illuminating an area of approximately 1 $cm^2$. Under these conditions the current drawn by the LST was $< i > \approx 2.5$ $\mu$A corresponding to a counting rate of 12 kHz with a discriminator threshold of 3.8 mV. The total charge accumulated per day was then about 0.22 C and the background current was $< i > \approx 0.06\ \mu$A due to the cosmic rays and other background.

The results of the study are shown in Fig. 5.27. During the first Coulomb of deposited charge, the average charge decreases by about 13% but for the higher values remains constant up to about 4 C.

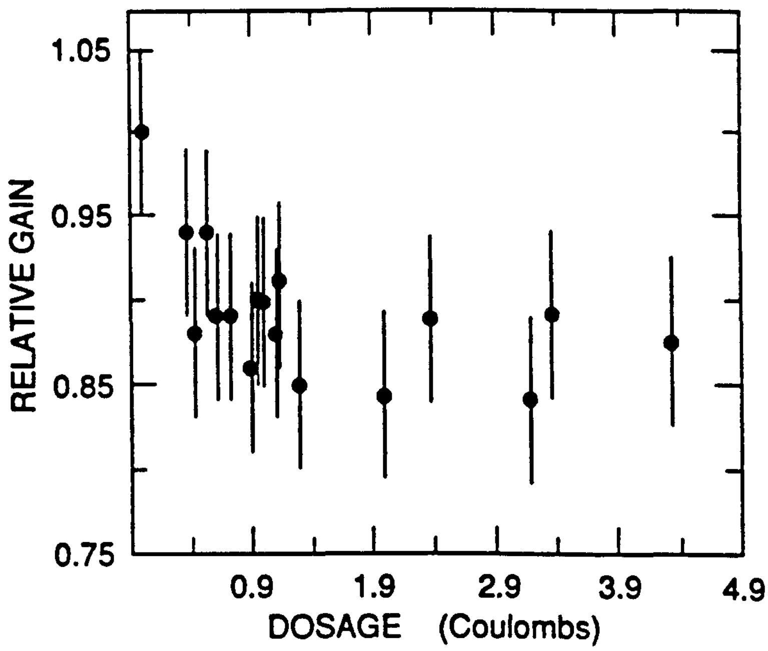


Figure 5.27. The mean charge per pulse on the wire as a function of the accumulated radiation measured in Coulombs integrated on the anode wire.

An investigation on the existence of the possible degeneration effects induced by high counting rates has also been done by the Nusex group[57]. The final result was that after the integration of $\approx$ 1.6 C charge ($\approx 2.6 \times 10^{10}$ particles), the tube has operated at knee voltage up to 1 kHz/cm$^2$, while, 250 V above the knee the maximum tolerable rate was 250 Hz. The test was performed with 35+65, Ar+Iso and a $\beta$ source was used for the irradiation.

In conclusion, the radiation damage seems not to be a problem for *SLD* LSTs, since in this experiment they will be exposed to the radiation dosages several orders of magnitude less than the above values.

# Chapter 6. Life, Cosmic Ray and WIC Prototype Tests

## 6.1 Introduction

In the first section of this Chapter we will present the results of a massive test, the so–called lifetime test performed with a set of LST modules.

In the second and third sections respectively, we will discuss procedures used to ensure the quality and the reliability of all the LSTs and WIC chambers before the installation in their final locations.

In the last section we will give the results of the beam test performed with the WIC prototype.

## 6.2 Long–Term Test, the Choice of the Criteria & Test Description

Almost all groups which use the LSTs in their detectors have been or are being realized a large–scale test. The aim of this test, at least for the *SLD* group, was to study and understand the long term behavior and the longevity of the LST modules. The basic reason is, the chambers will not be accessible (at least in the barrel) after the installation into the *SLD* iron gaps for the duration of the experiment which is about 5 years. Therefore, it has been decided that the reliability of these devices must be high enough to survive for this period of time without exceeding a total of $\approx$ 10% of failure rate which is less than about 2% per year.

The lifetime test for the WIC modules has been performed by operating two sets of LSTs in two different regimes (see Chapters 3 and 5) which are the streamer regime (at 4.65 kV with the "standard mixture") and the proportional regime (at 4.1 kV).

The different experimental groups have defined different "acceptance criteria" and there are in principle, some basic criteria which have been used by

Table 6.1. Acceptance criteria for various experiments.

| Acceptance Criteria | | | | | |
|---|---|---|---|---|---|
| Experiments | LST Modules Tested | Average Current | Current Burst | Source | Cosmic Ray Test |
| CHARM II | 20,000 | X | | | |
| DELPHI | 10,000 | X | | X | |
| UA1 | 8,000 | X | | | |
| ALEPH | 7,000 | X | | | |
| OPAL | 4,500 | X | | X | |
| SLD | 4,000 | X | X | | X |

these groups for the definition of the "good" module from which a good longevity can be expected. These criteria can be summarized as following;

1. current spikes should not exceed 1 $\mu$A more than 1 minute in 48 hours,
2. the average current must be less than 100 nA (for 6m long LSTs), which approximately corresponds to the cosmic rays background,
3. during the passage of a source (which gives $\approx$ 1 $\mu$A) along the module with a velocity about 10 cm/sec must not be observed persistent currents.

In Table 6.1 summarized are the various type of tests performed by different groups before accepting a "good" module. Table 6.2 shows some lifetime test results obtained from these groups.

The *SLD* WIC group has performed two independent lifetime tests in two different places simultaneously, the one of which setup and results described here, was performed at the Campana module factory with 720 modules. Similarly, the other test performed at SLAC using about the same number of modules. The combined results of these tests will be given later in this Chapter.

## 6.3 Test Setup

Fig. 6.1 shows how the 10 Campana batches (a batch is a group of 80 LST

Table 6.2. Data on the longevity of LSTs from various experiments.

| **LSTs Longevity Data** | | | | | |
|---|---|---|---|---|---|
| Experiments | LST Modules Tested | Duration (Years) | Equivalent Module–Years | Approximate %Fail | Comments |
| NUSEX | 5,000 | 4 | 20,000 | 1÷2% | |
| CHARM II | 20,000 | 1 | 15000 | 1÷3% | |
| UA1 | 8,000 | 0.5 | 3,000 | 1% | HV off every few hours. |
| SLD | 700 | 0.3 | 120 | 0% | HV off every 12 hours. Streamer mode operation. |
| SLD | 700 | 0.3 | 100 | 1÷7% | As above, prop. mode operation |
| ALEPH | 1000 | 0.16 | 150 | 1÷2% | |
| OPAL | 200 | 0.5 | 100 | 0% | Breox coated. HV off whenever $I > 2\ \mu A$ per 7 modules. Initially 2% failed. |
| OPAL | 200 | 0.25 | 50 | 0% | As above, but non–Breox coated. Initially 5% failed. |

modules) were placed on 3 racks, the gas flow, and the readout channels. Each row on a rack contains 10 daisy chained modules and each module has a 10 MΩ (1 MΩ during the conditioning test) limiting resistance in series with the HV. HV was provided to each row by one of the 40 channels of an intelligent CAEN power supply and a total of 3 CAENs were monitored by an IBM–PC.

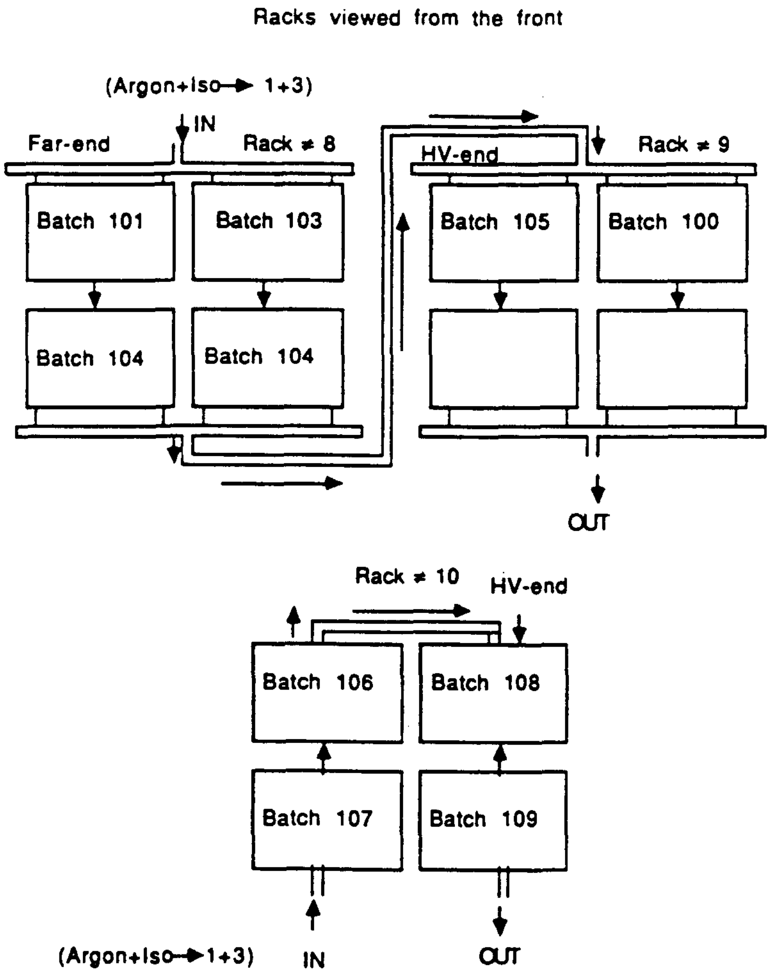


Figure 6.1. The view of the racks & gas flow used for the Campana lifetime test.

The gas flow was controlled by a Datametric mass flow meter & controller; the "standard mixture" (25% Ar+75% Iso) was used for this test and each batch was flowed for at least 10 volume changes before starting the test.

## 6.4 Test Description

### *6.4.1 Conditioning Test*

The "conditioning" process is based on the following idea.

It has been widely observed that immediately after the construction, a large fraction of LST modules cannot support the operating voltages and they draw rather high currents at low voltages. That is probably due to the presence of dust and dirt inside the modules. A solution for this problem is to ramp the voltage up and down repeatedly until a value higher than the operating voltage is reached without drawing anomalous current.

In the official test procedure, the serially connected 10 modules in each row were connected to one channel of the CAEN power supply and each channel was programmed to perform a conditioning sequence up to a maximum voltage of 5.0 kV and tolerating a maximum current of 5÷10 $\mu$A; in case of a trip, a return to 0 V was provided. The duration of the conditioning process was established to 72 hours for every module. If a module was continuously tripping for more than one hour it was disconnected from the remainder of test; similarly, if it could not reach to 5.0 kV at the end of the 72 hours it was defined as a "conditioning failure".

### *6.4.2 Soak Test*

In this step of the test, modules having the same connection as in conditioning test, were continuously kept for 6 days at 4.8 kV which is about 150 V higher than the operating point (4.65 kV). The aim of the soak test was to observe the small percentage ($\approx$ %1) of modules which draws the sudden currents up to 200 $\mu$A causing the gas soiling because of a possible plastic burning in the module. Therefore, during this test the power supply current limit was set to the 200 $\mu$A and every 12 hours each module drawing more than 20 $\mu$A was disconnected from the remainder of test and was defined as "high voltage soak failure".

### *6.4.3 Acceptance Test*

During this test the current was read from the ground returns of the modules through an interface card shown in Figure 6.2. The software set up on the PC was able to take 1 sample every ≈ 20 seconds; each HV channel was daisy-chained over ten modules with a 10 MΩ limiting resistor in series with each module.

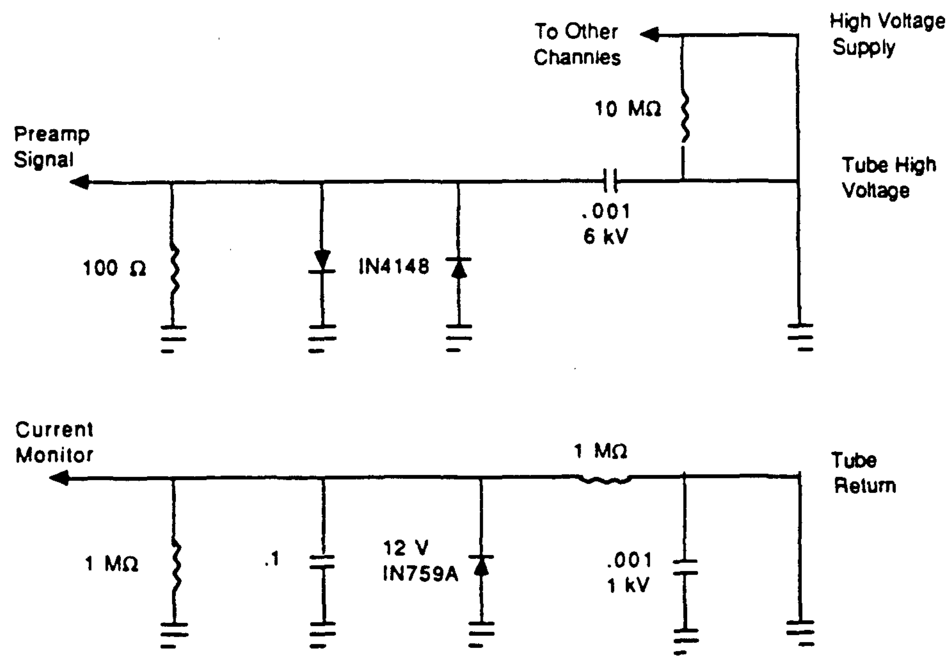


Figure 6.2. *SLD* **test interface card.**

The goal of this test was to keep the modules under 4.8 kV stable voltage for a total of 72 hours and monitor their current during the last 48 hours. To define a module as "bad module", during the last 48 hours it had to draw either

1) more than 0.1 $\mu$A average current,

or

2) more than 1.0 $\mu$A for any period of 1 minute (current trip).

The definition of the first point as a rejection criteria is the result of the analysis performed[58] with two batches of modules (200 modules each) at SLAC. In Figure 6.3 we see the average and peak current as a function of time over one acceptance test period (48 hours) for two modules tested at SLAC. In both modules the average current is less than 100 nA but as we see in the upper plot of Figure 6.3 the good one is less "stable" than the bad, at least in the peak

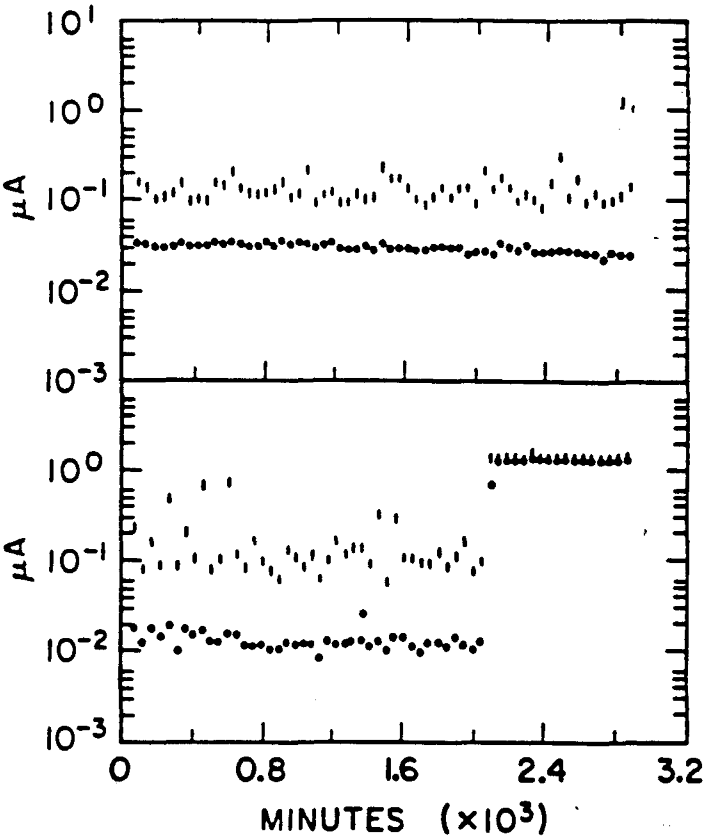


Figure 6.3. Average current (dots) and peak current (bars) for a module passed the acceptance test (upper) and one which failed (lower).

currents.

Figure 6.4 shows the average and peak currents drawn by the 3000 modules The average current shows a peak at $\approx 10\div20$ nA with a long tail extending up to 1 $\mu$A. The cut on the average current has been applied because of the very high probability that this tail can be attributed to the construction problems. It should be pointed out that the response to the source test[58] of the bad modules was normal; therefore, one can say that the modules which draw about 1 $\mu$A average current could be good detection elements, but on the other hand, they have higher probability of failing over a long period of operation; for this reason they were discarded.

As we see from Fig. 6.4 a very large amount of modules did not draw more than

2 $\mu$A. From these two plots it is clear that exist a group of "bad" modules which can not be selected if only the first criteria is applied.

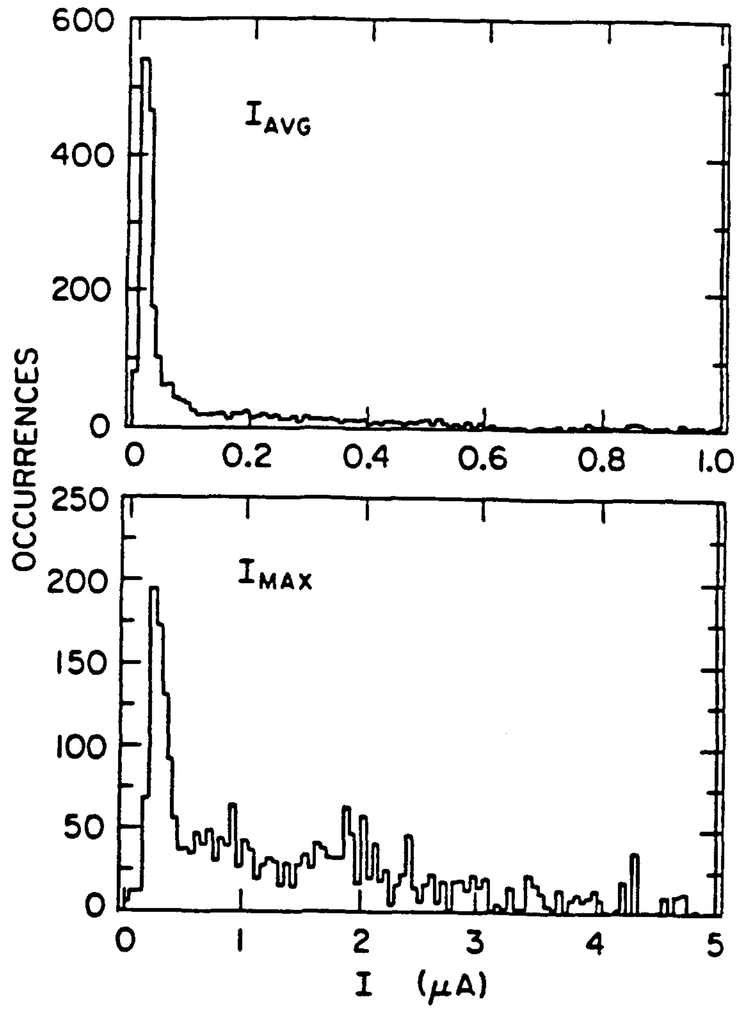


Figure 6.4. **Average (upper) and peak (lower) currents drawn by 3000 modules during the 48 hours of the acceptance test.**

At this point, a new criteria is needed to separate these two different group of "bad" modules, which is the second cut mentioned above. The minimum trip duration required has been defined in such a way that at least three consecutive readings ($\approx$ 20 sec/sample) should be performed to avoid occasional erratic readings due to the electronic system. Figure 6.5 shows the number of modules which failed the trip criteria and the average current of the modules which at least one time have drawn 1 $\mu$A for more than 1 minute. The analysis has shown that almost 50% of the modules failed the second criteria (trip criteria) and/or had 1 or 2 trips of less than 2 minutes.

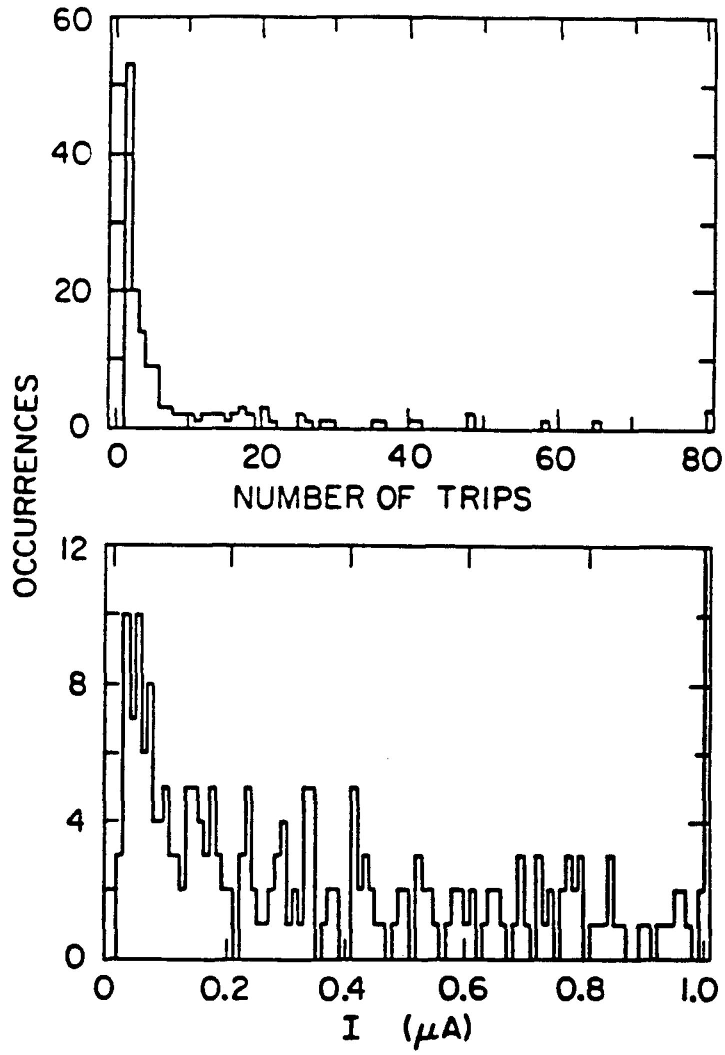


Figure 6.5. The number of modules failed the trip criteria (upper), the average current of the modules which had at least one current trip, before the average current cut was applied (lower).

The modules that failed during the acceptance were not disconnected in order to observe the long term behavior of the bad modules.

The modules which survived the above steps were then started to the lifetime test described in the following subsection. Of these modules 50% were operated in the proportional mode. This means the soak and acceptance tests were performed at 4.25 kV while the lifetime test was performed at 4.1 kV.

## 6.5 Lifetime Test

During the lifetime test, the modules were kept at fixed voltages for a period of time of more than 3 months. During the lifetime tests (both at Campana and SLAC) the high voltage was switched on and off every 12 hours for 10 minutes as it will happen during the operation of the detector. The current was monitored from the HV ground returns and every 15 minutes the average and maximum currents were recorded.

To define a module "lifetime test failure", thus disconnect it from the remainder of the test, the module had to draw a more than 200 $\mu$A steady current or 20 $\mu$A for $\geq$ 10% of total time. Figure 6.6 we show the average, maximum currents for 10 modules operated at two different voltages, at 4.65 kV (streamer) and at 4.1 kV (proportional), of the Campana lifetime test.

## 6.6 Lifetime Test Results and Statistics

In order to obtain a reliable result and to establish an experimental failure limit $\leq$ 2% per year, 0 failures in $\geq 42,600$ tube $\cdot$ day should be observed. Table 6.3 shows the overall result of the Campana lifetime test. In this test it has been observed one official failure over 20,100 integrated tube $\cdot$ day in the group of modules operated in proportional mode, and 0 failure in 31,720 integrated tube $\cdot$ day operated in limited streamer.

We found three other (non official) failures of which one had already failed the acceptance test but was not disconnected from the lifetime test while the top of the walls of the other two modules were not recoated.

The final result is obtained by combining the Campana and SLAC lifetime test results. Table 6.4. shows the final result.

## 6.7 Routine Test Procedures for the LSTs of WIC

After the encouraging results of the lifetime test, all the LSTs before to be

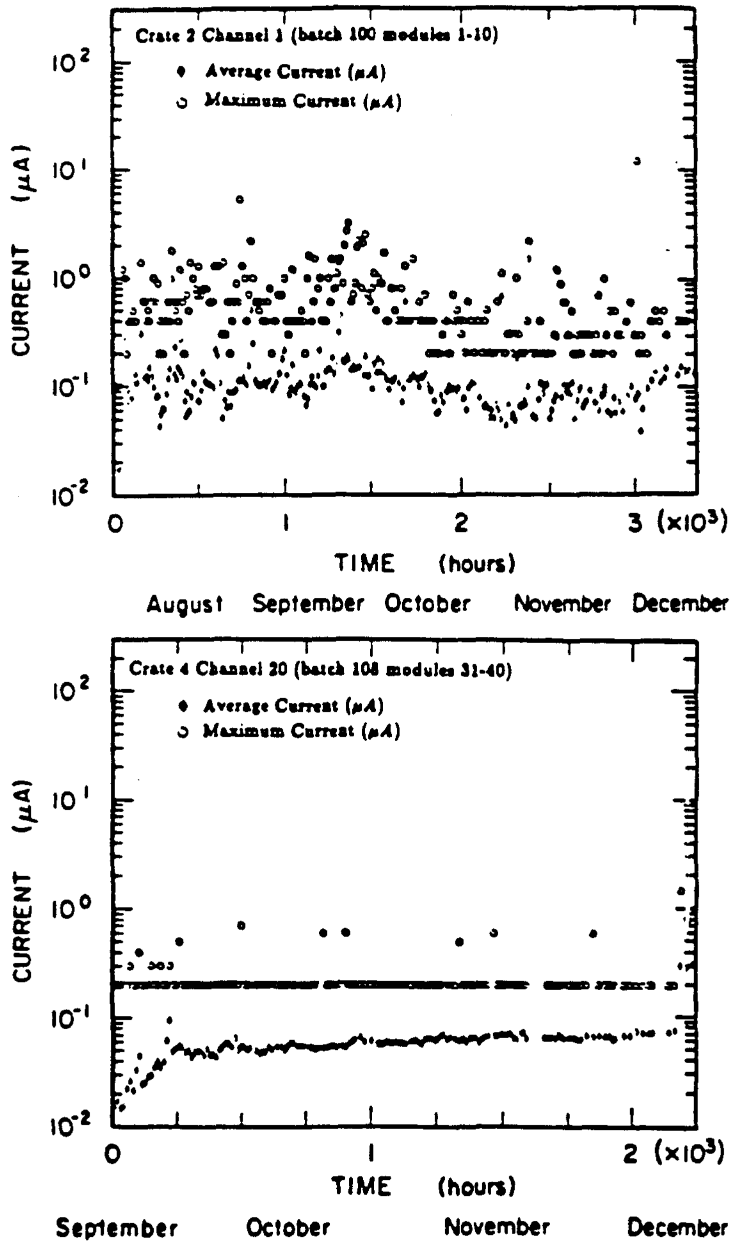


Figure 6.6. **Average and peak currents of 10 modules operated in streamer mode (upper) and in proportional mode (lower) for about 1.5 $\times 10^3$ hours during the Campana lifetime test.**

installed in the WIC chambers were tested at SLAC in a way similar to the first steps of the lifetime test procedure. This test consisted of two phases.

### *6.7.1 First Phase*

The LSTs were submitted to the "conditioning test" as discussed above

Table 6.3. Summary of the Campana lifetime test of 720 LSTs.

| Campana Lifetime Test Results | | |
|---|---|---|
| | Lifetime at 4.65 kV (Streamer mode) | Lifetime at 4.1 kV (Proportional mode) |
| Total modules | 400 | 320 |
| Conditioning failures | 17 | 29 |
| Soak failures | 21 | 0 |
| Acceptance failures | 74 | 31 |
| Subtotal loss (%) | 28% | 19% |
| On lifetime | 288 | 260 |
| Lifetime failures | 0 | 1 |
| tube · day | 31,720 | 20,100 |

Table 6.4. Combined SLAC–Campana lifetime test result.

| SLAC–Lifetime test | | | |
|---|---|---|---|
| $V_{test}$ | tube · day | # of failures | failure rate (90% CL) |
| 4.65 kV | 14,138 | 0 | $\leq$ 5.9% per year |
| 4.1 kV | 13,016 | 0 | $\leq$ 6.4% per year |
| **CAMPANA–Lifetime test** | | | |
| $V_{test}$ | tube · day | # of failures | failure rate (90% CL) |
| 4.65 kV | 31,720 | 0 | $\leq$ 2.3% per year |
| 4.1 kV | 20,100 | 1 | $\leq$ 7.1% per year |
| **COMBINED RESULT** | | | |
| $V_{test}$ | tube · day | # of failures | failure rate (90% CL) |
| 4.65 kV | 45,858 | 0 | **$\leq$ 1.8% per year** |
| 4.1 kV | 33,116 | 1 | **$\leq$ 4.3% per year** |

with only one more stringent condition, that is, once the module reached 5 kV then it should not draw more than 10 $\mu$A for at least 20 min in order to be accepted.

Next, a "soak test" (see section 6.4.2) was performed with the modules that passed the first step. The overall rejection rate for the first phase was between 5÷10%.

### 6.7.2 *Second Phase*

In this phase a continuous monitoring of the current was required over a period of 48 hours. For the monitoring we used the data acquisition system of the SLAC MAC experiment, consisting of Bertan power supplies to provide the HV to the daisy–chained 10 modules. The ground lead of every module was connected to the monitoring ADCs and every 15 seconds the ADC readings were acquired and stored on a VAX 11/780. The sensitivity of each channel was about 3 nA which was much better than the most sensitive limit (about 20 nA) provided by a CAEN HV power supplies used in the Campana test.
Before the "acceptance test" a series of short source ($Sr^{90}$) runs were performed in order to check the monitoring channels.

The rejection criteria used in this phase was exactly the same as mentioned in section 6.4.3.

The overall rejection rate after the first two phases was below 20%; the modules after being laminated into the chambers were then tested again with cosmic rays of which details will be discussed below.

## 6.8 TESTING OF THE WIC CHAMBERS

After the lamination of the LST modules, the completed WIC chambers (see Chapter 4) were tested using the cosmic rays[42] to check their mechanical and electrical quality.

The data taken during these tests were very useful to study in detail the chamber efficiency and resolution. In the following we will describe the chambers test procedure and the information obtained from the cosmic ray data.

### 6.8.1 *Leak and Capacitance Tests*

The all LST modules were checked for gas tightness before being laminated into the chambers. This was performed by immerging each tube in a water tank with 50 mbar of over pressure. A second gas leak test was performed after the lamination by keeping the WIC chambers under a pressure of 7.5 mbar and checking the leakages.

The second step of the test consisted of the all electrical connections check (modules and cathodes). The tube wires were tested by measuring the capacitance between the HV and ground leads of a each module with a high precision microprocessor–controlled automatic LRC meter. The frequency of the LRC meter was setted to 12 Hz in order to reduce the effects due to the variations of the graphite coating. Given the wire capacitance ($\approx$ 12 pF/m) and the total module lengths, any open connection inside the module was detected with unexpected low readings.
A similar technique was used to control the electrodes condition by using a commercial hand–held meter and measuring the capacitance between the electrode and its ground. Shorts detected at this stage, usually due to the copper filaments, were eliminated by connecting a low–voltage high-current power supply across the shorted elements for few seconds.
The LST identified to have a broken wire or nonrecoverable leakage was replaced.

### 6.8.2 *Cosmic Ray Test and Results*

During this test, the WIC chambers were placed horizontally on a rack arranged in 2 stacks, each containing 8 chambers separated by about 7 cm vertically. The top and bottom of the rack were covered to about half length by two (1 top and 1 bottom) scintillation counters which were used for the triggering. The integrated strip charge was read analogically with a threshold of *25 raw ADC counts ($\approx$ 8 pC) and the data were recorded and then analyzed on a* VAX 11/780. The LSTs were operated at 4.65 kV with the "standard mixture".

The experimental setup and data acquisition layout are shown in Fig. 6.7 and in Fig. 6.8, respectively.

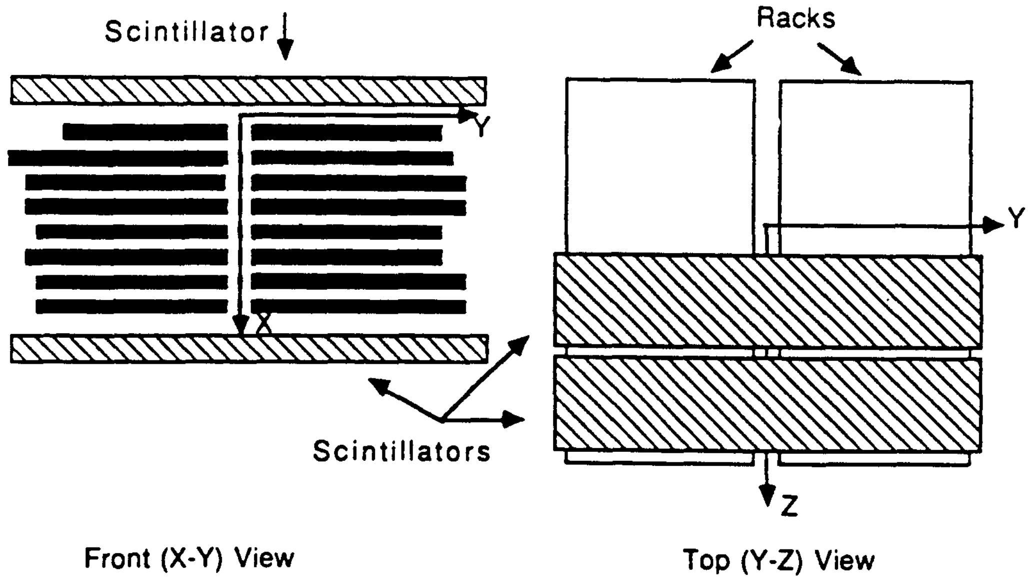


Figure 6.7. The layout of the cosmic ray test set-up.

In this test it was also possible to detect the system disconnected wire(s) not observed in the previous capacitance test (intermittent contact on the internal ceramic cards) by comparing the frequency of the "hit" wire(strips)s. A strip with few hits with respect to its adjacents was an evident sign of a missing wire for corresponding channel and approximately 0.1% of the wires of the finished chambers were found to be disconnected.

Another important point which has been checked, was the alignment of the strips with the wires. This was measured by the asymmetry of the strip hits induced on neighbors with respect to the central "hit" one of a cluster. The cluster asymmetry due to the displacement from perfect alignment of completed chambers has been found to be within $\pm$ 1 mm for most of the chambers.

### *6.8.2.1 Tracking Efficiency and Resolution*

Using the cosmic ray test setup we also investigated[59] the chamber muon tracking efficiency and resolution as a function of the impact angle ($\Theta$ and $\Phi$).

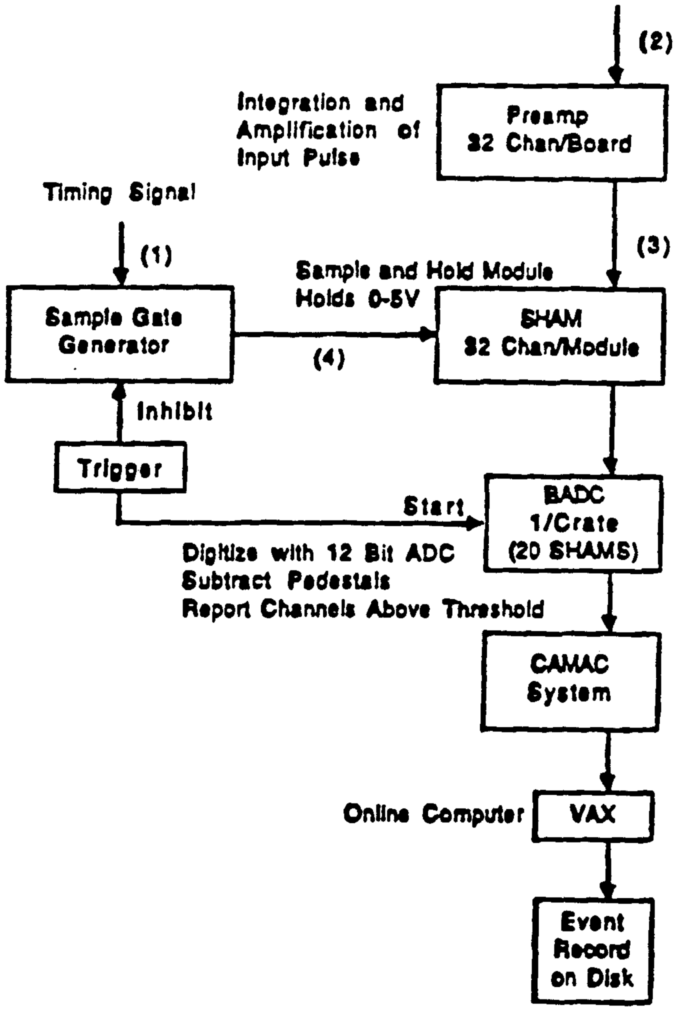


Figure 6.8. **Flux diagram of cosmic ray test data acquisition system.**

$\Phi$ is the track–wire angle in a plane perpendicular to the wires.

For the efficiency measurements we searched for the presence of a cluster within $\pm$ 3 cm from the predicted position by extrapolating the information obtained by the other planes (4 out of 8). The two upper and lower planes were used as reference planes.

As it is shown in Fig. 6.9. the efficiency for normal tracks ($\Phi$=0°, where $\Phi$ is the track–wire angle in a plane perpendicular to the wires) was about 90% because of dead spaces caused by the LST walls. Increasing the $\Phi$ impact angle it makes possible the penetration of tracks into the adjacent cells and the efficiency

increases up to 100% for $\approx \Phi$=60°.
The dependence of the efficiency on the angle $\Theta$, the track–wire angle in a plane parallel to the wires, is shown in the lower part of the same Figure. Increasing the $\Theta$, the number of the multi streamers also increase; because the portion of the wire receiving primary electrons extends with $\Theta$ but this does not strongly affect the efficiency of the chamber.
These results are in agreement with the expected efficiency calculated by considering the geometric inefficiencies of the chambers.

The spatial resolution of the X–strips has been studied in a similar way by searching for a cluster of up to 6 strips within 4 cm from the point extrapolated by the information of the other layers. The transverse resolution is about $\sigma \approx 0.34$ cm for the $\Phi$ less than 45°, which is slightly worse than the expected $\sigma \approx 1\ \mathrm{cm}/\sqrt{12} = 0.29$ cm. Fig. 6.10 shows the dependence of the muon tracking spatial resolution normalized to the intrinsic one, versus the angle $\Phi$.

## 6.9 Problems and Phenomena not Understood

After a considerable amount of testing on single LSTs and on completed chambers, performed by the *SLD* WIC group and other groups the basic features of these detectors have been clearly established. However, some problems are still not fully understood the so–called "dark current" which are present in a small fraction of the LSTs; the cause for the occasional bursts of current or the constant current well beyond the expected from the cosmic rays background.

As we will see in the following subsections, the *SLD* WIC collaboration has accomplished detailed studies in order to understand the nature of the "dark current", and compared the results with other experiments like Aleph[36], Opal[37], and CharmII[32]at Perugia, Campana and M.I.T. groups.

### *6.9.1 Extraneous Materials & Displaced Wires*

Our experience based on "post–mortem" observations of the LSTs which were drawing excessive current suggest that "dark current" can be drawn by a

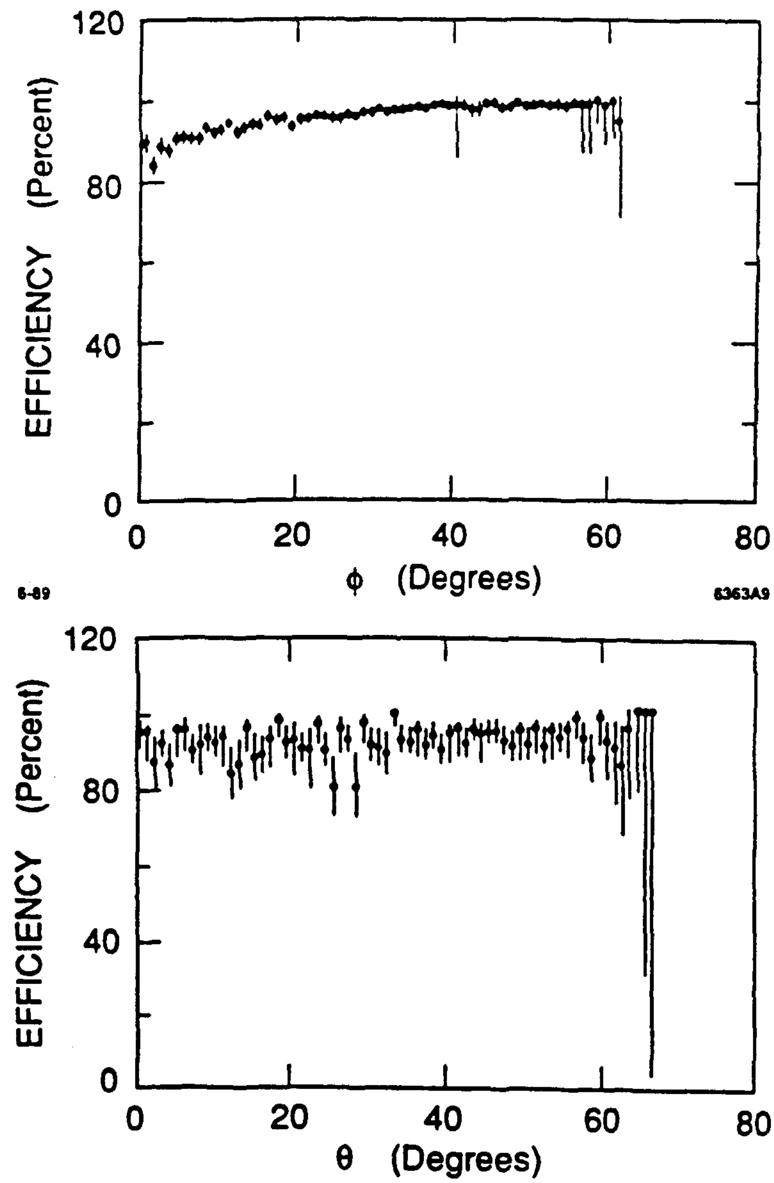


Figure 6.9. Chamber efficiency as a function of $\Phi$ (upper) and $\Theta$ (lower) impact angles. The results are consistent with the geometric limits.

LST for various reasons. For instance, if the wire is not centered in the LST channel because of the misplacement in the bridge which holds the wire, it can distort the local electric field, and may cause the breakdown. Similarly, the HV on such a wire will oscillate because of the successive breakdowns causing the current spikes.

Another conventional problem was the presence of the extraneous materials

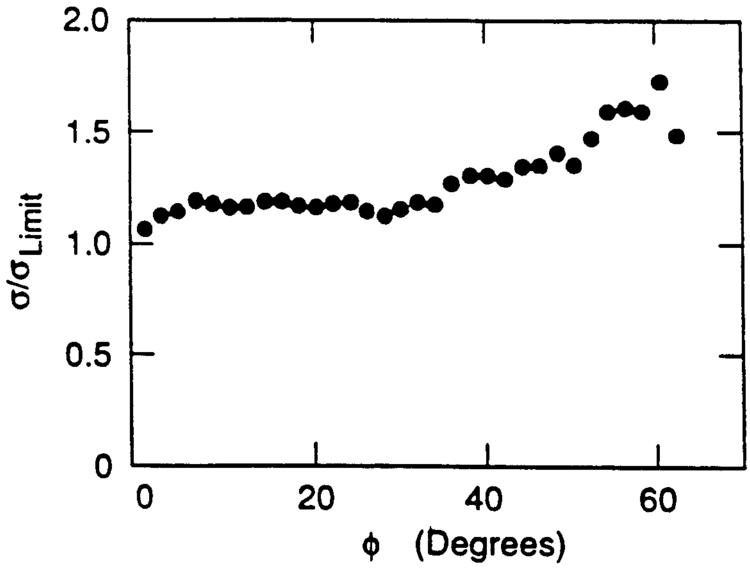


Figure 6.10. **The spatial X–strips resolution for muon tracking normalised to the intrinsic resolution (1 cm/$\sqrt{12}$) versus the $\Phi$ impact angle.**

for example, pollutants, dust and dirt inside the LST. It follows that care must be taken to keep the inside of modules as clean as possible. Our experience has shown that the tube insertion into its PVC envelope may result in PVC scraping by one part off another. Therefore, the use of a soft material between the two parts during the insertion and removing the tube is suggested.

### *6.9.2 Defective Graphite Coating and Glow Points*

A detailed study[60] in order to examine the source of the "dark current" other than the above mentioned conventional one, has shown a strong correlation between the presence of dark current and the glow points formed on the wires or on the graphite coated cathode. The glow point formation was inspected visually (inserting the modules inside the transparent sleeves) and with an image intensifier. A scanning electron microscope was used for the subsequent examination of the surfaces in detail, both in physical structure and chemical composition.

The results have shown that the total "dark current" is proportional to the number of glow points (see Fig. 6.11). Most of these glow points were located at the same place even if the wire and gas mixture compositions were changed different times. Using the electron microscope, found that the location of the glow points corresponds mostly to the presence of the small unpainted regions with very high resistivity. A qualitative explanation of this self-sustaining discharge in the tubes is based on the "Malter effect"[38] which consists in the accumulation of positive ion charges on these unpainted regions, leading the extraction of the electrons from the plastic and starting streamer discharges repeatedly.

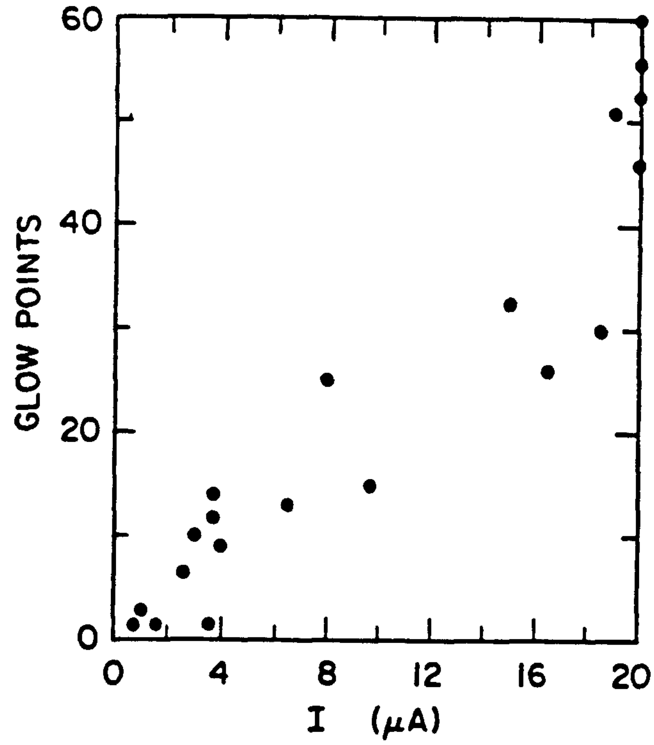


Figure 6.11. **Number of visible glow points in a bad module versus the current drawn by the module.**

Although the results of this study are not conclusive, they clearly suggest that uniform graphite coating and on-line control of the resistivity of all channels along the tubes are crucial and should be done very carefully.

*6.9.3 Current Spikes*

Another phenomenon is the sudden bursts of current occurring in the same module. The time duration of these spikes has been measured to be less than one second in 95% of the cases. We have not found a clear explanation to these current spikes, but we estimated that they should not damage the modules seriously since their integrated current over few years of operation is much smaller than 2 C/m, which is the safe limit established by our irradiation tests.

We lastly can add the anomaly of the current drawing of the perfectly functional LSTs when they first switched–on after a long period of pausing or after having been physically moved from one place to the other. Experiences of the various groups (UA1, Nusex) have shown that almost all the modules having this kind of problem were recovered after a certain period of re–conditioning.

### *6.9.4 Summary of Failures*

In Table 6.5 we summarize the results of the various causes of failure based on the visual "post–mortem" inspection of 60 LST modules after their failing during the various test steps.

## 6.10 WIC Prototype Beam Test Results

A prototype[61,62] of the WIC has been built and its performance has been studied in a test beam.

### *6.10.1 Test Calorimeter Setup*

The WIC prototype has been tested in conjunction with a prototype of the Liquid Argon Calorimeter in the test beam facility at SLAC. Fig. 6.12 shows the configuration of the elements of the experimental setup.

The test calorimeter has been constructed with 18 layers of LST chambers inserted between 17 layers of 5 cm thick $1.2 \times 1.2$ m$^2$ wide iron plates (total of 5.4 $\lambda$).

During the construction of these chambers on the bottom side of the LST modules a $112 \times 200$ cm$^2$ fiberglass electrode was laminated on which the strips

Table 6.5. Summary of the 60 opened LSTs after their failing at various steps of testing.

| Distribution of Defect Types | | | |
|---|---|---|---|
| Broken wire | 9 (@ bridge)<br>12 (@ G–10 card) | 21 | 35% |
| Displaced wire | 4 | 4 | 7% |
| White spots & poor coating | 6 | 6 | 10% |
| Whiskers(like) | 3 | 3 | 5% |
| Dust & Dirt | 9 | 9 | 15% |
| Others | 4 (leak)<br>1 (cracked card)<br>1 (hole) | 6 | 10% |
| No obvious evidence | 3 (recovered)<br>8 (not recovered) | 11 | 18% |

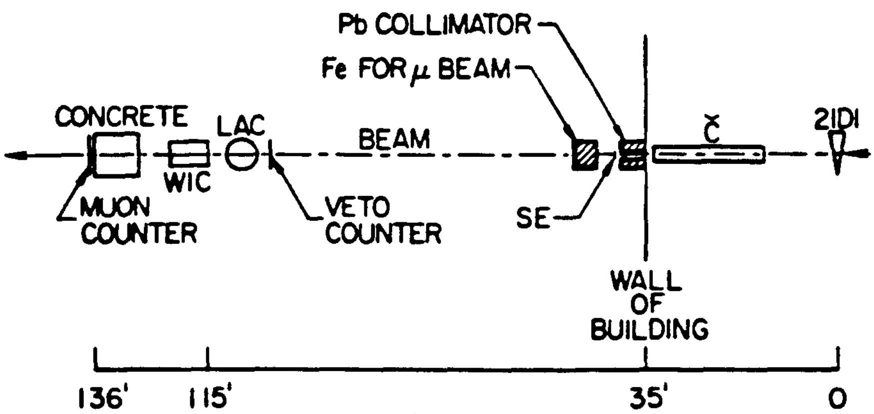


Figure 6.12. Test beam configuration.

were attached, and on the top side a sheet of fiberglass–copper was then glued to form the pad towers of size ranging from 22 $\times$ 22 to 25 $\times$ 30 cm$^2$.

The LSTs chambers were operated at voltages varying from 4.2 kV up to

4.65 kV with the "standard mixture", and data has been taken in two different periods (may 1985 and february 1986) with muon and pion beams of energies 5.5, 8.2, and 11 GeV.

The first period of data taking was performed by digitally reading the strip cathodes while during the second period, analogical readout was used for pads and strips. The uniformity of the response of different pads (or strips) was found to be within $\pm$ 5%.

#### *6.10.2 Experimental Results*

Before starting the data taking, strips and pads of the test chambers were calibrated[63] by sending known pulses through the data acquisition chain.

In order to have a clean pattern recognition for three different types ($\mu$, $\pi$ and e) of particles, various cuts were applied[62] in the off–line analysis. After these cuts, only the particles (one particle at a time) hitting the center of the calorimeter were accepted.

##### *6.10.2.1 Muon Selection*

Additional cuts have been applied to select the muons;

a) at least 10 hit planes out of 17,

b) less than two planes containing more than one clusters, and,

c) 10% $<$ $Q_{front}/Q_{total}$ $<$ 90% for both strip and pad signals, where $Q_{front}(Q_{back})$ is the total charge of the first(second) 8 layers.

After these cuts, the percentages of the selected events as a function of beam energy were 23%, 15% and 12% for 5.5 GeV, 8.25 Gev and 11 GeV, respectively.

We obtained the following results in the analysis;

1) the integrated charge produced by a minimum ionizing particle does not depend on the beam energy, and the transition from the proportional regime to the streamer one was observed by raising the operating voltages of the LSTs,

2) the efficiency for the normal tracks has been found to be approximately 91.6%

due to the geometrical inefficiencies and the average charge collected from a cluster at 4.6 kV was around 12 pC,

3) the width of the charge spectrum of a single muon passing through the calorimeter has been found to be $\Delta Q_{tot}/Q_{tot} \approx 25 \div 30\%$ for both strips and pads,

4) the $Q_{tot}(strips)/Q_{tot}(pads)$ has been found to be the same for different runs within $\approx 10\%$,

5) the position resolution was found $\sigma \approx 3.7$ mm for the digital, and $\sigma \approx 2.7$ mm for the analog strip readout.

*6.10.2.2 Pion Selection*

For the pions selection, the following additional cuts were applied;

a) rejection of the multiparticle events,

b) rejection of all the muons recognized by the algorithm used to search them,

c) rejection of the electrons of at least with 3 planes hit,

d) lateral containment, ($Q_{fid.vol} \geq 90\%$ of $Q_{tot}$),

e) longitudinal containment in the first 14 planes ($Q$(first 14 planes) $\geq 95\%$ of $Q_{tot}$).

Fig. 6.13 shows the pulse height spectrum obtained with the 11 GeV pions and Fig. 6.14 shows the energy resolution for 11 GeV pions as a function of the applied HV.

The analyzed data have shown that the calorimetry response has a good linearity, and the hadronic energy resolution is expected to be approximately $\sigma(\mathrm{E}) \approx 0.8\sqrt{E(GeV)}$ (see Fig. 6.15).

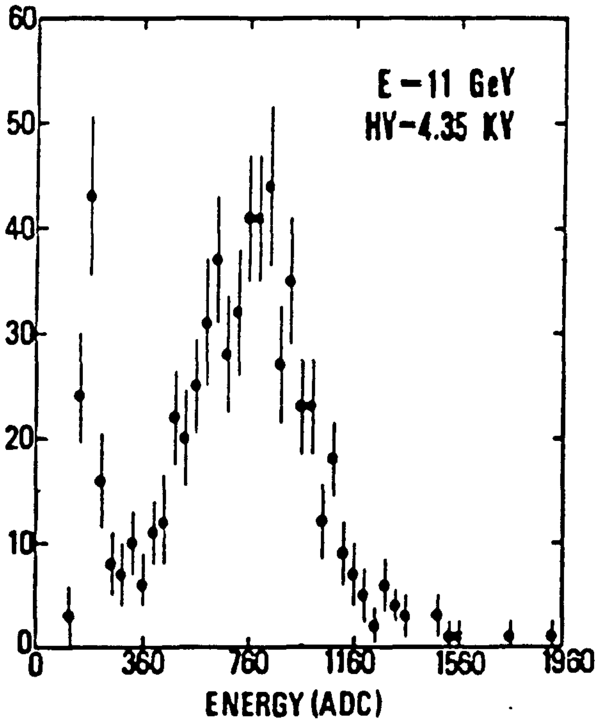


Figure 6.13. $\mu$ and $\pi$ peaks for 11 GeV beam.

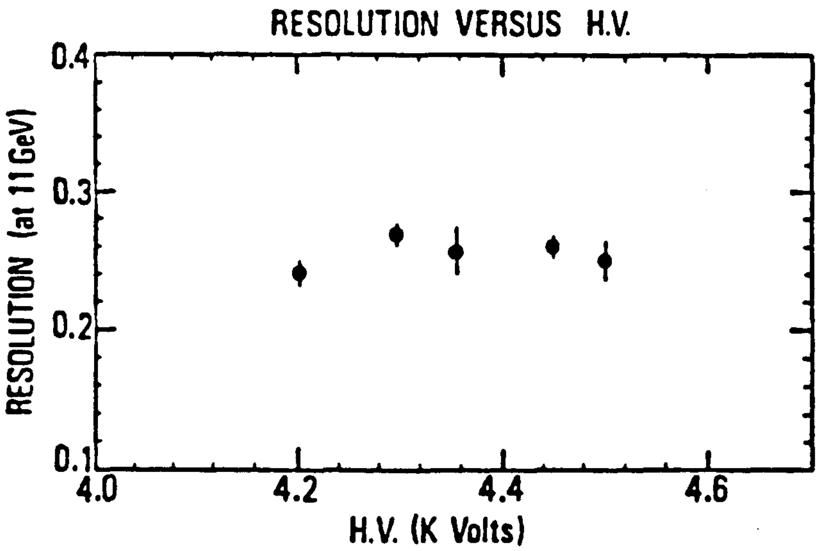


Figure 6.14. Resolution at 11 GeV for pions versus HV setting.

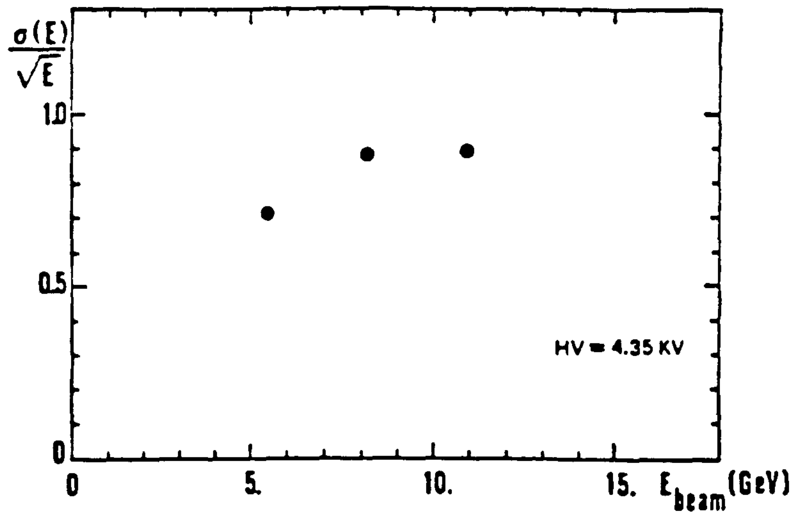


Figure 6.15. K=$\sigma(E)/\sqrt{E}$ versus beam energy.

# Appendix A. Studies of Non–Flammable $Ar+CO_2$+Hyd. Gas Mixtures

## A.1 INTRODUCTION

The gas mixtures used mostly in the LST detectors made up of "$Ar+C_4H_{10}$" or "$Ar+CO_2+C_5H_{12}$" are highly flammable when leaked into air. Thereby, considering the safety requirements of the *SLD* as well as the other large underground experiments, we have studied [64,65] the operating characteristics of the LSTs with non–flammable ternary mixtures made up of $Ar+CO_2$+hydrocarbon, containing less than 10% hydrocarbon. Some other groups have previously reported[66] good performance of the LSTs with non–flammable mixtures, but their LST geometry was different from that used in the WIC chambers.

In this Appendix, we will discuss the flammability characteristics of $CO_2$+hydrocarbon mixtures and will summarize the results after a brief description of the experimental setup.

## A.2 FLAMMABILITY CHARACTERISTICS OF $CO_2$+HYDROCARBON GAS MIXTURES

The flammability of a combustible gas mixture when leaked into air depends on the combustible/air ratio, and the mixture is considered flammable[67] if a flame can propagate within its volume. Due to the extinguishing effect of $CO_2$, higher concentrations of hydrocarbon are allowed in $CO_2$ than in air in order to have the final mixture non–flammable. Fig. A.1 shows the flammability limits of $C_4H_{10}+CO_2$ in air as a function of their fractions. In the region indicated as "flammable mixtures" the mixture is flammable when mixed with a determined amount of air. Flammability characteristics of isobutane is similar to that of the butane and flammability increase with the complexity of the paraffin hydrocarbon. In this study we also tested some other hydrocarbons like n-pentane and n-hexane but we have not used the more complex hydrocarbons because of their low vapor pressure. The argon–was treated like air from the point of view of flammability also because the Ar contents in the tested mixtures were much smaller (<10%) then the $CO_2$ contents.

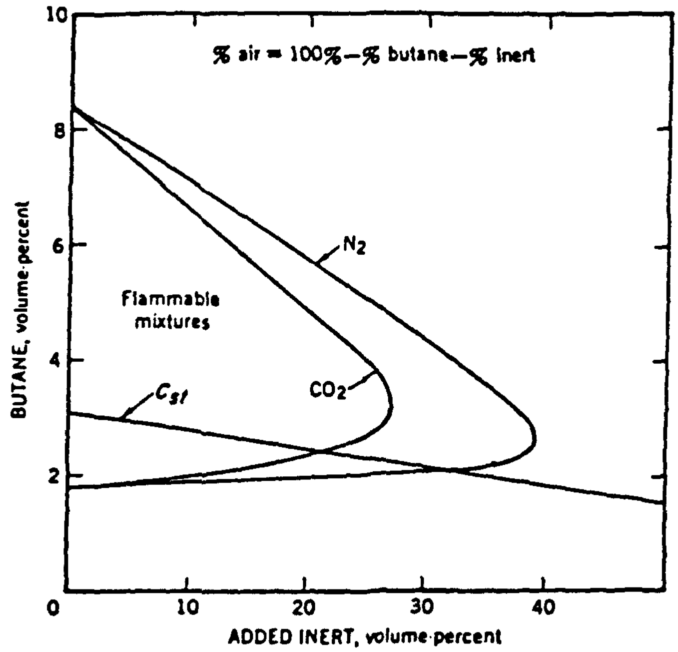


Figure A.1. Flammability limits for butane mixed with inert gas ($CO_2$ or $N_2$) and air. The slope of $C_{st}$ gives the maximum allowed combustible/inert ratio.

## A.3 Description of the Experimental Setup

The tests were performed in two different places; at Perugia University and SLAC, using the cosmic ray test setup described in Chapter 6.

In the Perugia setup (see Fig. A.2) 1.5 m long LSTs were used placed between two scintillators (utilized for the charge spectrum measurements) separated by 1.8 m and a layer of 7 mm thick lead was placed as absorber. The trigger was provided by two scintillation counters in coincidence with the test tubes (±3° tracks with parallel plane, and ±23° with perpendicular plane to the wires) and tubes were shielded with aluminum foil. To control the Ar, $CO_2$ and $C_4H_{10}$ fractions in the mixtures, a mass–flowmeter was used with an absolute accuracy of $\pm$ 1%. Due to the low vapor pressure of $C_5H_{12}$ and $C_6H_{14}$ a cooling system was developed and used (temperature stability better than 0.4 C°) shown in Fig. A.2 providing to have a relative accuracy for the fractions of the n–pent(hex)ane better than 5%. For the charge spectrum measurements signals were sent into a LeCroy2249A ADC gated for 500 ns by the trigger counters; for single rate curves, 0.090, 1.0 and 400 $\mu$s were set as dead times on three channels of a non–updating discriminator with 20 mV threshold into 50 $\Omega$. The data acquisition was provided by a modified MacIntosh–Plus with an additional Mac–Plinth board.

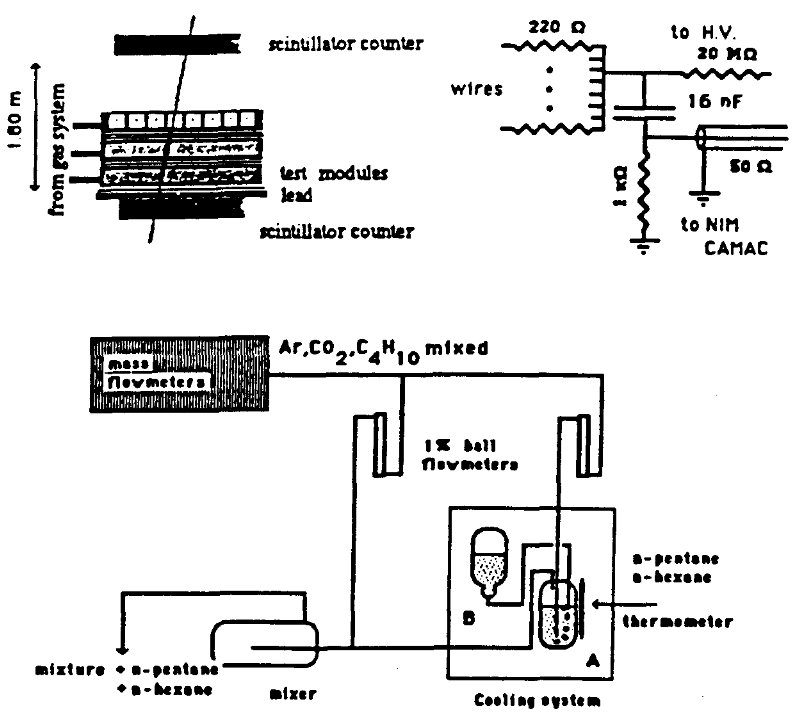


Figure A.2. Layout of the Perugia test set–up; (upper) test modules with the triggering scintillators, and coupling circuit, (lower) mixing system configuration for n–pent(hex)ane mixtures.

Tests at SLAC were performed on two finished WIC chambers. The top chamber with three modules was operated with the "standard mixture" and gas mixture under test was flowed through the bottom chamber. Only events with clean track in the top chamber were used to study the behavior of the bottom chamber. In both setups the ambiental conditions were controlled and in the SLAC setup, they have also been computer recorded.

## A.4 Results

The search of the best non–flammable gas mixture has been performed by the various ratios of three above mentioned hydrocarbons with Ar+$CO_2$ by keeping constant the maximum allowed fraction of the flammable gas and varying the Ar content in the range $0 \div 5\%$.

For each mixture we measured the single rate plateau as a function of the high voltage for three different discriminator dead times in order to study the effect of these shaping times to the single rate. The 90 ns dead time which is the drift time of an electron over a half tube cell for both "standard" and non–flammable mixtures, has been chosen to count the primary streamers (within 90 ns), secondary streamers occurring after about 90 ns and afterpulses (see subsection 3.3.3) caused by the extraction of electrons from the cathodes by the slow ions (approximately few hundreds of $\mu$s later than the primary streamers). In the same manner, the 1 $\mu$s dead time, corresponds to the sum of the primary and secondary streamers, and finally the 400 $\mu$s counts only the primary streamers.

After the scanning of different compositions of Ar+Isobutane+$CO_2$ we found that the composition (2.5%)Ar+(9.5%)$C_4H_{10}$+(88%)$CO_2$ has about the same knee as the "standard mixture" but the plateau width (400 V) of 1 $\mu$s dead time is narrower than that (700 V) of the "standard mixture" because of the higher rate of afterpulses. However, the presence of these afterpulses does not strongly affect the energy resolution of the hadronic calorimeter. Fig. A.3 and Fig. A.4 show, respectively, the single rate plateau as a function of HV for different discriminator dead times, and, the average streamer pulses on the wire, for the "standard" and "new" mixtures. Fig. A.5 shows how the argon concentration dominates both the secondary streamer, afterpulse activities and the location of the plateau knee as a function of HV. In Table A.1 compared are the results for the Ar+$C_4H_{10}$+$CO_2$ mixtures with the standard (25%)Ar+(75%)$C_4H_{10}$ mixture.

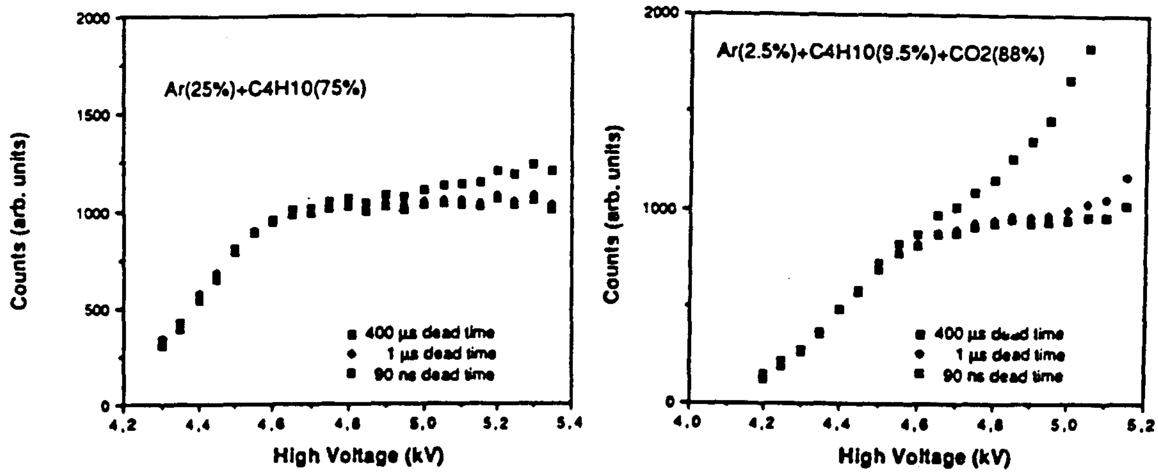


Figure A.3. Single counting rates versus HV for the "standard mixture" (left) and for the non-flammable "new mixture" (right) for different discriminator dead times. The threshold was 20 mV into 50 Ω.

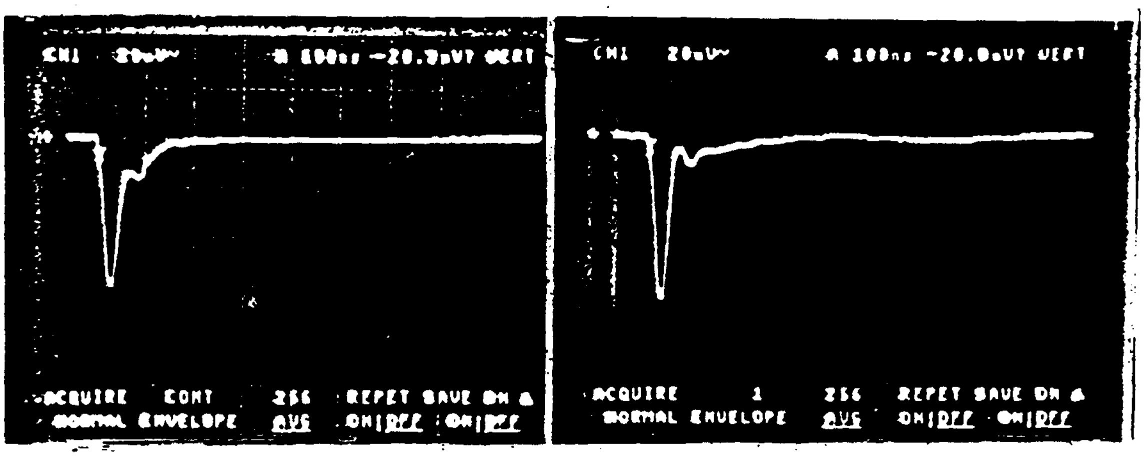

Figure A.4. Averaged streamer pulses on the wire at working point (4.7 kV) both for "standard mixture" (left) and for the non-flammable "new mixture" (right).

From these data we deduce that the mixture with (2.5%)Ar is a good candidate to substitute the flammable "standard mixture"; it has a reasonable

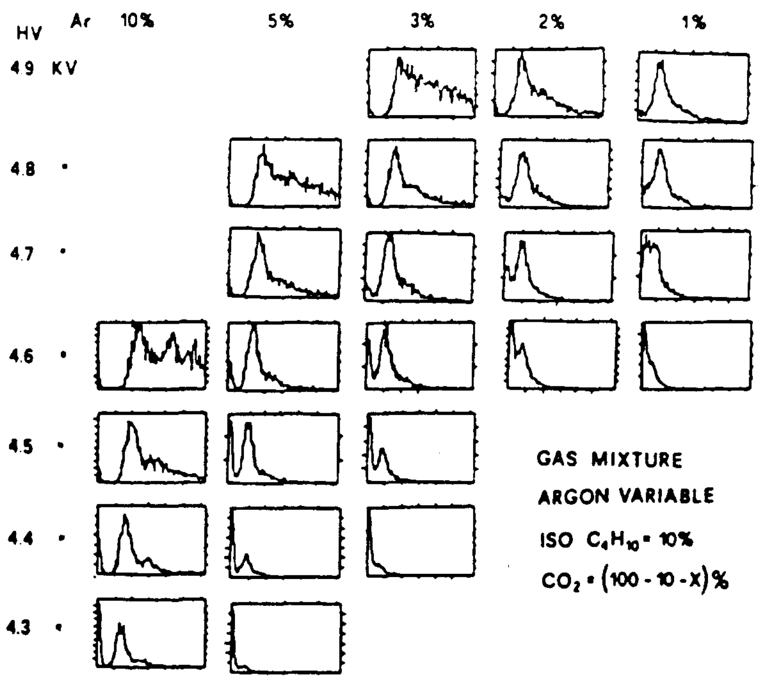


Figure A.5. Charge spectrum as a function of high voltage and different Ar concentration in the Ar+$C_4H_{10}$+$CO_2$ mixture.

Table A.1. Comparison of some important parameters obtained with (X%)Ar+(9.5%)$C_4H_{10}$+(Y%)$CO_2$ mixtures, where X=0, 2.5 or 5% and Y=100–9.5–X, with the "standard mixture". The discriminator dead time was 1 $\mu$s.

| Various Ar+Iso+$CO_2$ Compositions Compared with the Standard Mixture | | | | |
|---|---|---|---|---|
| Gas mixture under test | Operating point | Average charge on wire | Average dark current | Slope /100 |
| (0%)Ar+(9.5%)$C_4H_{10}$+(90.5%)$CO_2$ | 5.1 kV | ≈ 35 pC | ≈ 20 nA/7m | 13÷18% |
| (2.5%)Ar+(9.5%)$C_4H_{10}$+(88%)$CO_2$ | 4.75 kV | ≈ 51 pC | ≈ 30 nA/7m | 10÷15% |
| (5%)Ar+(9.5%)$C_4H_{10}$+(85.5%)$CO_2$ | 4.65 kV | ≈ 58 pC | ≈ 40 nA/7m | 10÷15% |
| (25%)Ar+(75%)$C_4H_{10}$ | 4.65 kV | ≈ 30 pC | ≈ 18 nA/7m | 2÷3% |

operating point (4.75 kV), acceptable plateau width (≈ 400 V with 1$\mu$s dead time), and low dark current (≤ 30 nA/7 m) at the working point. The average charge of a streamer at the working point is about 51 pC which is approximately

1.7 times higher than in the case of the "standard mixture".

The measurements made with n–pentane have shown that, within the limits of non–flammability and different (0, 2.5, 5%) Ar concentrations the behavior of the mixture is very similar to that of the isobutane.

In the same manner, the data taken with the n–hexane of which the concentrations are limited to ≤15% because of its low vapor pressure, have demonstrated a qualitatively similar behavior to n–pentane having approximately 400 V wide plateau. Because of the similar performance of the tested LSTs with three hydrocarbons used in non–flammable ternary mixtures, no clear evidence was found in favor of the use of the hydrocarbons heavier than the isobutane also because, they require sofisticated cooling systems due to their low vapor pressures.

### *A.4.1 Lifetime Test Results with the "New Mixture"*

Before deciding to substitute the "new mixture" with the "standard" one, we performed a lifetime test[68] similar to that discussed in section 6.2. The test was performed at SLAC using the same technique and test setup of Campana lifetime test and utilizing the SLACs gas system.

A total of 403 modules of various lengths (from 5.06 m to 7.04 m), purged for about 10 volumes with the "new mixture → (2.5%) Ar+ (9.5%) $C_4H_{10}$+(88%) $CO_2$", were reconditioned and soak tested using the standard procedure and failure criteria described previously. At the end of the reconditioning and soak tests, a total of 10 LST modules failed (6 conditioning and 4 soak with a failure rate of ≈ 2.5%) and disconnected from the remainder of the test.

The lifetime test was performed with 393 survived LST modules which were continuously kept at 4.75 kV except for switch–off of the HV for 10 minutes twice a day.

After 106 days (41,550 tube·days) only one LST module failed, but when this module was opened, a displaced wire was found and therefore the failure was

not considered caused by the tested gas.
The failure rate of this lifetime test was found to be <2.0%/year at 90% C.L. (not considering the failure) which is comparable with the combined result (<1.8%/year at 90% C.L.) of the Campana and SLAC lifetime tests.

After the lifetime test, 94 modules were kept at under 4.75 kV for a period of 25 days without switching–off and on the HV, and at the end of this period, 3 problematic modules which were occasionally drawing high currents were opened and found that all three modules had displaced wires.

We then concluded that, this three component non–flammable mixture, having similar operational characteristics and failure rate, can successfully substitute the old "standard mixture".

Recently other groups [69,70] have performed further studies on these mixtures obtaining very encouraging results. In particular, Moromisato *et al.* have tested a similar non–flammable ternary mixture (2%)Ne+(10%)$C_4H_{10}$+(88%)$CO_2$ using the neon as noble gas. Their results on the operating characteristics were very similar to ours and they also observed no change on the pulse height spectra after a long term wire–aging test (0.4 pC/1 cm wire).

# Appendix B. Studies of Non–Flammable Fast $CF_4$ Based Gas Mixtures

## B.1 Introduction

Using the same experimental technique and setup shown in Fig. A.2 we have studied[71] the characteristics of various compositions of the $CF_4$+hydrocarbon(+Ar) mixtures. For drift time measurements we used a 2226A LeCroy TDCs triggered by the scintillators. The purpose of the study was to develop a non–flammable fast gas mixture which would give the possibility of using the LSTs for muon detection also in the high repetition rate (i.e $10\div25$ ns/beam interaction) multi TeV hadron colliders. A similar study exists in the case of the multiwire proportional chambers[72], but nothing was done previously in the streamer regime.

$CF_4$, having a rather stable molecular structure with high bond strength (low polymerization rate) contrary to the most of the halogenated hydrocarbons, is not self–quenching enough to be used alone in gas detectors, but becomes stable and fast with a small addition ($\approx \geq$10%) of quenching gas.
Because of its good extinguishing capability (twice as $CO_2$), larger hydrocarbon fractions are allowed in non–flammable $CF_4$ mixtures than in $CO_2$.

## B.2 Results

$CF_4$ mixture with 13%, 11%, 9.5% of $C_4H_{10}$, $C_5H_{12}$, $C_6H_{14}$ respectively, have been tested with the 0 and 2.5% of argon; the percentage of $CF_4$ in these mixtures was then given by % $CF_4$=100%–Ar–hydrocarbon. All these mixtures are non–flammable.

The measurements taken with $CF_4$+Iso(+Ar) have shown that the presence of a little fraction of argon moves ($\approx$ 700 V) the plateau knee to lower voltages drastically without influencing appreciably the spurious streamer activity. The charge collected at the knee is $\approx$ 15 pC almost independent from the presence of argon; the average pulse height is twice larger in presence of argon.
The drift time spectrum of $CF_4$+Ar+Iso mixtures obtained with cosmic rays, exhibits saturated drift velocities of about 110$\pm$10 $\mu$m/ns which is approximately twice larger than the mixtures without $CF_4$.

The data taken with n–pentane is comparable with the isobutane mixtures, although the average charge is larger in particular when there is no argon in the mixture.

The n–hexane measurements also suggest that, $CF_4$ acts not simply as quenching gas but acts also as a noble gas. As it is shown in the upper part of Fig. B.1, the plateau width is approximately the same with or without presence of argon. The small argon fraction in the mixture lowers the plateau knee by about 800 V and induces large amount of double streamers. The pulse heights are similar in both cases (72 mV with and 60 mV without Ar) having the different durations, (62 ns with and 37 ns without Ar respectively).

In conclusion, $CF_4$+n–hexane mixtures seem to be very good non–flammable fast mixture between the studied compositions, having a reasonable working point (at 4.65 kV), large pulse height (60 mV into 50 $\Omega$), wide plateau of approximately 300 V and low secondary streamer activity (both from photons and ion cathodic extraction). In all cases, the drift velocities were saturated and at least twice higher ($\approx$ 110 $\mu$m/ns) than in the case of the "standard mixture". It should be noted that the radiation hardness and long term behavior of this mixture should be investigated in detail to have a complete information on its operational characteristics, although preliminary measurements suggest very good behavior of $CF_4$ based mixtures at high particle fluxes.

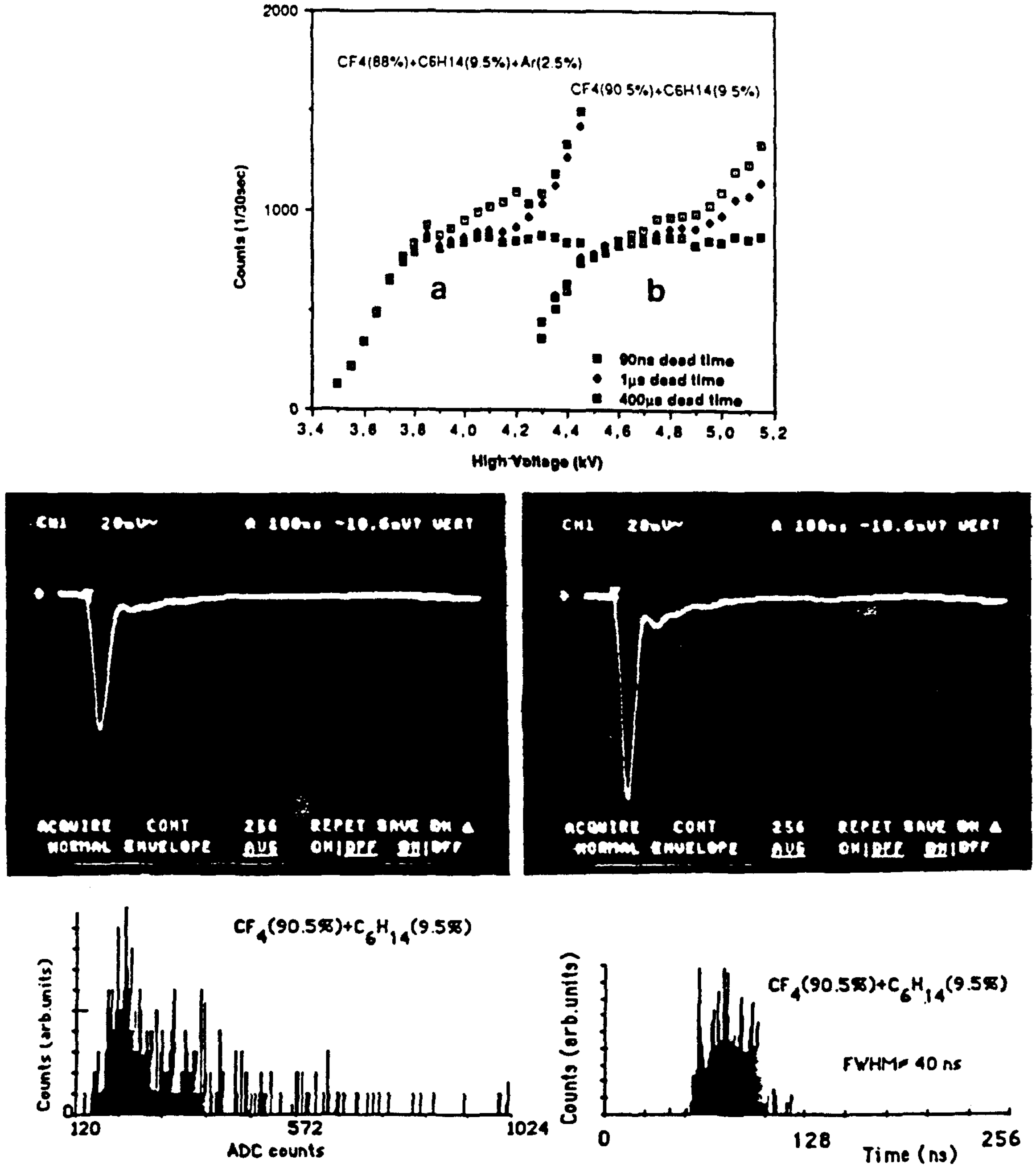


Figure B.1. (upper) Single counting rates versus HV with different discriminator dead times and 10 mV threshold into 50 Ω for a) (88%)$CF_4$+(9.5%)$C_6H_{14}$+(2.5%)Ar; b) (90.5%)$CF_4$+(9.5%)$C_6H_{14}$; (middle) averaged wire streamer pulses at (left) 4.55 kV, (right) 4.75 kV, and (lower) charge spectrum at the knee (4.6 kV, 500 ns ADC gate) (left), drift time spectrum at 4.85 kV (right), for (90.5%)$CF_4$+(9.5%)$C_6H_{14}$ mixture.

# Appendix C. WIC Database (DBWIC) System

## C.1 Introduction

The large amount of data obtained from the various tests of the LSTs and chambers plus the geometrical information on the WIC structure, require the use of a database system to organize and analyze this information by also giving the possibility to be utilized from the analysis and/or simulation programs.

In this Appendix we be describe briefly the NOMAD2–Database system used for the WIC.

## C.2 Structure and Facilities of DBWIC

DBWIC is a relational database written with NOMAD2 which is a database management system[73] that allows to store and make use of data.

On DBWIC, the data are stored, either directly from external sources (i.e IBM mainframe) or by–hand through the appropriate interface procedures, in major sections called "masters" and subsections called "items" which are the units of data. In order to eliminate the possibility of duplicated records we have chosen one or more items for each master that make it unique, and we then organized the data into groups of related items in a main program called "schema".

When the data are retrieved, records from different files are matched and joined together and treated as if they were one record from one file.

In DBWIC there are 24 masters which have mainly been grouped as follows;

a) (ideal & real) geometry information,

b) all SLAC based and some Campana test information,

c) others (i.e institutions, persons, phones, physicists, shifts etc.).

Thanks to NOMAD2's powerful LIST command and its plot, statistics and table facilities, it is relatively simple for users to create reports and make analysis [74,75] utilizing the stored information. Fig. C.1 shows an example of a report obtained from the stored data of the SLAC based LST module tests.

```
TOTAL GOOD MODULE    5,084

TOTAL BAD  MODULE  **1,347**  % 20.94

TOTAL      MODULE    6,431

-----------------------------------------------------------------------
                                                                  TOTAL
INDIVIDUAL                                                        OF IND.
FAILURES   LEAK   SOAK+COND+OTHERS   ACCEPTANCE   CAPACITANCE     FAILUR.
                                                   Low - Short

CAMPANA     -          155               -              -           155

SLAC       23          283             806          95     4      1,211

TOTAL      23 %.3      438 %6.37       806 %12.59   99 %1.53   **1,366**

-----------------------------------------------------------------------

          BASIC DESCRIPTIVE STATISTIC ON THE MODULE CURRENTS


                       Number
                       of obser    Mean        Standard
No.  Variable  name   (coat per)  (mic A )     deviation   Skewness    Kurtosis
---  ---------------  --------   ----------   ----------  ----------  ----------

 1   &GOOD                  8       0.030        0.009       1.734       1.841
 2   &BAD                   8       0.367        0.117       0.359      -1.426
 3   &ALL                   8       0.128        0.047       0.608      -0.627

Correlation matrix
------------------

No.  Variable  name       1      2      3
---  ---------------    -----  -----  -----
 1   &GOOD              1.000
 2   &BAD              -0.431  1.000
 3   &ALL               0.005  0.670  1.000
```

Figure C.1. A typical report on summary of the barrel LST module information retrieved from DBWIC by using the various NOMAD2 facilities.

## REFERENCES


1. "Fifty Years of Weak–Interaction Physics" Edts. Bertin, Ricci, Vitale I.P.S.–Bologna, April 26, 1984 (416–484).
2. W. Marciano and A. Sirlin, Phys. Rev. **D22** (1980) 2695.
3. M. Consoli and A. Sirlin, "Physics at LEP", CERN–86–02 Vol.1 (1986) 63.
4. C. Baltay, "*SLD* Physics Studies", SLAC–Rep.–354, October (1989) 1.
5. R. Battiston *et al.*, "*SLD* Physics Studies", SLAC–Rep.–354, October (1989) 103.
6. P. Rankin, "Proc. of the third Mark II Workshop on *SLC* Physics", SLAC–Rep.–315, July (1987) 63.
7. G. Bonvicini *et al.*, "Proc. of the third Mark II Workshop on *SLC* Physics", SLAC–Rep.–315, July (1987) 546.
8. U.J. Becker, talk given at PASCOS–90, March 27–31, 1990, Boston–USA.
9. M. L. Swartz, "Polarization at *SLC* ", CERN–88–06 Vol.2 (1988) 166.
10. P.D.B. Collins, A.D. Martin, E.J. Squires, "Particle Physics and Cosmology", John Wiley&Sons, 1989.
11. A.S. Johnson, *SLD* "Physics Studies", SLAC–Rep.–354, October (1989) 438.
12. *SLD* Physics Rep.–1, December 1988.
13. C. Ahn *et al.*, "Opportunities and Requirements for Experimentation at High Energy $e^+e^-$ Collider". SLAC–Rep.–329, May (1988).
14. P.C. Rowson *et al.*, *SLD* "Physics Studies", SLAC–Rep.–354, October (1989) 513.
15. J. E. Clendenin *et al.*, SLAC–PUB–3285.
16. W. B. Atwood *et al.*, SLAC–PUB–3910, March 1986.
17. D. Aston *et al.*, SLAC–PUB–4795, June 1989.
18. "SLD Design Report", SLAC–Rep.–273, May (1984), revised in (1987).
19. R. Dubois *et al.*, SLAC–PUB–3813, October 1985.

20. A. Benvenuti *et al.*, SLAC–PUB–5028, July 1989.

21. A. Benvenuti *et al.*, SLAC–PUB–5066, August 1989.

22. M. Breidenbach, SLAC–SLD–NOTE 137, October 1985.

23. G. M. Haller *et al.*, SLAC–PUB–3778, September 1985.

24. D. J. Sherden, SLAC–SLD–NOTE 163, October 15, 1986.

25. F. Sauli, "Principles of Operation of Multiwire Proportional and Drift Chambers", CERN 77–09, May (1977).

26. G. Charpak *et al.*, Nucl. Ins. and Meth., **162** (1979) 405.

27. A. Barbaro *et al.*, Nucl. Ins. and Meth., **213** (1983) 223.

28. T. Takahashi, "Proc. on Gas Sampling Calorimetry Workshop II", Fermilab, (1985) 385.

29. S. Brehin *et al.*, Nucl. Ins. and Meth., **123** (1975) 225.

30. G. Battistoni *et al.*, Nucl. Ins. and Meth., **164** (1979) 57.

31. M. Atac *et al.*, Nucl. Ins. and Meth., **200** (1982) 345.

32. W. Flegel *et al.*, "Proc. on Gas Sampling Calorimetry Workshop II", Fermilab, (1985) 313.

33. G.Battistoni *et al.*, Nucl. Ins. and Meth., **217** (1983) 429.

34. E. Iarocci, Nucl. Ins. and Meth., **217** (1983) 30.

35. P. Rapp, Nucl. Ins. and Meth., **A244** (1985) 430.

36. P. Campana, "Proc. on Gas Sampling Calorimeter Workshop II", Fermilab, (1985) 445.

37. C. Bosio, "Proc. on Gas Sampling Calorimeter Workshop II", Fermilab, (1985) 507.

38. L. Malter, Phys. Rev. **50** (1986) 48.

39. Wit Busza, M.I.T Technical Report, April 1987.

40. G. Battistoni *et al.*, Nucl. Ins. and Meth., **202** (1982) 459.

41. Cos. Mecc. Bindi, San Giustino, Italy.

42. A. Benvenuti *et al.*, SLAC–PUB–4677, July 1988.

43. A. C. Benvenuti *et al.*, SLAC–PUB–4993, October 1989.

44. C. W. Davidson, "Transmission Lines for Communications", Macmillan 1978.

45. U. Schneekloth *et al.*, WIC–Memo, January 3, 1987.

46. F. Beconcini *et al.*, INFN/TC–86/17 (1986).

47. R. Battiston, WIC–Memo, November 8, 1986.

48. B. Alpat *et al.*, WIC–Memo, December 6, 1986.

49. CERN–EP, Internal Note on the LSTs, July 18, 1986.

50. S. Fuess *et al.*, WIC–Memo, March 16, 1987.

51. G. M. Haller *et al.*, IEEE Trans. Nucl. Sci. **NS–33** (1986) 221.

52. F. E. Taylor *et al.*, WIC–Memo, October 26, 1986.

53. F. E. Taylor, WIC–Memo, January 11, 1987.

54. T. Federico *et al.*, WIC–Memo, August 18, 1986.

55. J. Va'vra, SLAC–PUB–3882, February 1986.

56. F. E. Taylor *et al.*, WIC–Memo, November 2, 1986.

57. G. Battistoni, "Proc. on Gas Sampling Calorimeters Workshop II", Fermilab, 1985 (594).

58. R. De Sangro *et al.*, WIC–Note 110, June 29, 1987.

59. A. Calcaterra, WIC–Note 145, September 18, 1987.

60. P. Struckman *et al.*, WIC–Memo, July 15, 1986.

61. G. Callegari *et al.*, IEEE Trans. Nucl. Sci. **NS– 33**, 1986.

62. R. Battiston *et al.*, SLAC–SLD–NOTE 158, July 10, 1986.

63. L. Servoli, private communication.

64. S. Cartwright *et al.*, Nucl. Ins. and Meth., **A277** (1989) 177.

65. L. Piemontese *et al.*, SLAC–PUB–5016, July 1989.

66. T. Uebayashi *et al.*, Nucl. Ins. and Meth., **A265** (1988) 457.

67. M. C. Zebatakis, National Bureau of Mines, Bull. 625 (1965).

68. U. Schneekloth, WIC–Note 88–028, August 29, 1988.

69. LVD Internal Note 61, December 1989.

70. J. H. Moromisato, Nucl. Ins. and Meth., **A274** (1989) 177.

71. B. Alpat *et al.*, Nucl. Ins. and Meth., **A277** (1989) 260.

72. J. Fisher *et al.*, Nucl. Ins. and Meth., **A238** (1985) 249.

73. NOMAD2 Reference Manual, Vol.s 1–2, D&B Computing Services.

74. B. Alpat, WIC–Note 120, August 4, 1987.

75. R. De Sangro, WIC–Note 100, April 27, 1987.

## Acknowledgements

First of all, I would like to thank all the *SLD*–WIC collaborators. The studies reported here benefited mostly from the superb work realized by them. I am grateful to all who contributed to the *SLD* effort.

I would like to thank Prof. W. Busza for useful discussions outlining the present work. My special thanks goto Prof. Battiston for his stimulating discussions.

I wish to thank, the director of Perugia INFN group, Prof. G. Mantovani, for his wise advise during and after my studies and for arranging good research facilities. In addition, I would like to acknowledge the efforts of Madeline Serio who patiently has read and correct the english text and of Dr. G.M. Bilei who has made it possible to have SLAC's library at Perugia. It is a pleasure to thank my co–workers Drs. M. Pauluzzi and L. Servoli whom I enjoy working with.

Finally, I want to thank first, my wife for her infinite forbearance, affection and support to texifize the whole thesis and last but not least, my parents for their patience, love and encouragement without which I would never have made it this far.